2018

Multiscale Deformation And Failure Behavior Of Polymer Bonded Explosives Subjected To High Rate Loading

Suraj Muthiramalil Ravindran
University of South Carolina - Columbia

MULTISCALE DEFORMATION AND FAILURE BEHAVIOR OF POLYMER BONDED EXPLOSIVES SUBJECTED TO HIGH RATE LOADING

by

Suraj Muthiramalil Ravindran

Bachelor of Technology
University of Kerala, 2008

Master of Technology
Indian Institute of Technology, 2011

Submitted in Partial Fulfillment of the Requirements

For the Degree of Doctor of Philosophy in

Mechanical Engineering

College of Engineering and Computing

University of South Carolina

2018

Accepted by:

Addis Kidane, Major Professor

Michael A. Sutton, Committee Member

Xiaomin Deng, Committee Member

Jennifer L. Jordan, Committee Member

Cheryl L. Addy, Vice Provost and Dean of the Graduate School

ACKNOWLEDGMENTS

First, and most importantly I would like to extend my gratitude to my advisor Dr. Addis Kidane for his guidance, support and fruitful discussions that helped me in enjoying the research. This research would not have been possible without his advice, insight, and encouragement. I sincerely thank him for being available any time to support in my struggles.

Dr. Michael Sutton is greatly acknowledged for his encouragement, continued support for my entire Ph.D. research duration in the University of South Carolina. Dr. Jennifer Jordan is sincerely acknowledged for her generosity in reviewing our research papers and providing valuable comments. I gratefully acknowledge Dr. Xiaomin Deng for his valuable comments on my research.

I would also like to express my gratitude to my current and graduated lab mates: Addis Tessema, Behrad Koobhor, Ali Fahem, Vijendra Gupta, Dennis Miller, Ronak Patel, Peter Malchow, and Abigail Wohlford. Especially, I would like to thank my friend and colleague Addis Tessema for all the support and shared struggles. My gratitude is extended to Bill Bradly, David Westbury, Renee Jenkins, Lalitha Ravi, and Misty O'Donnell, for their kind assistance.

Finally, I would like to thank my beloved wife, Bhavya, my parents, Ravindran and Sumathi, and my brother, Suveesh, for their love and emotional support.

ABSTRACT

Polymer bonded explosives (PBX) are heterogeneous granular composites with a high-volume fraction of solid. Typically, they contain 80-95% explosive crystals and 5-20% soft polymer binder. These materials are subjected to different loading conditions during their service life. The main function of the soft binder is to reduce shock sensitivity to prevent an accidental explosion. However, there have been inadvertent detonations in these materials during transportation and handling. The reason for such unintentional explosion is not well understood. It is commonly accepted that the formation of local high-temperature regions, called 'hot spots', is the primary cause. Hotspot formation is associated with the local energy dissipation mechanisms in the material system during dynamic loading.

There is a large knowledge gap in understanding the dynamics of local failure mechanisms in polymer bonded explosives subjected to loading at different time scales. The primary focus of the present work is to understand the local deformation mechanisms in polymer bonded explosives subjected to high rate and impact loading. An experimental method is developed based on high-speed photography and digital image correlation (DIC). The experimental setup helps to observe and quantify the deformation mechanisms in-situ at a spatial and temporal resolution of 10.66 μm/pixel and 200 ns, respectively. The capability of the experimental setup is validated in two heterogeneous materials system at strain rates varying from 150-1000 s^{-1}.

In this study, polymer bonded sugar (PBS), a mechanical simulant of PBX is used. PBS contains sugar solid crystals and plasticized hydroxyl-terminated polybutadiene (HTPB) as the soft binder. Two different dynamic loading configurations are studied, simulating high strain rate and high impact loading conditions.

The first loading configuration involves the dynamic loading of PBS specimens at a strain rate from 150 to 1000 s^{-1}. High temporal resolution dynamic deformation measurements are conducted at macro and meso (local) length scales. From these experiments, global and local deformation mechanisms and failure behavior are studied in detail. The effects of strain rate and particle volume fraction on the deformation mechanisms are studied for a comprehensive understanding of the material behavior. These experiments reveal the link between the macroscale shear band formation and its microscopic origin.

The second case involves, a direct impact loading utilizing a gas-gun with impact velocity varying from 50 to 100 m/s. From the images captured during loading, a quantitative analysis of the compaction wave dynamics is performed at two length scales. The particle velocity, compaction wave velocity, and wave thickness are calculated from the macroscale experiments. In addition. spatial stress distribution is determined from the equilibrium equations using the full displacement data obtained from DIC. From stress and strain rates, the total energy dissipated during compaction wave propagation is estimated. Finally, mesoscale experimental observations are used to identify the main local failure and deformation mechanisms associated with the energy dissipation.

TABLE OF CONTENTS

LIST OF TABLES

LIST OF FIGURES

CHAPTER 1

INTRODUCTION

Polymer bonded explosives (PBXs) are a class of energetic granular composite materials that are widely used in military explosives, civil engineering applications, and jet propulsion. They typically contain 80-95% of explosive crystals and 5- 20% of the soft polymer binder. The explosive crystals that are typically used in the PBX are 1,3,5,7-Tetranitro-1,3,5,7-tetrazocane (HMX), 1,3,5-Trinitro-1,3,5-triazinane (RDX), 2,2-Bis[(nitrooxy)methyl] propane-1,3-diyl dinitrate (PETN) etc. Whereas the common binder material used in these materials are Viton, plasticized hydroxyl-terminated polybutadiene (HTPB), esatane, rubber etc. The inert binders reduce the chances of accidental detonation by minimizing the impact sensitivity. In addition, these soft binders help to improve castability, machinability and structural integrity of the explosive composites.

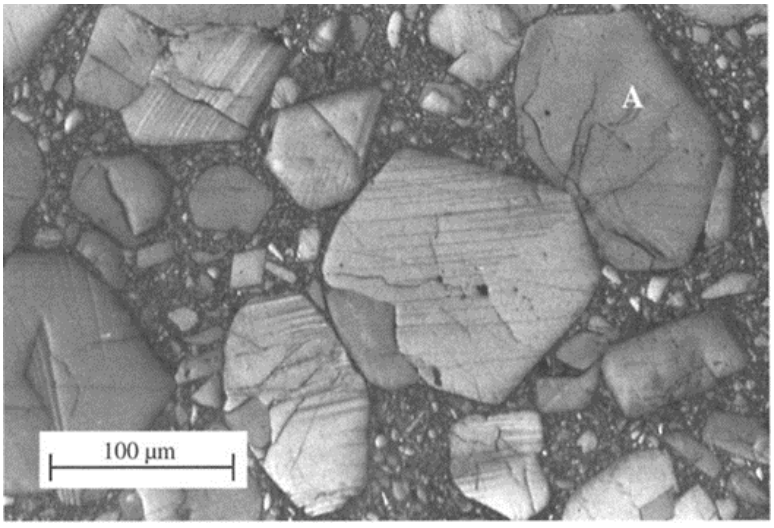

Figure 1.1 Microstructure of HMX bases polymer-bonded explosive

PBXs are highly heterogeneous due to a substantial mismatch in material properties of the binder and explosive crystals, the presence of voids and damage in the material. Typical microstructure of HMX based PBX sample with 95 % solid loading is shown in Figure 1.1. These materials can be subjected to loading at different time scales during transportation and handling, which may cause accidental detonation. This gives rise to safety concerns during handling. It is widely believed that the formation of local heating regions called hot-spots is the main reason for early detonation. The formation and dynamics of the hotspots are mainly controlled by local failure and energy dissipation mechanisms. Therefore, a clear understanding of the local failure mechanisms in this these materials are inevitable for a precise prediction of the material behavior.

The problem is that with all of the studies we still cannot predict with any precision, in general, what will happen to an explosive if we hit, heat, drag, drop, or do anything else outside of its design envelop. Interestingly, the design envelope is determined by the test protocols that attempt to cover the possible loading scenarios an explosive may subject in its service life. These test protocols are empirical in nature, therefore, very little understanding of the detonations mechanisms. Therefore, several experiments are required to consider all the potential loading scenarios to have a wider design envelope for safe handling. However, it is not feasible due to the cost and time required. The solution to this problem is to numerically simulate the material behavior under different loading conditions using reliable material models. However, the experimental validation of such models is very difficult due to the lack of understanding of the local failure mechanisms in PBX at different length and time scales.

1.1 BACKGROUND AND MOTIVATION

In the last two decades, a significant amount of research has been devoted to understanding the deformation and failure mechanisms in PBX [1–10]. Quasi-static loading of the HMX based PBX shows a wide variety of mechanisms involved in the failure of the PBX. The macroscopic failure was observed to be due to the formation of shear bands as seen in Figure 1.2a [11,12]. Whereas, the postmortem studies show that the debonding of the polymer binder from crystals, fracture and twinning of crystals as shown in Figure 1.2b are the major mesoscale failure mechanism in PBXs under quasi-static loading.

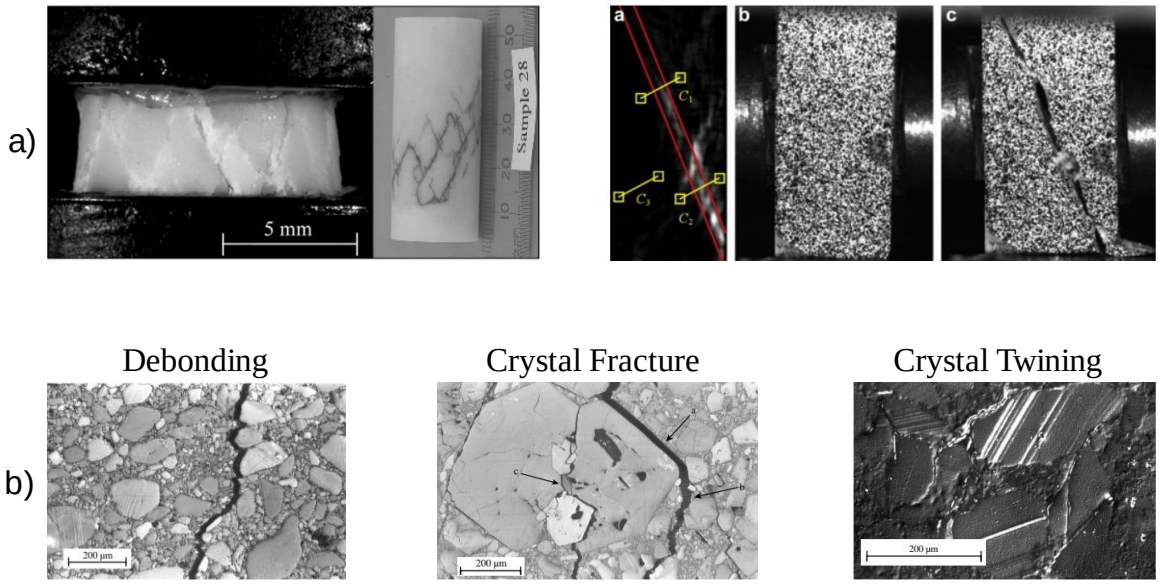

Figure 1.2 (a) Shear band formation in PBXs, (b) Grain scale (mesoscale) mechanisms involved in PBXs.

Continuum scale high temporal resolution in-situ experiments have provided much insight into the high rate macro scale deformation behavior of PBX. It was shown that even a low amplitude insult can lead to ignitions and violent explosions in PBX [13]. With the help of high speed photography and heat sensitive films, observation has been made at

macroscale, and shear band formation is considered as the prime macroscale failure mechanism in PBX [11,14]. Unfortunately, such macro scale experiments cannot resolve the mesoscale mechanisms that cause shear banding and hot spot formation. It is well known that thermal softening due to large strain (10-50% strain) deformation is responsible for the formation of the shear band in most materials under dynamic loading [15]. However, in PBX, shear bands are observed at a strain far below the strain required for thermal softening.

In case of impact type loading, numerical studies in PBXs show the propagation of the compaction type wave at low impact velocities (50-200 m/s) [16]. Though several shock propagation experimental based investigations are available to quantify the shock nature in PBX in different loading regimes [17–19], no attempts have been made to measure the spatial stress profile, which is essential in estimating the energy dissipation profile during the shock wave propagation. Especially in the weak shock regime that is close to transport accidental loading.

Optical methods, such as photoelasticity, digital speckle radiography, digital gradient sensing, laser-induced fluorescent speckle photography, and digital image correlation have been used in the past to understand the failure and fracture mechanics of materials subjected to dynamic loading [11,20–26]. These types of experiments are inadequate to understand the local deformation mechanisms in highly heterogeneous PBX materials under dynamic loading. On the other hand, high spatial resolution micro scale experiments have elucidated the local deformation mechanisms in these materials under quasi-static (10^{-4} to 10 s^{-1}) loading conditions [6, 9]. Though high spatial resolution full-field DIC measurements based on optical microscopes or scanning electron microscopes

have been successfully implemented to measure local deformation in different materials at submicron scale under quasi-static loading conditions [7-11], high temporal measurement with high spatial resolution is not well established. Figure 1.3 shows the some of the high spatial and temporal resolution of the experiments that have been performed in the past 20 years using DIC. It should be noted, the maximum resolution obtained using visible DIC is 15 µm/pixel which inadequate in measuring local deformation in PBX. It is required to have at least 10 µm/pixel at a temporal resolution of 500 ns for measuring the local deformation behavior in PBX samples with 200 µm grain size.

The present investigation is focused mainly on the understanding the multiscale deformation and failure mechanism in polymer bonded explosives subjected high rate loading. An experimental setup based on high speed imaging and digital image correlation is developed. Using the experimental setup, a detailed investigation of PBX under high rate and impact type of loading is performed.

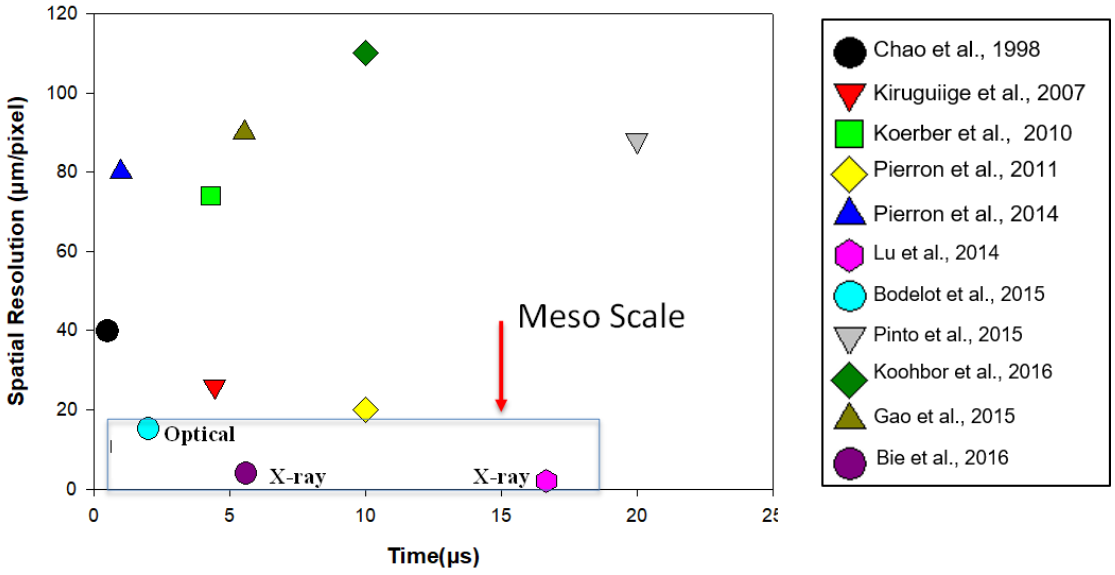

Figure 1.3 Experiments with spatial resolution and corresponding temporal resolution.

1.2 LIST OF REFRENCES

[1] Balzer JE, Siviour CR, Walley SM, Proud WG, Field JE. Behaviour of ammonium perchlorate-based propellants and a polymer-bonded explosive under impact loading. Proc R Soc A Math Phys Eng Sci 2004;460:781–806. doi:10.1098/rspa.2003.1188.

[2] Barua A, Horie Y, Zhou M. Microstructural level response of HMX–Estane polymer-bonded explosive under effects of transient stress waves. Proc. R. Soc. London A Math. Phys. Eng. Sci., vol. 468, The Royal Society; 2012, p. 3725–44.

[3] Siviour CR, Grantham SG, Williamson DM, Proud WG, Field JE. Novel measurements of material properties at high rates of strain using speckle metrology. Imaging Sci J 2009;57:326–32.

[4] Drodge DR, Williamson DM. Understanding damage in polymer-bonded explosive composites. J Mater Sci 2016;51:668–79.

[5] Field SGG and CRS and WGP and JE. High-strain rate Brazilian testing of an explosive simulant using speckle metrology. Meas Sci Technol 2004;15:1867.

[6] Roessig KM. Mesoscale mechanics of plastic bonded explosives. AIP Conf. Proc., IOP INSTITUTE OF PHYSICS PUBLISHING LTD; 2002, p. 973–8.

[7] Liu C. On the minimum size of representative volume element: an experimental investigation. Exp Mech 2005;45:238–43.

[8] Hu Z, Luo H, Bardenhagen S, Siviour C, Armstrong R, Lu H. Internal Deformation Measurement of Polymer Bonded Sugar in Compression by Digital Volume Correlation of-Tomography. Exp Mech 2015;1:289–300.

[9] Gray III GT, Blumenthal WR, Idar DJ, Cady CM. Influence of temperature on the high-strain-rate mechanical behavior of PBX 9501. tenth Am. Phys. Soc. Top. Conf. Shock compression Condens. matter, vol. 429, AIP Publishing; 1998, p. 583–6.

[10] Siviour C., Laity P., Proud W., Field J., Porter D, Church P., et al. High strain rate properties of a polymer-bonded sugar: their dependence on applied and internal constraints. Proc R Soc A Math Phys Eng Sci 2008;464:1229–55. doi:10.1098/rspa.2007.0214.

[11] Williamson DM, Siviour CR, Proud WG, Palmer SJP, Govier R, Ellis K, et al. Temperature–time response of a polymer bonded explosive in compression (EDC37). J Phys D Appl Phys 2008;41:085404. doi:10.1088/0022-3727/41/8/085404.

[12] Wang X, Ma S, Zhao Y, Zhou Z, Chen P. Observation of damage evolution in polymer bonded explosives using acoustic emission and digital image correlation. Polym Test 2011;30:861–6.

[13] Idar DJ, Lucht RA, Straight JW, Scammon RJ, Browning R V, Middleditch J, et al. Low amplitude insult project: PBX 9501 high explosive violent reaction experiments. Los Alamos National Lab., NM (United States); 1998.

[14] Field JE. Hot spot ignition mechanisms for explosives. Acc Chem Res 1992;25:489–96.

[15] Molinari A, Clifton RJ. Analytical Characterization of Shear Localization in Thermoviscoplastic Materials. J Appl Mech 1987;54:806–12.

[16] Barua a., Horie Y, Zhou M. Microstructural level response of HMX-Estane

polymer-bonded explosive under effects of transient stress waves. Proc R Soc A Math Phys Eng Sci 2012;468:3725–44. doi:10.1098/rspa.2012.0279.

[17] Tarver CM, Forbes JW, Garcia F, Urtiew PA. Manganin gauge and reactive flow modeling study of the shock initiation of PBX 9501. AIP Conf. Proc., vol. 620, AIP; 2002, p. 1043–6.

[18] Gustavsen RL, Aslam TD, Bartram BD, Hollowell BC. Plate impact experiments on the TATB based explosive PBX 9502 at pressures near the Chapman-Jouguet state. J. Phys. Conf. Ser., vol. 500, IOP Publishing; 2014, p. 52015.

[19] Dick JJ, Martinez AR, Hixson RS. Plane impact response of PBX 9501 and its components below 2 GPa. Los Alamos National Lab., NM (United States); 1998.

[20] Sundaram BM, Tippur H V. Dynamics of crack penetration vs. branching at a weak interface: an experimental study. J Mech Phys Solids 2016;96:312–32.

[21] Sundaram BM, Tippur H V. Dynamic mixed-mode fracture behaviors of PMMA and polycarbonate. Eng Fract Mech 2017;176:186–212.

[22] Sundaram BM, Tippur H V. Full-field measurement of contact-point and crack-tip deformations in soda-lime glass. Part-I: Quasi-static Loading. Int J Appl Glas Sci 2018;9:114–22.

[23] Sundaram BM, Tippur H V. Full-field measurement of contact-point and crack-tip deformations in soda-lime glass. Part-II: Stress wave loading. Int J Appl Glas Sci 2018;9:123–36.

[24] Zhou Z, Chen P, Duan Z, Huang F. Study on fracture behaviour of a polymer-bonded explosive simulant subjected to uniaxial compression using digital image

correlation method. Strain 2012;48:326–32. doi:10.1111/j.1475-1305.2011.00826.x.

[25] Grote DL, Park SW, Zhou M. Dynamic behavior of concrete at high strain rates and pressures: I. experimental characterization. Int J Impact Eng 2001;25:869–86.

[26] Huang JY, Li Y, Liu QC, Zhou XM, Liu LW, Liu CL, et al. Origin of compression-induced failure in brittle solids under shock loading. Phys Rev B 2015;92:144101.

CHAPTER 2

DYNAMIC MESO-SCALE FULL FIELD SURFACE DEFORMATION MEASUREMENT OF HETEROGENEOUS MATERIALS

[1]*Ravindran, S.,* Tessema, A., & Kidane, A. (2016). *Review of Scientific Instruments*, 87(3), 036108. https://doi.org/10.1063/1.4944488 Reused here with permission of publisher.

2.1 ABSTRACT

A dynamic experiment at mesoscale is developed to measure local deformation and strain in granular materials at high temporal and spatial resolutions. The experimental setup is comprised of a high-speed camera along with a high magnification extension tube. The method is demonstrated by measuring the full field strain across and in the boundary of the crystals at a high temporal resolution in polymer bonded sugar crystals and glass beads filled epoxy particulate composite specimens under dynamic loading. In both cases, the local strain heterogeneity is captured successfully. The measured strain and deformation field can be further used to obtain the relative motion of each crystal, crystal rotation, and the relative displacement between the polymer interface and the crystal, which are very critical to understand the local failure mechanisms in heterogeneous materials.

2.2 INTRODUCTION

Since proposed in 1949 by Kolsky, the Kolsky bar has been widely used to characterize materials under dynamic loading conditions [1]. The recent development of optical systems and digital based experiments extended the technique to accommodate non-homogeneous and anisotropic materials. Dynamic properties of heterogeneous materials with defects have been investigated in Kolsky bars along with photoelasticity and digital image correlation (DIC) [2–5]. Though these optically based measurements with a high temporal resolution at macro scale have been valuable techniques to understand the failure mechanism at continuum scale, they could not provide insights into the local deformation mechanisms [6–10]. Due to the material inherent heterogeneity, measuring deformation at sub-grain scale level is paramount to fully understand the fundamental failure mechanism of granular materials.

DIC has been effectively implemented to measure deformations at submicron scale under quasi-static loading [11,12]. However, high temporal digital image-based measurements at a high spatial resolution are still not well established. Recently, high speed X-ray has been used for full field strain measurement and damage assessment at high temporal and spatial resolutions [13,14]. For strain measurement, ultrafast X-rays and X-ray speckles (inherent features) are used to obtain the images before and after deformation.14 The application of X-ray DIC has been demonstrated successfully [15]. However, due to its complex experimental setup, difficulty in obtaining appropriate X-ray speckles and high cost associated with commissioning and running the setup, the X-ray DIC is limited to few users.

The demand for understanding the dynamic local deformation and failure mechanisms of heterogeneous materials necessitates alternative and relatively simple optical full-field deformation measurements at sub-grain scale. Bodelot et al. recently using a high-speed camera, HPV-2, equipped with an Infinity K2 long-distance microscope, measured the deformation of copper at a framing rate of 500 000 frames/sec and achieved a spatial resolution of 15.2 μm/pixel. In this note, an optical based experimental setup that can be used to obtain surface strain fields and deformation in heterogeneous materials at a speed up to one million frames per second and spatial resolution of 10 μm/pixel is presented. To demonstrate the technique, two material systems: (1) polymer bonded sugar crystals, 85% sugar crystals of size varying 200-800 μm with 15% of plasticized hydroxyl terminated polybutadiene (HTPB) and (2) glass filled epoxy particulate composite, 80% spherical glass beads of diameter between 200 and 400 μm with 20% epoxy are used and their local deformation under dynamic loading is measured.

2.3 MATERIALS AND METHODS

A conventional specimen size, dimensions 18×12×12 mm is used to make sure that the representative volume element is enough to give the continuum scale response of the material when loaded with Kolsky bar. For the DIC, a high contrast, random and isotopic pattern is needed. It is important to choose the right size speckles according to the image resolution of the optical system and experimental setup. As a "thumb of rule" for good displacement resolution and accuracy, every speckle has to be sampled by at least 3-5 pixels [16,17]. To generate the needed speckles on the specimen surface, the specimen is grounded and dry polished with silicon carbide paper of grit size varying from 240 to 1200 and then fine polished with diamond particles of 3 μm. The area of interest (AOI) is marked and the microstructural image of the AOI is taken before loading using an optical microscope. During speckling, a thin layer of white paint was applied, using an airbrush, on the specimen surface covering the AOI and left to dry partially. A black toner particle size varies from 12 to 20 μm is deposited on top of the partially dried white paint by blowing the powder onto the surface using an air gun and was kept to dry completely. With this process, random high contrast and isotropic speckle patterns are obtained.

Schematic representation of the proposed experimental setup is shown in Figure 2.1. The setup is comprised of a Kolsky bar with input and output bars made of polycarbonate, data acquisition, oscilloscope, strain gages, amplifier, and high magnification optical system. The high magnification optical system incorporates a high-speed camera and high magnification extension tube focused at the AOI of the specimen. The high-speed cameras used in this experiment are SA-X2 by Photron at 100, 000 frames/s and HPVX-2 by Highland Imaging at 1, 000, 000 frames/s and the high magnification extension tube is

from Navitar. Lighting is provided using two cold light light-emitting diode (LED) lamps and one single point halogen flexible light pipe (not shown in schematic) that is kept as close as possible to the specimen without obstructing the camera view. Post processing is done with the help of commercially available software Vic2D, by Correlated Solution, Inc., and details of the correlation parameters used in our study are given in Table I. The theory and further description of DIC technique can be found elsewhere [16–18]. The measurement noise level was estimated by correlating 15 still images taken just before the start of the dynamic test. The strain was computed using the parameters given in Table I. The noise level in strain was in the order of 1000 micro-strain for both cameras, with an uncertainty of 0.2% for SA-X2 and 0.33% for HPVX-2, which is accurate enough to capture the large local deformation expected in heterogeneous materials.

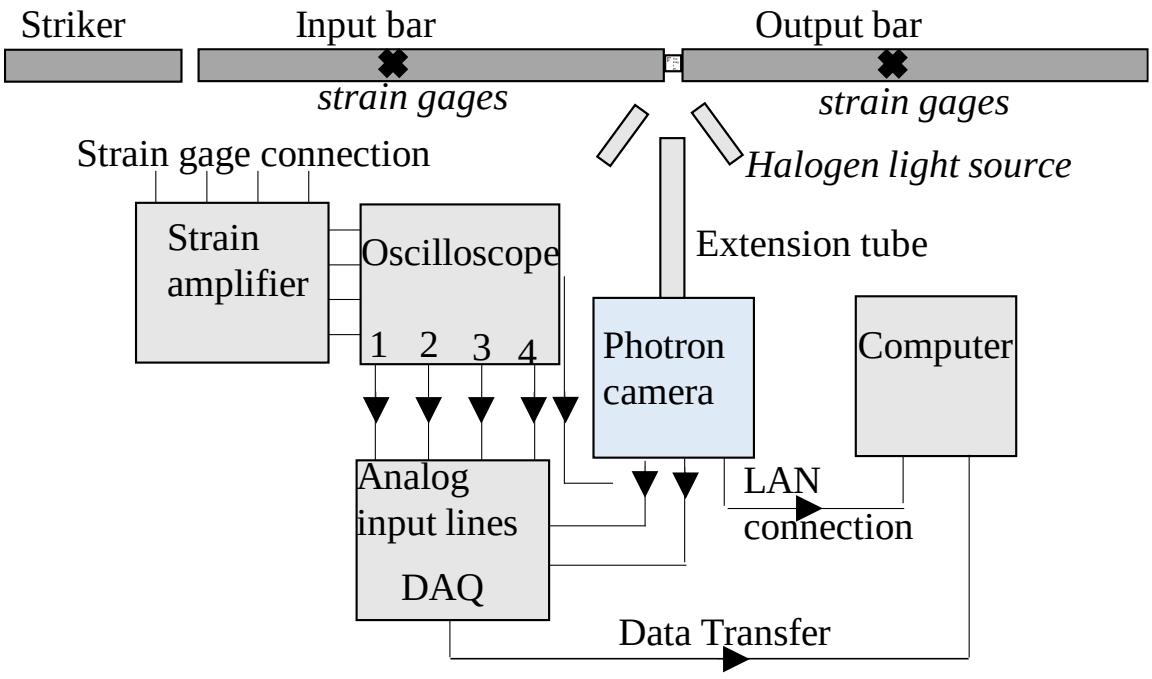

Figure 2.1 Schematic of the experimental setup

Table 2.1 Experimental post processing parameters

Camera/Parameters	Photron	HPV-X2
Field of View	$3840\times2640\mu m^2$	$4200\times2600\mu m^2$
Framing Rate:	1×10^5 f/second	1×10^6 f/second
Subset size:	11×11 pixel^2 110×110 μm^2	9×9 pixel^2 96×96 μm^2
Step Size	1 pixel/ 10μm	1 pixel/ 10.66μm
Filter size	9 pixel / 90 μm	9 pixel / 96μm
Resolution	10μm/pixel	10.66μm /pixel
Interpolation type	Optimized 8-tap	Optimized 8-tap
Matching criterion	Zero-normalized squared differences	
Strain tensor type:	Lagrangian	

2.4 RESULTS

Figure 2.2 shows the local strain field with the corresponding microstructure of a polymer bonded sugar (PBS) subjected to dynamic loading at instant 160 μs from the time the loading starts. As shown in the figure, highly heterogeneous strain localization is captured using the proposed experimental setup. It is important to note that the local axial strain is as high as 8% for only 3.5% of global axial strain. In addition, the lateral strain is localized predominantly at 45◦ from the loading axis indicating a local shear band formation. The shear formation observation is also supported by the local shear strain field shown in Figure. 2.2 c. The local tensile transverse strain (Figure. 2.2 b) is as high as 8%, indicating the possibility of interface failure and delamination of crystals. It can be seen that the strain localization is confined at the polymer rich interfaces between particles while most of the particle stays within the elastic range. It is also noticed that the high strain localization occurred in the region where small crushed crystal powders are bonded

together with the binder and surrounded by large crystals. For example, the area surrounded by the crystals 10, 15, and 19 is rich in polymer and shows high strain localization indicating a hot spot area in the material for failure initiation. On the other hand, there are some cases where the lateral strain in the crystals is higher than the failure strain of the sugar crystal, for example, crystals 13, 6, and 20. This indicates that there are locations where crystals fracture. Though it is hard to identify the reason for the large strain observed in some crystals, the existence of initial flaw was the cause at least for crystal 6. The initial crack on crystal 6 seen in Figure. 2.2a expands and opens as loading progress and causes high strain localization as shown in the local lateral strain plot in Figure. 2.2c. The sharp point contact between crystals 13 and 14 could form stress concentration on crystal 13 and led to crystal 13 to fracture and could be the reason for the large strain observed in that region.

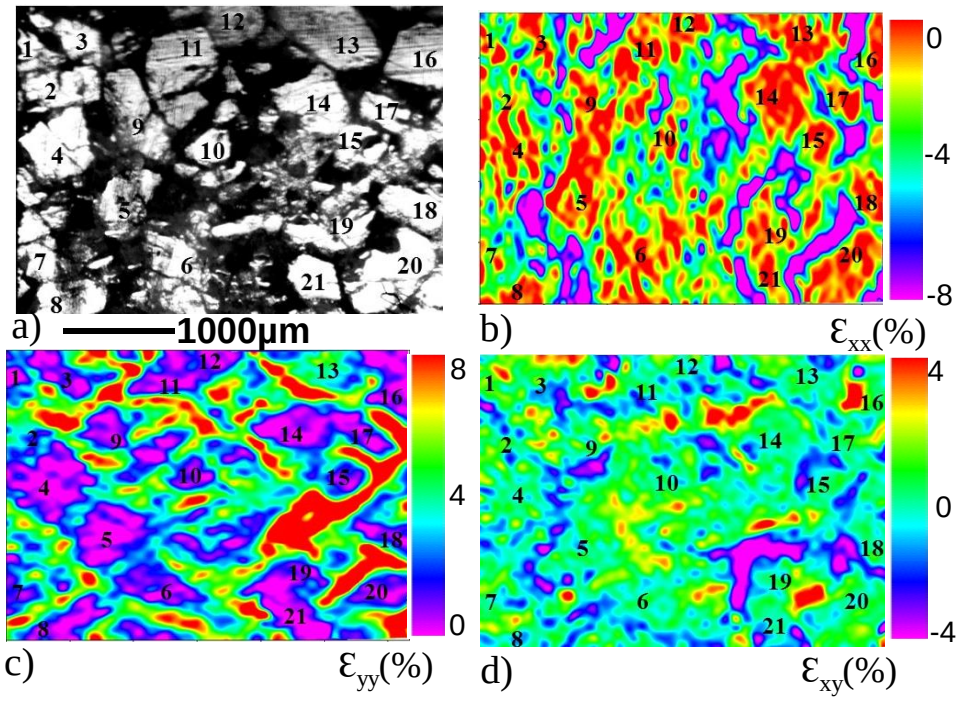

Figure 2.2 Component strains and the corresponding microstructure (a) Microstructure of PBS specimen with crystals numbered (b) Axial (c) Transverse and (d) Shear strain fields, at160μs.

Similarly, the local strain distribution is captured at a higher rate for the glass-epoxy particulate composite specimen. Though the strain heterogeneity looks similar to the one shown in PBS, in the case of glass-epoxy composites, the strain localization initiated and reached the local failure strain early. Since the epoxy is way harder than the HTPB binder, this is expected. At 0.43% global strain, the axial strain reaches as high as 3% and the local transverse strain reaches as high as 8%. The high local transverse strain shown in Figure. 2.3c indicates that a fracture might have already initiated at this location. It is also interesting to note that the crack seems to initiate at the epoxy binder interface and the fracture path deviate as it approaches the glass boundary. More importantly, the local transverse strain trend indicates that there might be a force chain mechanism with a favorable path for the force as observed in granular materials at macro-scale [19,20].

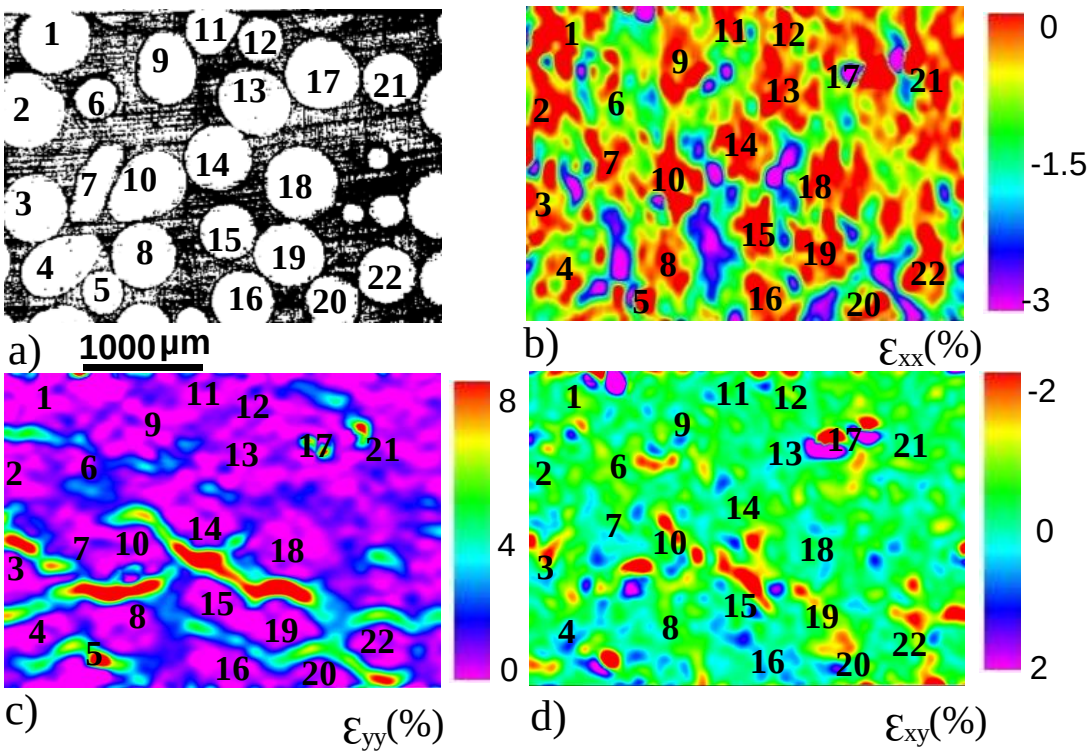

Figure 2.3 Microstructure of glass bead-epoxy specimen with crystals numbered and the corresponding (b) Axial (c) Transverse and (d) Shear strain fields, at14µs (0.42% Global Axial Strain).

2.5 SUMMARY

In summary, an optical based experimental setup is developed and the deformation of the dynamically loaded granular samples is measured at sub-grain-scale and up to a framing rate of 1×10^6 /s. It is demonstrated that the existing optical system can be used for the mesoscale dynamic experiment to measure local strain in granular materials at high temporal and spatial resolutions. The experimental system provided quantitative data on local strain information in heterogeneous materials. In general, it is observed that the local strain field is highly heterogeneous, mostly confined in the polymer-rich region, and propagates as load progress and leads to shear banding in the material. The obtained full field local information can be further used to measure the relative motion of each crystal, crystal rotation, and the relative displacement between the interface and the crystals, which are very critical to understand the local failure mechanisms in heterogeneous materials. The experimental method can be extended and used to obtain strain field in other granular materials of even a smaller crystal size by using higher magnification lenses.

2.6 LIST OF REFERENCES

[1] Kolsky H. An investigation of the mechanical properties of materials at very high rates of loading. Proc Phys Soc Sect B 1949;62:676.

[2] Shukla A, Zhu CY, Xu Y. Dynamic stresses in granular assemblies with microstructural defects. J Eng Mech 1992;118:190–201.

[3] Hurley R, Marteau E, Ravichandran G, Andrade JE. Extracting inter-particle forces in opaque granular materials: Beyond photoelasticity. J Mech Phys Solids 2014;63:154–66.

[4] Xu LR, Rosakis AJ. Impact damage visualization of heterogeneous two-layer materials subjected to low-speed impact. Int J Damage Mech 2005;14:215–33.

[5] Kidane A. On the failure and fracture of polymer foam containing discontinuities. ISRN Mater Sci 2013;2013.

[6] Balzer JE, Siviour CR, Walley SM, Proud WG, Field JE. Behaviour of ammonium perchlorate-based propellants and a polymer-bonded explosive under impact loading. Proc R Soc A Math Phys Eng Sci 2004;460:781–806. doi:10.1098/rspa.2003.1188.

[7] Grote DL, Park SW, Zhou M. Dynamic behavior of concrete at high strain rates and pressures: I. experimental characterization. Int J Impact Eng 2001;25:869–86.

[8] Williamson DM, Siviour CR, Proud WG, Palmer SJP, Govier R, Ellis K, et al. Temperature–time response of a polymer bonded explosive in compression (EDC37). J Phys D Appl Phys 2008;41:085404. doi:10.1088/0022-3727/41/8/085404.

[9] Zhang QB, Zhao J. Effect of loading rate on fracture toughness and failure micromechanisms in marble. Eng Fract Mech 2013;102:288–309. doi:10.1016/j.engfracmech.2013.02.009.

[10] Zhou Z, Chen P, Duan Z, Huang F. Study on fracture behaviour of a polymer-bonded explosive simulant subjected to uniaxial compression using digital image correlation method. Strain 2012;48:326–32. doi:10.1111/j.1475-1305.2011.00826.x.

[11] Sutton MA, Li N, Joy DC, Reynolds AP, Li X. Scanning electron microscopy for quantitative small and large deformation measurements part I: SEM imaging at magnifications from 200 to 10,000. Exp Mech 2007;47:775–87.

[12] Kammers AD, Daly S. Digital image correlation under scanning electron microscopy: methodology and validation. Exp Mech 2013;53:1743–61.

[13] Huang JY, Li Y, Liu QC, Zhou XM, Liu LW, Liu CL, et al. Origin of compression-induced failure in brittle solids under shock loading. Phys Rev B 2015;92:144101.

[14] Lu L, Fan D, Bie BX, Ran XX, Qi ML, Parab N, et al. Note: Dynamic strain field mapping with synchrotron X-ray digital image correlation. Rev Sci Instrum 2014;85:076101. doi:10.1063/1.4887343.

[15] Bodelot L, Escobedo-Diaz JP, Trujillo CP, Martinez DT, Cerreta EK, Gray GT, et al. Microstructural changes and in-situ observation of localization in OFHC copper under dynamic loading. Int J Plast 2015;74:58–74.

[16] Sutton MA, Orteu JJ, Schreier H. Image Correlation for Shape, Motion and Deformation Measurements: Basic Concepts,Theory and Applications. Springer

Science & Business Media; 2009.

[17] Chu TC, Ranson WF, Sutton MA. Applications of digital-image-correlation techniques to experimental mechanics. Exp Mech 1985;25:232–44. doi:10.1007/BF02325092.

[18] Bornert M, Brémand F, Doumalin P, Dupré J-C, Fazzini M, Grediac M, et al. Assessment of digital image correlation measurement errors: methodology and results. Exp Mech 2009;49:353–70.

[19] Hurley RC, Lim KW, Ravichandran G, Andrade JE. Dynamic inter-particle force inference in granular materials: method and application. Exp Mech 2016;56:217–29.

[20] Sadd MH, Tai Q, Shukla A. Contact law effects on wave propagation in particulate materials using distinct element modeling. Int J Non Linear Mech 1993;28:251–65.

CHAPTER 3

LOCAL DEFORMATION AND FAILURE MECHANISMS OF POLYMER BONDED ENERGETIC MATERIALS SUBJECTED TO HIGH STRAIN RATE LOADING

[1]*Ravindran, S.*, Tessema, A., & Kidane, A. (2016). *Journal of Dynamic Behavior of Materials*, 2(1), 146-156. https://doi.org/10.1007/s40870-016-0051-9 Reused here with permission of publisher

3.1 ABSTRACT

The dynamic multi-scale deformation mechanism of polymer bonded energetic material is investigated. Samples made of polymer bonded sugar (a known simulate for polymer bonded explosives) with 85 % sugar crystals and 15 % polymer binder are used. The samples are dynamically compressed using a split Hopkinson pressure bar. Using a high magnification, meso-scale 2D digital image correlation experimental setup, the local deformation is measured in situ at sub-grain scale. The macroscale deformation mechanism is also investigated with the help of 3D digital image correlation. From the mesoscale experiment, it is observed that the local strain distribution in the specimen is highly heterogeneous with large strain localization occurring at the polymer rich areas between the crystal boundaries. Deformations of most of the crystals are minimal, and usually realign themselves to accommodate large deformation of the binder by rigid rotation and sliding. Due to this, delamination of the polymer binder from crystals and binder cracking are the main local failure modes. It is also observed that the presence of small crushed crystals from material processing are the favorable sites for this opening mode failure.

3.2 INTRODUCTION

Dynamic characterization is critical in granular materials, such as polymer bonded explosive (PBX), concrete, sand, armor protection materials etc., employed in extreme loading conditions. Especially in the case of polymer bonded explosives, understanding the failure mechanism under high strain rate loading is vital for safe use of these materials. PBXs typically contain 60–95 % of explosive solid loading and about 5–40 % of the soft polymer binder. Due to significant mismatch between the mechanical properties of the solid constituents and the soft polymer binder, the presence of inclusions, cracks, and voids

from the processing of the material, the failure mechanism of PBXs is complex and extended to multi-length scales. Quantifying the local deformation and failure initiation mechanisms of PBXs subjected to dynamic loading at meso-scale entails a deep understanding of the material response at much smaller length scales than macroscale measurements.

Optical methods, such as photoelasticity, digital speckle radiography, laser induced fluorescent speckle photography, and digital image correlation have been used in the past to understand the failure and fracture mechanics of PBXs subjected to dynamic loading [1–7]. Most of these studies are at macroscale and have provided much insight into the continuum scale high strain rate behavior of PBXs [2–10]. However, these experiments are inadequate to understand the local deformation mechanisms in highly heterogeneous PBX materials. On the other hand, high spatial resolution micro scale experiments have been proven to elucidate the local deformation mechanisms in these materials under quasi-static loading conditions [11,12]. Although high spatial resolution full field DIC measurements based on optical microscopes or scanning electron microscopes have been successfully implemented to measure local deformation in different materials at submicron scale under quasi-static loading conditions [12–18], high temporal resolution measurement with high spatial resolution are not established. Due to the absence of a suitable experimental method, the local behavior of these materials under dynamic loading conditions is not well understood although it is critically important. Recently an optical based meso-scale digital image correlation has been proposed that can be used to measure the local deformation in heterogeneous materials [13,19].

In this study, an experimental setup based on mesoscale digital image correlation is used and the local deformation and failure mechanisms in PBXs at high strain rate loading are investigated by measuring the local strain fields at sub-grain scale level. To the best knowledge of the authors, this is the first detailed work on understanding the local deformation of PBX by measuring strain at the sub-grain scale and at high temporal resolution. Macroscale experiments are also conducted and the failure mechanisms at macro and meso scales are compared.

3.3 MATERIALS AND METHODS

3.3.1 Material Preparation and Specimen geometry

The material used in this study is polymer bonded sugar (PBS), a known simulant of polymer bonded explosives. Sugar is far from representing the actual microstructural failure mechanisms of RDX and HMX, but is still an ideal and widely used simulant for the following reasons, (1) macroscopically the deformation behavior of polymer bonded sugar is similar to most polymer bonded explosives [20] and, (2) microscopically the monoclinic structure of sugar resembles the monoclinic crystalline structure of high melting point explosives (HMX) [21]. In addition, its simplicity and safety make sugar a convenient surrogate for explosive materials that can be tested in university laboratories and facilities. On the other hand, sugar is soluble in water therefore moisture and humidity can affect its mechanical and physical properties. In our work, proper care was taken to minimize the effect of moisture and humidity during fabrication and characterization process. Samples were cured in a vacuum assisted oven. Specimens were dry polished without the application of water. Experiments were conducted in a controlled atmosphere of temperature and humidity.

The formulation is composed of 85/10.8/2.89/1.31 wt % of sugar/Hydroxyl-terminated polybutadiene (HTPB)/di-octyl sebacate (DOS)/Toluene diisocyanate (TDI). HTPB is the monomer, DOS is the plasticizer and TDI is a curing agent. HTPB is a common binder material in polymer bonded explosives. To study the effect of loading rate on the failure behavior of PBX one should account for the strain rate sensitivity of the typical viscoelastic polymer used in PBX [22]. The goal of the current work, however, is not to study the effect of strain rate rather study the local deformation mechanism of PBX at a given loading rate by measuring the deformation in and across the boundary of the crystals. It is a first of its kind, and intentionally other parameters, such as strain rate are excluded.

Fabrication of the PBS specimens involves three major steps. First, the HTPB is mixed with the plasticizer (DOS) and curing agent (TDI). Then the sugar crystals are added to the blend and mechanically mixed thoroughly. It is then kept in a vacuum oven for 24 h at 60 °C, where the partial curing leads to the formation of a powdery mixture. Using a cylindrical mold of bore diameter 25 mm, the powder is then hydrostatically pressed at 90 MPa to cylindrical billets. These billets are completely cured by keeping them in the oven for 120 h and cooled naturally to room temperature. The specimens for the experiments are then machined from billets using a milling machine.

3.3.2 Experimental Setup

3.3.2.1 High Strain Rate Testing

The high strain rate compression experiments are performed using split Hopkinson pressure bar (SHPB) apparatus. Since the specimen used in the experiment is made of low impedance material, a soft polymer binder, polycarbonate bars are used as input and output

bars to minimize the impedance mismatch and obtain appreciable transmitted signals [23]. Both the incident and the transmitter bars are made of 1830 mm long and 25.4 mm diameter polycarbonate bar. To reduce the friction between the specimen and the bars, a thin layer of molybdenum disulfide is applied on the contacting surface. The waves in the incident and transmitter bars are measured with the help of strain gages located at the middle of the incident and transmitter bars. The average strain rate, strain and stress on the specimen are obtained using well-known equations,

$$\dot{e_s}(t) = -\frac{2C_b}{l_0}\varepsilon_R(t) \quad (3.1)$$

$$e_s(t) = \int_0^t \dot{e_s}(t)dt \quad (3.2)$$

$$\sigma_s(t) = \frac{E_a A_b}{A_s}\epsilon_T(t) \quad (3.3)$$

Where, $'l_0'$ is the original length of the specimen, $'\varepsilon_R(t)'$ is the time resolved strain of the reflected pulse in the incident bar and $'C_b'$ is the velocity of the wave in the bar. $'E_a'$is the elasticity modulus of the bar material, $'A_b'$ is the area of cross section of bar, $'A_s'$ is the area of cross section of specimen. It should be noted that the stress–strain plots are used to see the trend and are not critical for this study. Wave attenuation and dispersion in the bars are not corrected in the analysis.

3.3.2.2 High Speed Imaging

To observe the local deformation in situ, a high-speed camera equipped with high magnification extension tube is used. Figure 3.1a show the schematic representation and Figure 3.1b, shows the close-up picture of the actual setup used in the experiment. A high-speed camera SAX2, by Photron Inc., at a framing rate of 100,000 frames/s and at a resolution of 384 × 264 pixels is used. For high magnification imaging, an extension tube

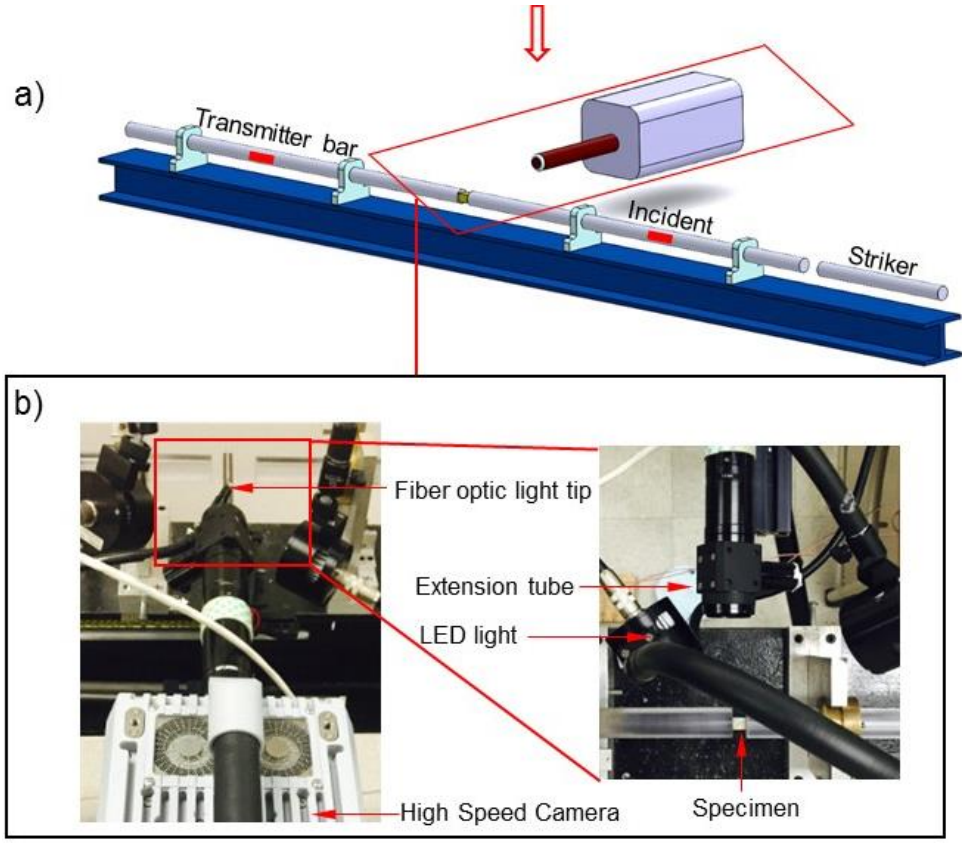

Figure 3.1(a) Schematic of the experimental setup, (b) The close-up image of the experiment setup.

from Navitar is used. The greatest challenges in obtaining images at high magnification and high rates are the low depth of field of the optical system and the need for high intensity illumination. For illumination, two high intensity LED lights and a fiber optic light tip was kept as close as possible to the specimen without obstructing the view of the camera as shown in Figure 3.1b. This illumination provides sufficient light to acquire the images, up to 180,000 frames per/second. An optical resolution of 10 µm/pixel is achieved using the proposed method, which is sufficient to obtain strain field inside a grain of size 400 µm using DIC. The macroscale deformation of the specimen is measured using stereovision system, comprised of two SAX2 high speed camera and two 100 mm lenses. In this case, two LED cold lights are used for illumination. The image acquisition rate is kept the same

as that of the mesoscale dynamic experiments. Details of the optical parameters used in the two systems can be found in Table 3.1.

Table 3.1 Experiment Resolution and Magnification

Experiment Details	*Macro*	*Meso*
Image Acquisition rate (frames/second)	100000	100000
Image Resolution (Pixels × Pixels)	384×256	384×256
Magnification	0.133X	2X
Pixel to length ratio (μm/pixel)	150	10
Field of view (mm × mm)	30.72×21.12	3.84×2.64
DIC algorithm	3D	2D

3.3.2.3 Specimen Geometry and Surface Preparation for Macro and Meso Scale DIC

To facilitate DIC measurement, a high contrast, random and isotropic speckle pattern has to be applied on the surface of the specimen. It is very important to choose the right size speckles according to the image resolution of the optical system and experimental setup. As a 'thumb of rule' for good displacement resolution and accuracy, every speckle has to be sampled by at least 3–5 pixels [24]. The image resolution for the macroscale experiment is 150 μm/pixel and, therefore, a speckle size of 500–800 μm is required. These speckles are achieved using an airbrush and flat paint. First, a thin layer of white paint is applied on the surface of the specimen, and after it has dried completely, a black paint was sprayed on the top of the white layer using an airbrush. The specimen dimensions and the speckle pattern for the macroscale DIC measurement are shown in Figure 3.2a.

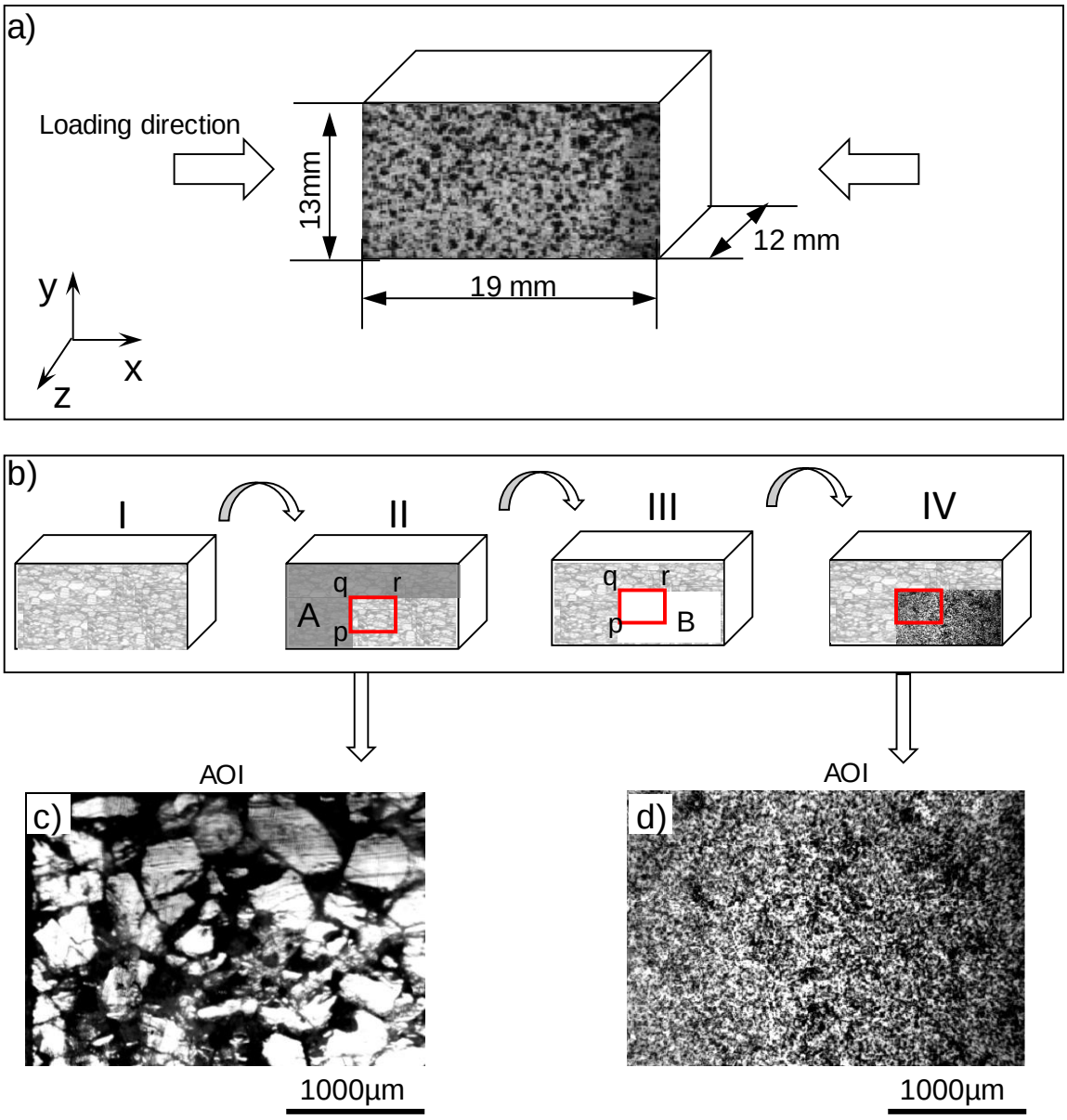

Figure 3.2 (a) Specimen dimension and speckle pattern for macroscale experiment, (b) Specimen dimension and steps involved in marking and speckling the area of interest (AOI) for the mesoscale experiment, (c) Microstructure of AOI, d) Speckle pattern of AOI.

For that matter, three major steps, polishing, marking, and speckling is followed as illustrated in Figure 3.2b. First, the specimen was dry polished with silicon carbide paper of grit size varying from 240 to 1200 and then finely polished with diamond particles of 3 µm. Secondly, in order to mark the AOI and obtain a microstructural image, the left and top part of the specimen is covered with scotch tape as L shape (A), as shown in Figure

3.2b (II), leaving the microstructure of the right bottom side of the specimen accessible for imaging and speckling. Note that the right edge of the vertical scotch tape (pq) and the bottom edge of the horizontal scotch tape (qr) are used as a reference, during imaging both the microstructure and DIC images. The image of the microstructure is captured covering entire the field of view of the area of interest marked with red rectangle shown in Figure 3.2b (II). The microstructure of the AOI is shown in Figure 3.2c. In step three, the AOI is speckled for DIC measurements. In order to speckle the specimen, first, a thin layer of white paint was applied, using an airbrush, on the specimen surface covering the AOI, and allowed to dry partially. Then a black toner powder is deposited on top of the partially dried white paint, by blowing the powder onto the surface using an air gun and allowed to dry completely. Finally, the scotch tape was peeled off, which gave speckle patterns of AOI shown in Figure 3.2b (IV), d.

3.3.2.4 Post Processing of Macro and Meso Scale DIC

Using these speckled specimens both the macro and meso scale experiments are conducted, while images are taken in situ. The camera system was triggered with the help of oscilloscope and strain gages attached on the input bar. Using the camera delay time feature, the duration of the trigger is adjusted to capture images prior (reference image) and after deformation. The reference and the consequence images are then imported for further post-processing following a well-documented procedure available in the literature [24–26]. For macroscale strain field measurement, the images are processed using Vic3D, commercial digital image correlation software by correlated solutions Inc. As mentioned above the resolution of the macroscale experiment is 150 µm/pixel and the average speckle size is 600 µm. Hence, subset sizes of 1.95×1.95 mm^2 are used, considering a minimum

of 3 × 3 speckles in one subset. Strain calculation in this study is done with the exhaustive search mode, which enables the highest amount of data recovery when correlation fails, at the expense of processing time [24]. A higher order interpolation function (Optimized 8-tap) is used to convert discrete digital data points to continuous data. The correlation criterion was chosen to be zero normalized, which is insensitive to the scaling of light intensity. Similarly, in the case of mesoscale strain field calculation a commercial 2D digital image correlation software, Vic 2D, is used. The strain calculation, in this case, was done with the exhaustive search mode similar to the macroscale. However, a subset size of 110×110 μm^2 is employed in this case which enables to have at least ~14 subsets in one grain of 400 μm size.

The proposed surface measurement cannot provide detailed failure mechanisms that occur below the considered plane. Especially, it is difficult to tell where the failure initiated, an interesting subject but out of the scope of the current work. On the other hand, the strain localization and the deformation profiles in and across the boundary of the crystals are investigated, by locally measuring the deformation on the binder and crystals in the same plane. The images are captured on a plane perpendicular to the loading direction. Considering the loading and boundary conditions in a Hopkinson bar experiment, it is reasonable to assume that, macroscopically, the deformation is uniform across the thickness of the specimen. This is the basic assumption of Hopkinson Pressure bar experiment. The proposed local measurements will show that the deformation is heterogeneous locally, whilst being uniform macroscopically. In addition, the surface measurements, in conjunction with the underlying microstructure can give information

about the interaction and propagation of strains between the binder and crystals, which is the main objective of the current work.

It was also found that the effect of subsurface deformation on the measured surface deformation is negligible, in the early stages of the loading. The specimens are unconfined and free to expand in the out of plane direction. If there is out of plane motion due to subsurface deformation, the captured images would have been out of focus, as the depth of field of the microscope is very small. Fortunately, we haven't observed such a large effect during the early stage of the deformation and all the images correlate well. However, once failure initiated, the images are no longer in focus and could not be used for digital image correlation. So, it is reasonable to assume that the early stage of deformation is one dimensional and the deformation fields presented in this work can representative the deformation profile across the thickness of the specimen.

3.4 RESULT AND DISCUSSION

3.4.1 Macro Scale Deformation Behavior

Typical stress-strain relation of PBS subjected to dynamic loading is shown in Figure 3.3a. The strains calculated based on the strain gage readings and obtained from 3D DIC are compared in Figure 3.3b. The values are comparably close to each other especially in the early stage of deformation; however, there is a small variation in the later deformation stage of the material, which could be due to the variation of the strain field due to speckle cracking once the failure initiation occurs in the material. To check the stress equilibrium on the flat specimen tested at the macroscopic scale, three wave and single wave analysis are performed. As shown in Figure 3.3, stress obtained from the three-wave

analysis oscillates around the stress obtained from the one wave analysis indicating reasonable stress equilibrium in the specimen.

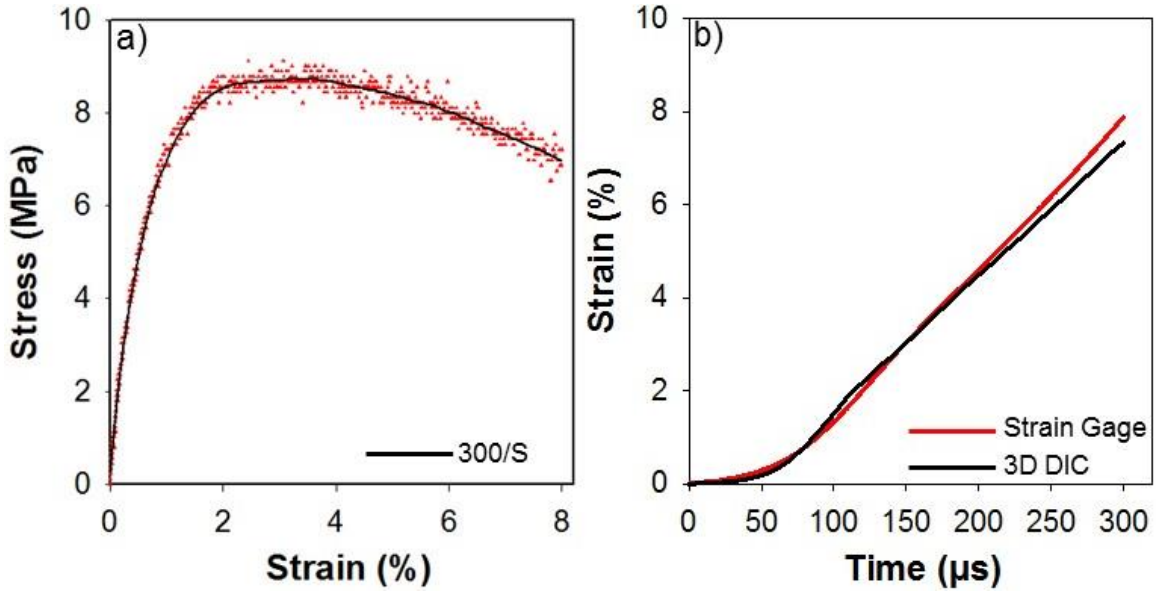

Figure 3.3 (a) Stress strain curve for PBX at 300 s^{-1}, (b) Comparison of DIC strain measurement with the strain gage measurement.

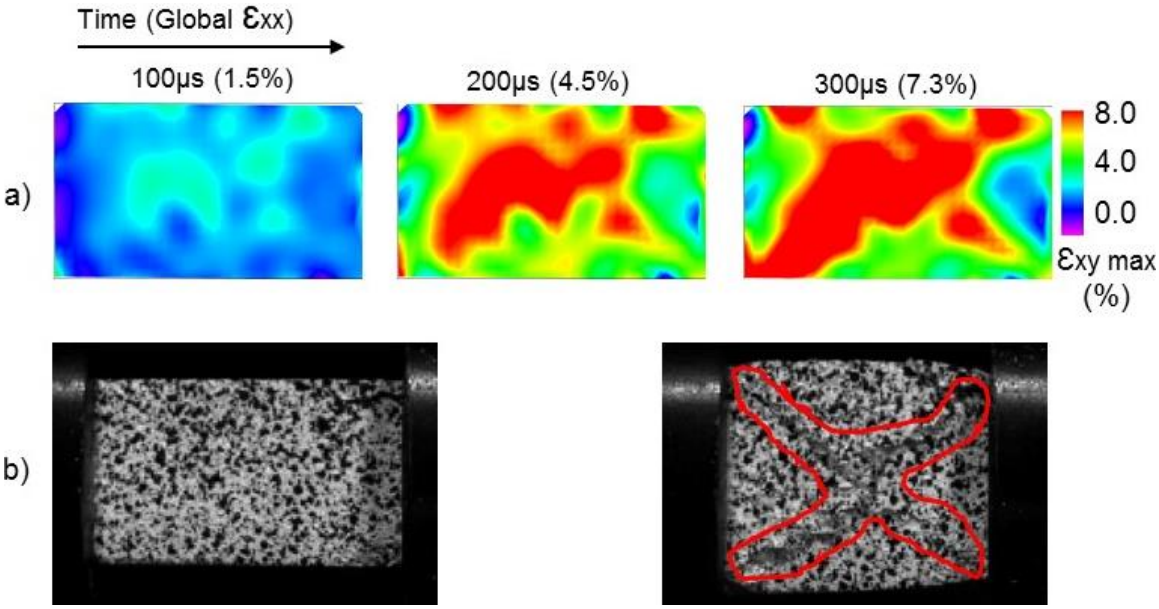

Figure 3.4 (a) Maximum shear strain in the material at 100μs, 200μs, 300μs, (b) Specimen in undeformed state and failure state.

Figure 3.4b shows the contour plot of maximum shear strain fields as a function of time obtained from macroscale DIC. It is clearly visible that at 200 μs, high shear strain localization is started at each corner of the specimen and later merged into the center of the specimen leading to shear band failure. The shear band formation is clearly visible in the fracture specimen shown in Figure 3.4b. Apart from observing the macroscale shear band formation, it was impossible to look into the local deformation mechanism at this scale. The onset of local deformation mechanism is observed in the mesoscale experiment and discussed in the next section.

3.4.2 Mesoscale Deformation Behavior

Highly heterogonous deformation is apparent in the PBS sample tested, and the experimental method employed was able to capture these local strain fields accurately. Figure 3.5 shows typical local axial, lateral and shear strain fields in the PBS specimen subjected to dynamic compressive loading. It is distinctly visible that, the local compressive strain in some regions reach as high as 8 % for the global axial strain of only about 0.5 %. Similar observations have been made in the meso scale computational study of polytetrafluoroethylene-Al-W granular composites under dynamic loading conditions [27]. The strain localization is prevailing around crystal boundaries, rich in the polymer, and it is presumable that most of the deformation was accommodated by the deformation of the soft polymer binder while crystals realign themselves to accommodate the deformation. This could be the reason that the stress-strain plot has extended deformation after the yield. Furthermore, from the lateral strain field shown in Figure 3.5b, it is clearly seen that the local deformation occurs at an angle close to $\pm 45^0$, indicating local shear band formation is also captured in the experiment.

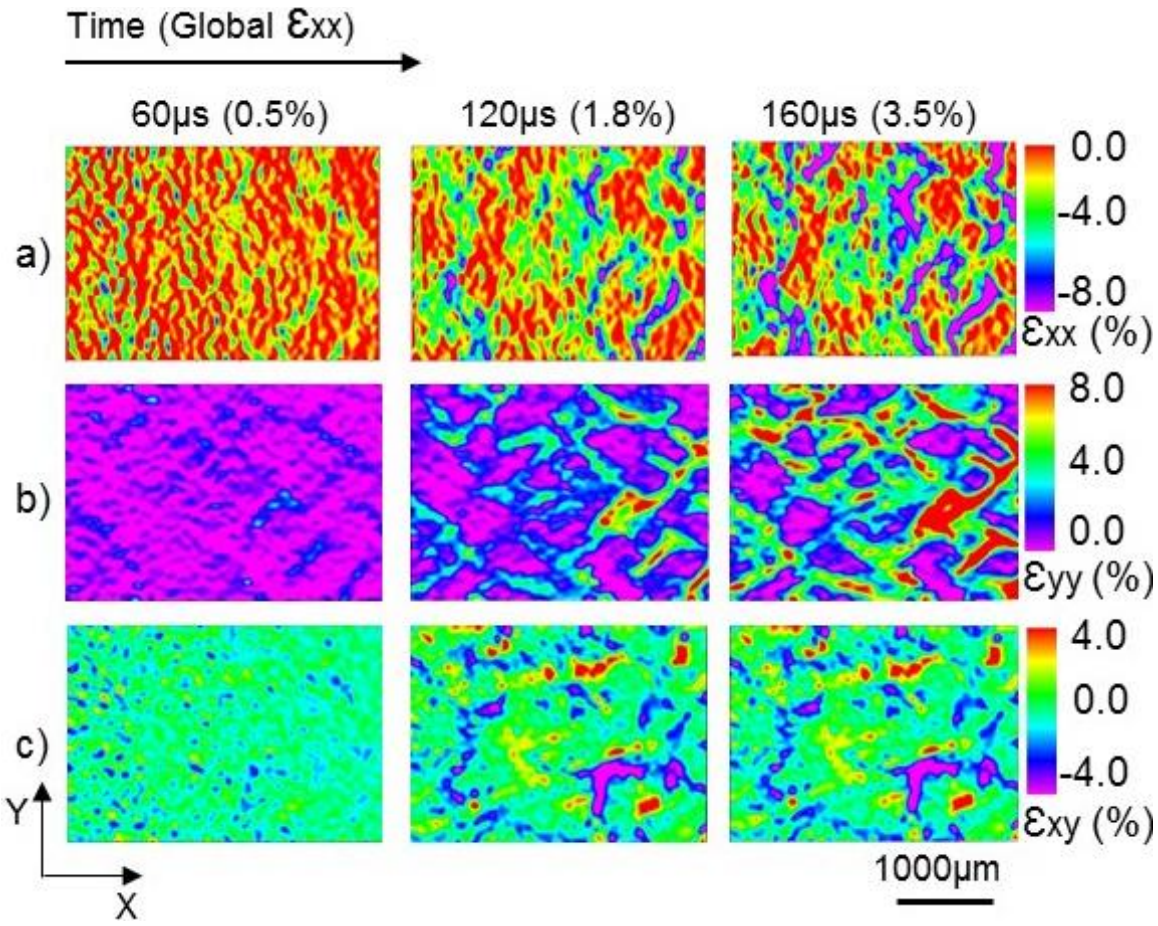

Figure 3.5 Local strain at different time (60μs, 120 μs, 160 μs) and global axial strains (0.5%, 1.8%, 3.5%), (a) local axial strain field, (b) local transverse strain field, (c) local shear strain field.

In order to understand these effects better, the local strain fields were compared with the underlying microstructure taken before the deformation as shown Figure 3.6. It is shown that, in most cases, the axial strain localization occurs at the vertical or low angle interfaces with thick binder interface, where there are no crystal–crystal contacts or adjust crystals are far away from each other, for example between Crystal 3 (C3) and Crystal 11 (C11), between Crystal 4 (C4) and Crystal 9 (C9), between Crystal 7 (C7) and Crystal 5 (C5), between Crystal 8 (C8) and Crystal 6 (C6), between Crystal 10 (C10) and Crystal 14 (C14) etc. It can be seen that the crystals C5, C6, C9, C11, C12 and C13 C14 C15 are in contact and the strain localization observed at the interface between these crystals are

minimal due to the absence of polymer binder. It is visible that the axial strain field in these crystal interfaces are small and reasonably continuous compared to the crystals with rich polymer binder interface. But there are cases where the crystals are surrounded by polymer but there is no substantial strain localization, for example between Crystal 5 (C5) and Crystal 10 (C10), between Crystal 6 (C6) and Crystal 10 (C10) and between Crystal 5 (C5) and Crystal 9 (C9). This indicates the possibility of force chains in the material, and there might be some crystals that form favorable paths for the load transfer mechanism. The speculated force chains are based on the continuity of the compressive strain across the specimen length and are in crystals either in contact or very close to each other, which agrees well with the fact that as the solid loading increases it results in permanent stress bridging [28]. However, considering the percentage of solid loading used in the specimen, additional work is needed at different solid volume fraction to reach a conclusive observation on the force chain formation in the material.

It is important to note that the lateral strain localization occurred at grain boundaries that are at an angle about ± 45^{o} with respect to the loading direction. Very high tensile strain, up to 8 %, has been seen at a small global compressive strain of 0.5 %. Figure 3.6c shows the comparison of the local transverse strain field with microstructure shown in Figure 3.6a. It is shown that the strain localization is substantial in the polymer binder rich area (marked in a black rectangle in Figure 3.6c). This area is formed by collections of small crystals bound together by the polymer binder and surrounded by large crystals, which potentially form a weak region for tension. It is also visible that the lateral strain around this region extends to the boundary of the specimen, indicating the possibility of either binder delamination around the crystal or/and crystal cracking, which will be further

discussed in the next section. The local shear strain field is also significantly localized at the boundaries and prevalent at the weak polymer-rich region. The high shear localization could cause the sliding of the crystal over another and crystal rotation.

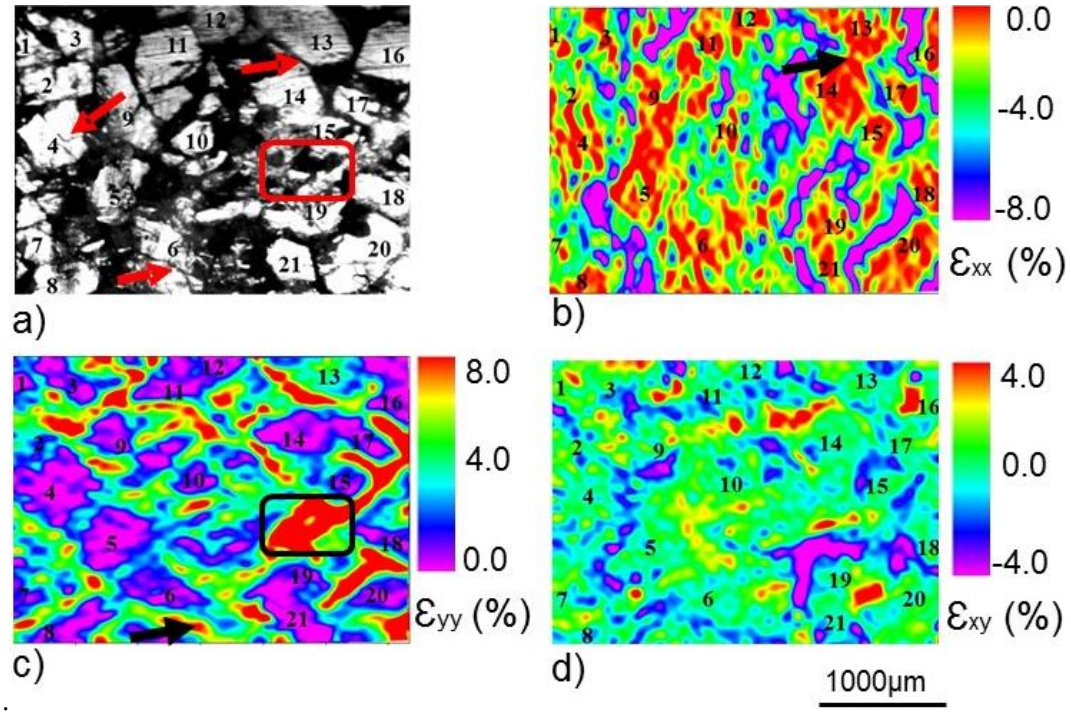

Figure 3.6 (a) Microstructure with crystal numbering, (b) local axial strain field with crystal numbering, (c) local transverse strain field with crystal numbering, (d) local shear strain field with crystal numbering

3.4.2.1 Crystal Fracture

One of the major failure mechanisms of PBS observed in this experiment is crystal fracture. As shown in Figure 3.6c, a large strain value is clear on or across some crystals, such as C2, C9, C6, and C13. The strain on this crystal is as high as 4 %. However, the sugar crystal used in this experiment is brittle and will not be able to deform to a strain of order 3–4 % without fracture. This indicates that some of the crystals undergo fracture. Crystals C9 and C13 are relatively large, which is a favorable condition for crystal fracture

if it is surrounded by large crystals. In such cases, the number of crystal to crystal contact points will be less, which essentially reduces the chances of force distribution through more contact points and hence increases the probability of stress concentration. It is distinctly visible from the Figure. 3.6a that C14 and C13 have a single point contact, where a sharp corner of C14 hitting C13. Consequently, these conditions cause stress concentration and finally fracturing of C13. Similar observations can be made on C2 and C9 as well. Whereas, in the case of C6, an initial crack formed from the preparation of the material is visible, see Figure 3.6a (red arrow on C6). Fracture of crystals during material preparation is common [29]. This initial crack starts to grow as loading progress and leads to fracture C6. It is very interesting to note that C4 also has an initial crack as of C6, as indicated in Figure 3.6a by an arrow, but there is no further fracture of the crystal is observed. This could be either the disengagement of C4 in the load transfer mechanism due to a large region of binder ahead of the crystal, possible force chain mechanism or rigid body rotation. Nevertheless, it indicates that increasing the polymer binder will effectively reduce the probability of crystal fracture due to crystal–crystal contact.

3.4.2.2 Crystal Rotation

Another deformation mechanism observed in this experiment is crystal rotation and sliding. Crystal rotation and sliding have been observed in granular materials under quasi-static and dynamic loading conditions in the past [30,31]. Figure 3.7 shows the rotation of each crystal as a function of loading time. The magnitude and direction of rotation vary from grain to grain, and crystal rotation as high as 3.2° is measured (see Table 3.2). It is also observed that, in some cases, two or more grains form a group and rotate together up to a certain loading time. For example, C12 and C11 form a pair and rotate together up to

a time of 200 μs in a clockwise direction. There is no relative rotation between C11 and C12 until this time. C1, C2, and C3 have also formed groups and rotate in the same direction. On the other hand, some crystals in contact with another rotating crystal are shown to be stationary or rotates in a different direction, which could create sliding and friction between the adjacent crystals. For example, C4, which is in contact with C2, does not rotate significantly, which could cause potential sliding friction with C2. In addition, relative rotation between the adjacent crystals can cause delamination at the interface and could be a potential failure mode in PBX.

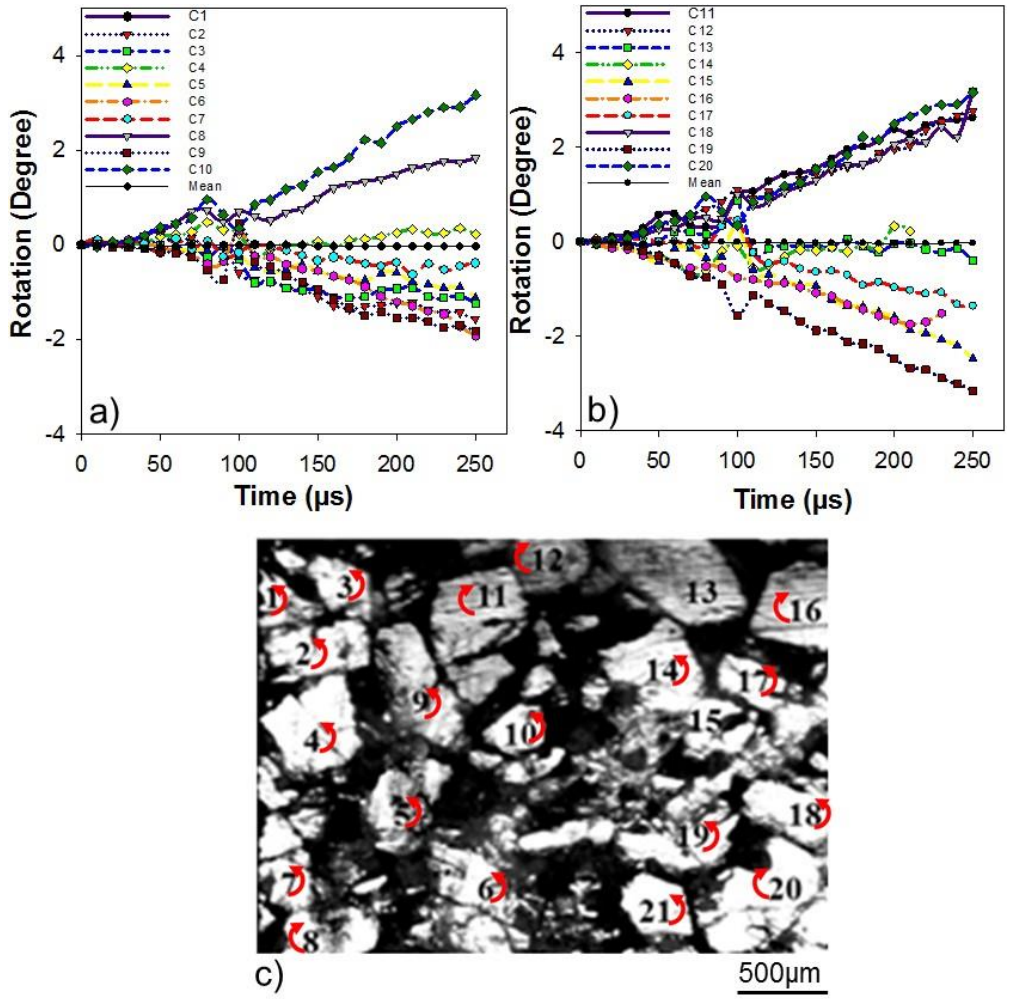

Figure 3.7 Rotation of crystals with time (a) From crystal number 1-10, (b) From crystal 11-21, (c) Microstructure and the rotation direction of the crystals.

Table 3.2 Magnitude and direction of crystals rotation

Crystals	**Rotation direction**	**Max. Rotation (Degree)**	**Min. Rotation (Degree)**	**Mean Rotation (Degree)**
C1, C2, C3,C4,C5,C6 ,C7,C9,C14, C19,C18,C21	Clock Wise	C21-3^o, C17-2.5^o C6-2^o	C4,C14 & C16 = 0.2^o	0.03^o
C8, C10,C20,C11,C12	Anti-clockwise	C10-3.2^o, C20- 3.2^o, C11 & C12-3.2^o		

3.5 CONCLUSION

An experimental method has been developed to investigate the local deformation mechanism in PBX under dynamic loading conditions by the employed high-speed camera along with high magnification extension tube. To the knowledge of the authors, for the first time, quantitative data at a spatial resolution of 10 μm/pixel and at a framing rate of 100,000 frames/second is achieved. Based on the macro and meso scale experiments the following points are summarized.

1. Macro scale experiments showed that under dynamic loading conditions the PBS fracture by shear band formation and the shear band formation started around 6 % of global axial strain.
2. From the mesoscale experiments, different deformation mechanisms are observed.
   a) The strain is highly localized in the interface region with a thick polymer binder, while the crystals either rotate or realign themselves to accommodate deformation in the binder.

b) Crystals with direct multi-point contact with their neighbor crystal are unlikely to undergo large deformation.

c) On the other hand, crystals either with initial crack or in direct point contact with the neighbor crystal are seen to undergo fracture.

d) The lateral strain is highly visible in areas where small crushed crystals are bonded together, indicating a potential spot for opening-mode fracture initiation.

3.6 LIST OF REFERENCES

[1] Roessig KM. Mesoscale mechanics of plastic bonded explosives. AIP Conf. Proc., IOP INSTITUTE OF PHYSICS PUBLISHING LTD; 2002, p. 973–8.

[2] Peterson PD, Mortensen KS, Idar DJ, Asay BW, Funk DJ. Strain field formation in plastic bonded explosives under compressional punch loading. J Mater Sci 2001;36:1395–400.

[3] Zhou Z, Chen P, Duan Z, Huang F. Study on Fracture Behaviour of a Polymer-Bonded Explosive Simulant Subjected to Uniaxial Compression Using Digital Image Correlation Method. Strain 2012;48:326–32.

[4] Prentice HJ, Proud WG, Walley SM, Field JE. The use of digital speckle radiography to study the ballistic deformation of a polymer bonded sugar (an explosive simulant). Int J Impact Eng 2010;37:1113–20.

[5] Siviour CR, Grantham SG, Williamson DM, Proud WG, Field JE. Novel measurements of material properties at high rates of strain using speckle metrology. Imaging Sci J 2009;57:326–32.

[6] Siviour CR, Grantham SG. High resolution optical measurements of specimen deformation in the split Hopkinson pressure bar. Imaging Sci J 2009;57:333–43.

[7] Field SGG and CRS and WGP and JE. High-strain rate Brazilian testing of an explosive simulant using speckle metrology. Meas Sci Technol 2004;15:1867.

[8] Siviour C., Laity P., Proud W., Field J., Porter D, Church P., et al. High strain rate properties of a polymer-bonded sugar: their dependence on applied and internal constraints. Proc R Soc A Math Phys Eng Sci 2008;464:1229–55.

doi:10.1098/rspa.2007.0214.

[9] Balzer JE, Siviour CR, Walley SM, Proud WG, Field JE. Behaviour of ammonium perchlorate-based propellants and a polymer-bonded explosive under impact loading. Proc R Soc A Math Phys Eng Sci 2004;460:781–806. doi:10.1098/rspa.2003.1188.

[10] Drodge DR, Williamson DM. Understanding damage in polymer-bonded explosive composites. J Mater Sci 2016;51:668–79.

[11] Rae PJ, Palmer SJP, Goldrein HT, Field JE, Lewis AL. Quasi-static studies of the deformation and failure of PBX 9501. Proc R Soc A Math Phys Eng Sci 2002;458:2227–42. doi:10.1098/rspa.2002.0967.

[12] Ravindran S, Kidane A. Meso-Scale Deformation Behavior of Polymer Bonded Energetic Material Under Quasi-Static Compression. Mech. Compos. Multi-functional Mater. Vol. 7, Springer; 2016, p. 345–50.

[13] Ravindran S, Tessema A, Kidane A, Sutton MA. Meso-scale Deformation Mechanisms of Polymer Bonded Energetic Materials Under Dynamic Loading. Mech. Compos. Multi-functional Mater. Vol. 7, Springer; 2016, p. 451–6.

[14] Koohbor B, Ravindran S, Kidane A. Meso-scale strain localization and failure response of an orthotropic woven glass–fiber reinforced composite. Compos Part B Eng 2015;78:308–18.

[15] Ravindran S, Koohbor B, Kidane A. On the Meso-Macro Scale Deformation of Low Carbon Steel. Adv. Opt. Methods Exp. Mech. Vol. 3, Springer; 2015, p. 409–14.

[16] Sutton MA, Li N, Joy DC, Reynolds AP, Li X. Scanning electron microscopy for

quantitative small and large deformation measurements part I: SEM imaging at magnifications from 200 to 10,000. Exp Mech 2007;47:775–87.

[17] Kammers AD, Daly S. Digital image correlation under scanning electron microscopy: methodology and validation. Exp Mech 2013;53:1743–61.

[18] Zhou Z, Chen P, Huang F, Liu S. Experimental study on the micromechanical behavior of a PBX simulant using SEM and digital image correlation method. Opt Lasers Eng 2011;49:366–70.

[19] Ravindran S, Tessema A, Kidane A. Note: Dynamic meso-scale full field surface deformation measurement of heterogeneous materials. Rev Sci Instrum 2016;87:36108.

[20] Liu C. On the minimum size of representative volume element: an experimental investigation. Exp Mech 2005;45:238–43.

[21] Asadi M. Beet-sugar handbook. John Wiley & Sons; 2006.

[22] Gray III GT, Blumenthal WR, Idar DJ, Cady CM. Influence of temperature on the high-strain-rate mechanical behavior of PBX 9501. tenth Am. Phys. Soc. Top. Conf. Shock compression Condens. matter, vol. 429, AIP Publishing; 1998, p. 583–6.

[23] Zhao H, Gary G, Klepaczko JR. On the use of a viscoelastic split hopkinson pressure bar. Int J Impact Eng 1997;19:319–30. doi:10.1016/S0734-743X(96)00038-3.

[24] Sutton MA, Orteu JJ, Schreier H. Image Correlation for Shape, Motion and Deformation Measurements: Basic Concepts,Theory and Applications. Springer Science & Business Media; 2009.

[25] Mallon S, Koohbor B, Kidane A, Sutton MA. Fracture behavior of prestressed

composites subjected to shock loading: a DIC-based study. Exp Mech 2014;55:211–25.

[26] Koohbor B, Mallon S, Kidane A, Sutton MA. A DIC-based study of in-plane mechanical response and fracture of orthotropic carbon fiber reinforced composite. Compos Part B Eng 2014;66:388–99.

[27] Herbold EB, Nesterenko VF, Benson DJ, Cai J, Vecchio KS, Jiang F, et al. Particle size effect on strength, failure, and shock behavior in polytetrafluoroethylene-Al-W granular composite materials. J Appl Phys 2008;104:103903.

[28] Barua A, Horie Y, Zhou M. Microstructural level response of HMX–Estane polymer-bonded explosive under effects of transient stress waves. Proc. R. Soc. London A Math. Phys. Eng. Sci., vol. 468, The Royal Society; 2012, p. 3725–44.

[29] Hu Z, Luo H, Bardenhagen S, Siviour C, Armstrong R, Lu H. Internal Deformation Measurement of Polymer Bonded Sugar in Compression by Digital Volume Correlation of-Tomography. Exp Mech 2015;1:289–300.

[30] Kuhn MR, Bagi K. Contact rolling and deformation in granular media. Int J Solids Struct 2004;41:5793–820.

[31] Tordesillas A, Muthuswamy M, Walsh SD. Mesoscale measures of nonaffine deformation in dense granular assemblies. J Eng Mech 2008;134:1095–113

CHAPTER 4

MULTISCALE DAMAGE EVOLUTION IN POLYMER BONDED SUGAR UNDER DYNAMIC LOADING

[1] *Ravindran, S.*, Tessema, A., & Kidane, A. (2017). *Mechanics of Materials*, 114, 97-106. https://doi.org/10.1016/j.mechmat.2017.07.016 Reused here with permission of publisher

4.1 ABSTRACT

High-speed and high spatial resolution digital image correlation-based experiments are performed to understand the sub grain level local failure mechanisms in highly filled composites under dynamic loading. Polymer bonded sugar that mimics the mechanical properties of a polymer bonded explosives (highly filled composite) is used in this study. The experiments are conducted in a split Hopkinson pressure bar setup at an intermediate strain rate. In polymer bonded sugar, high strain localization was observed predominantly in the region filled by the polymer binder surrounding the sugar crystals. The damage evolution was quantified by calculating the Poisson's ratio and volumetric strain as a function of loading. It was observed that the damage incubation is started at a very small global strain and causes mechanical softening in the material that leads to shear band formation. Also, the possible hotspot mechanism in the material was seen to be frictional heating of the crack faces and de-bonding of the polymer binder.

4.2 INTRODUCTION

Polymer bonded explosives (PBX) are highly filled heterogeneous composites which contain 80-95% of polycrystalline explosives crystals (RDX, HMX, for instance.) bound together by 5-20% of rubbery polymer binder (HTPB, Estane, for instance). These materials are subjected to dynamic loading at a range of strain rates, during manufacturing, machining, and transportation. These loading can cause severe damage and formation of hot spots [1–3], that can lead to deflagration of the material, which in turn affects the safety and chemical stability of PBX. The most numerical simulation shows that the grain scale strain localization due to heterogeneity in the microstructure, material property mismatch between the binder and explosive crystal, the existence of defects such as voids, cracks and

inclusions play a major role in the local failure and formation of hot spots [2, 4–12]. However, these observations are limited to computational experiments.

On the other hand, continuum scale high temporal resolution *in-situ* experiments have provided much insight into the macro scale deformation behavior of PBX [13–16]. It was shown that even a low amplitude insult can lead to ignitions and violent explosions in PBX [16]. With the help of high-speed photography and heat sensitive films, observation has been made on the macroscale shear band formation in PBX and which is considered as the prime reason for such behavior [2, 14]. However, the macros scale experiments cannot resolve the mechanisms that cause shear banding and hot spot formation. It is well known that thermal softening due to large strain (10-50% strain) deformation is responsible for the formation of the shear band in most materials under dynamic loading [17]. However, in PBX shear bands are observed at a strain far below the strain required for thermal softening. Computationally, it is shown that the mechanical softening due to local failure can lead to shear bands in PBX at small strain. The shear bands formed due to mechanical softening are wider in size compared to shear bands due to thermal softening [12]. Wide shear bands cannot produce hot spots, which again brings to the question that what is the main causes for the formation of a hot spot in PBX at small strain.

Meso scale computational studies showed that plastic heating due to strain localization in the polymer binder and frictional heating due to cracking of the crystals are the leading mechanisms for the formation of the hotspots in PBX under dynamic loading conditions [7– 9]. Due to the complexity of the required experimental setup and limitations in obtaining images at high resolution at high speed, experimental observations of such phenomenon were scarce. Recently the authors utilized and demonstrated a digital image

correlation (DIC) based experiment to measure the local strain fields in PBX under dynamic loading [19–22]. It was found that the local deformation of PBS is highly heterogeneous, and the heterogeneity is predominately localized in the binder region between crystals while the crystals are mainly rotating or moving rigidly without much deformation. It is also observed that pre-existing cracks in the crystals grow depending on the engagement of crystals in the load transferring mechanism in the material during loading. However, the reason behind such a phenomenon and the main local damage incubation mechanism was not clear. In this study, using the recently developed method, the local damage initiation mechanism in PBX is investigated. Polymer bonded sugar specimen is used in this study. The deformation mechanisms, failure process and its evolution with time are investigated and discussed in detail.

4.3 MATERIALS AND METHODS

4.3.1 Material Preparation and Specimen geometry

Polymer bonded sugar (PBS), an inert simulant of polymer bonded explosives (PBXs) was used in this study. PBS contains sugar crystals of sizes varying from 100-600 μm and plasticized hydroxyl terminated polybutadiene (HTPB) binder. The composition of the PBS is given Table 4.1. PBS was prepared in several steps: first, the HTPB (monomer) was mixed with the di-octyl sebacate (plasticizer) and toluene diisocynate (curing agent), followed by the addition of sugar crystals. The heterogeneous composition of sugar and the polymer was mixed thoroughly in order to coat the surface of the sugar crystals with the polymer binder. Then, the mixture was kept in an oven for partial curing at 70 ^{o}C for about 16 hours. This process helps in activating the binding properties of the

coated polymer. The partially cured mixture was pressed at 90 MPa in a steel mold of 25.4 mm diameter at room temperature. Finally, these sample billets were heat treated at 70 ^{o}C for 96 hours to completely cure the samples. For the dynamic experiments, the specimens of rectangular geometry with dimensions close to 19×12×12 mm, shown in Figure 4.1a, were machined from the cured cylindrical billets.

Table 4.1Composition of PBS

Sugar (% wt)	HTPB (% wt)	Di-Octyle Sebacate (% wt)	Toluene diisocynate (% wt)
85	10.8	2.89	1.31

The extracted samples were dry polished using silicon carbide grit papers with grit size varying from 240-1200 to reveal the microstructure. The microstructural image of the area of interest (AOI) shown in Figure 4.1b was captured using an optical microscope prior to speckling of the specimen. Speckles must be applied to the specimen in order to facilitate the AOI for strain measurement using DIC. The speckling was performed by the following procedure: a thin layer of white paint was applied on the specimen covering the entire AOI, prior to the drying of the paint, a small amount of black toner powder (particle size 1040μm) was deposited on the surface using an airbrush. After the drying of the paint, the speckled surface was air blasted to confirm the adherence of particles to the paint. The speckle pattern obtained using this method is shown in Figure 4.1c. Note that, the gray intensity of the speckle pattern image follows a bell-shaped curve shown in Figure 4.1d, which is suitable for strain calculation using DIC.

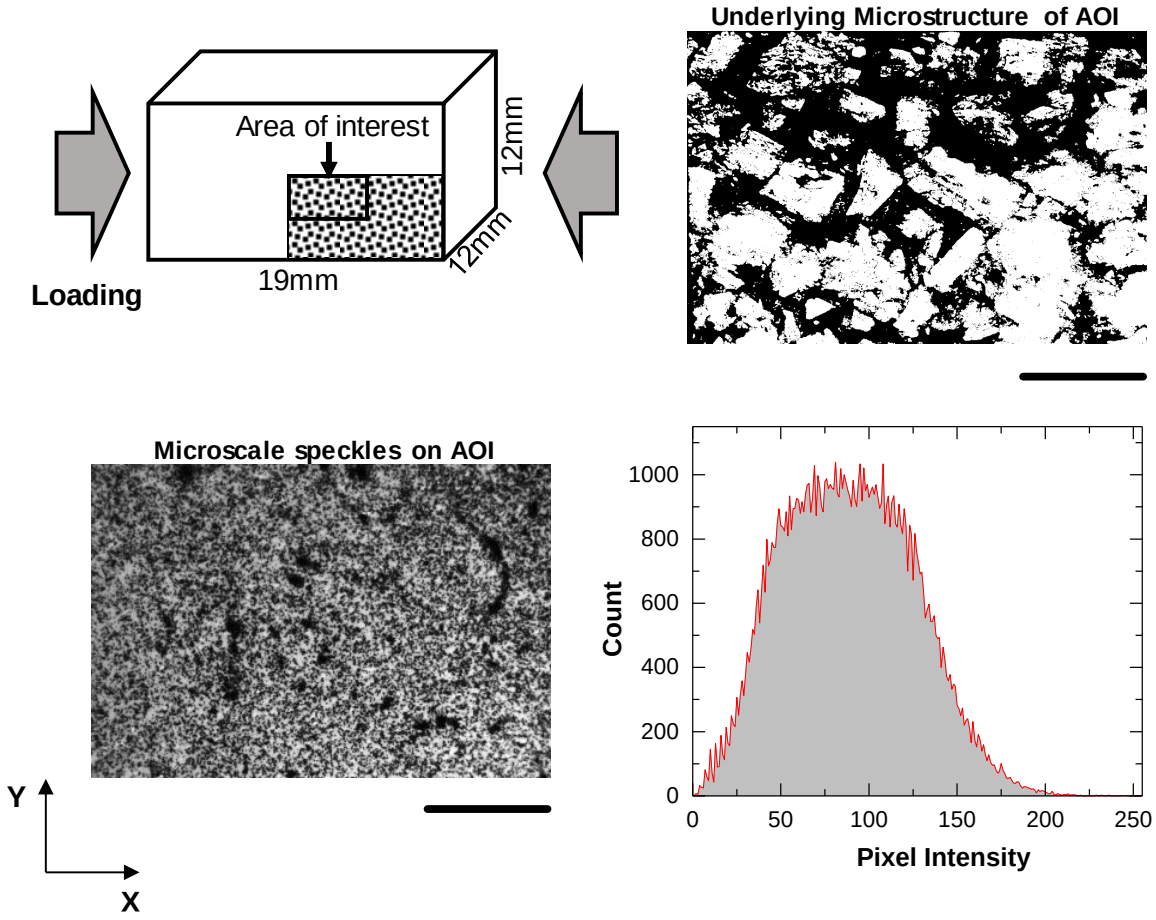

Figure 4.1 (a) Specimen geometry and Area of interest (AOI), (b) Microstructure of PBS-8501 at AOI, (c) Speckle at AOI. (d) Pixel intensity shows a bell-shaped curve indicates a suitable pattern for DIC.

4.4 EXPERIMENTAL SETUP

A complete schematic diagram and a close-up image of the experimental setup used in this study is shown in Figure 4.2. Dynamic uniaxial compression of the samples was performed in a classic compression split Hopkinson bar setup (SHPB). It comprises of two polycarbonate bars of circular cross section, gas-gun, and a launching barrel. The incident and transmitter bars were of 25.4 mm in diameter and 1830 mm in length. A striker bar of length 800 mm was used to achieve a wide incident pulse which helps in loading the sample for the large strain. To acquire the incident, reflected and transmitted signals, two strain

gages were attached diametrically opposite at the middle of the incident and transmitter bar. These strain gages were connected to a strain amplifier, and the data from the amplifier was recorded in an oscilloscope.

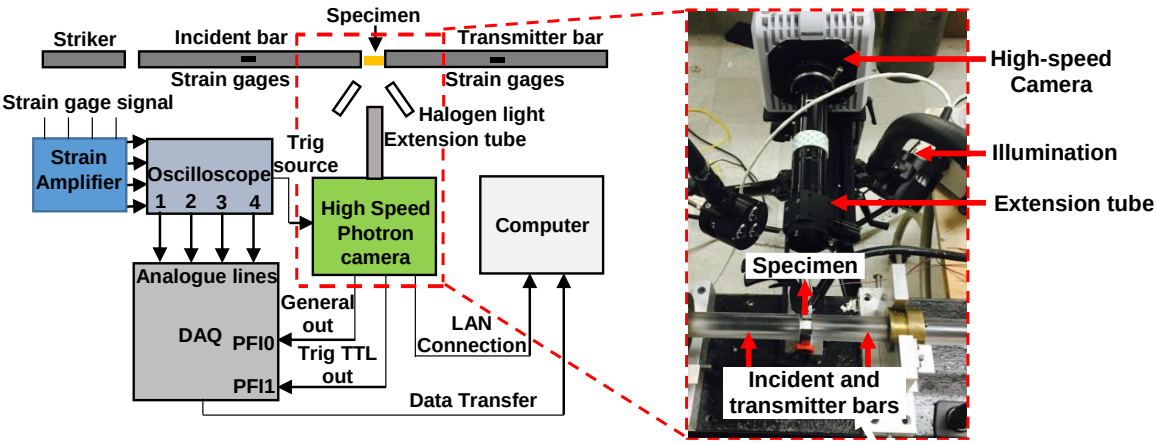

Figure 4.2 Schematic of experiment setup for the mesoscale dynamic experiment

To perform the experiments, the specimens were sandwiched between the incident and transmitter bars. A thin layer of lithium grease was applied at the interface between the specimen and bars to reduce the friction. The dynamic compressive wave was generated in the incident bar by propelling the polycarbonate projectile through a lunching tube into the incident bar using a gas-gun. During the experiment, the oscilloscope was triggered when the strain signal reached the location of the strain gages on the incident bar and recorded the strain history. These strain signals were used to calculate the global axial strain, strain rate, force and stress induced in the specimen using well-known equations shown below,

$$\text{Specimen strain rate, } \dot{\varepsilon}_s = \frac{-2C_b}{l}\varepsilon_r(t) \tag{4.1}$$

$$\text{Specimen axial strain, } \varepsilon_s = \int_0^t \frac{-2C_b}{l}\varepsilon_r(t) \tag{4.2}$$

$$\text{Incident force, } F_i = EA_b[\varepsilon_i(t)+\varepsilon_r(t)] \tag{4.3}$$

$$\text{Transmitter force, } F_t = EA_b\varepsilon_t(t) \tag{4.4}$$

For $F_i=F_t$, force equilibrium, the stress in the specimen can be calculated as,

$$\text{Stress in the specimen, } \sigma_S = \frac{EA_b}{A_s}[\varepsilon_t(t)] \tag{4.5}$$

Where, C_b = sound velocity in bar, l=length of the specimen, $\varepsilon_i(t)$ = incident strain, $\varepsilon_r(t)$ = reflected strain signal, $\varepsilon_t(t)$ = transmitted strain signal, A_b = cross sectional are of the bar, As = cross-sectional area of the specimen and E= modulus of elasticity of the bar.

Table 4.2 Post-processing parameters used in this study

Parameter	**Value**
Correlation Criteria	Zero-normalized squared differences (ZNSD)
Pre-filtering	Gaussian
Step Size	1
Subset Size	11× 11 pixels, (110× 110 μm)
Filter size	9 pixels
Virtual strain gage length	9 pixels (90 μm)

In order to capture the images of the deformation of the specimen *in-situ*, a Photron SA-X2 high speed camera equipped with a high-magnification long distance Navitar extension tube was used. A framing rate of 100,000 frames/second was selected in this study at an

image resolution of 384×264 pixel^2. Using the optical setup developed, a pixel to length ratio of 10 µm/pixel was achieved. The field of view of the experiment was 3.84×2.64 mm^2. The images acquired during the experiment were post-processed in a commercially available software Vic2D from correlated solutions. The post processing of the images was performed using the parameters shown in Table 4.2.

4.5 DISTORTION CORRECTION AND MEASUREMENT PERFORMANCE

High magnification digital image correlation is always affected by image distortion due to the spherical geometry of the lenses. This type of image distortion can cause large errors in the displacement calculation. The error associated with displacement is magnified in the strain measurement due to the numerical calculation of the displacement derivatives in strain computation. Therefore, the distortion correction is inevitable in a reliable DIC strain measurement system. To correct the spatial distortion, a well-documented practice was followed in this study. The detailed mathematical background of the method and the complete procedure is not described here, interested readers can refer to [35]. In short, the procedure is described as follows: The speckled specimen was translated in a micrometer assisted linear translation stage to a known distance along the x-direction and imaged. In this study, this horizontal translation was performed in 10 steps with each step-width of 44.5 µm. Similarly, the same procedure was followed in the y-direction with each step-width of 27.5 µm. Images captured during these steps were correlated in Vic 2D software. The uncorrected displacement field obtained is shown in Figure 4.3a and Figure 4.3b. For the 445 µm horizontal translation, a spatial variation of the displacement field across the width was seen with minimum displacement at the center (444.7 µm) and maximum at the edge (449.6 µm). A difference close to 4.9 µm is observed in the contour plot. Figure 4.3c

shows the variation of horizontal displacement (u-displacement) along with a horizontal line AB in the field. In order to correct the distortion, a B-spline vector function (warping function) was generated using the uncorrected correlated images and the known displacement that was noted from the linear stage. This warping function was used to correct the displacement field. The corrected horizontal and vertical displacements are shown in Figure 4.3a and Figure 4.3b. The variation of the displacement from the actual value of 445 µm was close to 0.6 µm after the correction. Displacement along the line AB concaving upward becomes linear as shown in Figure 4.3c.

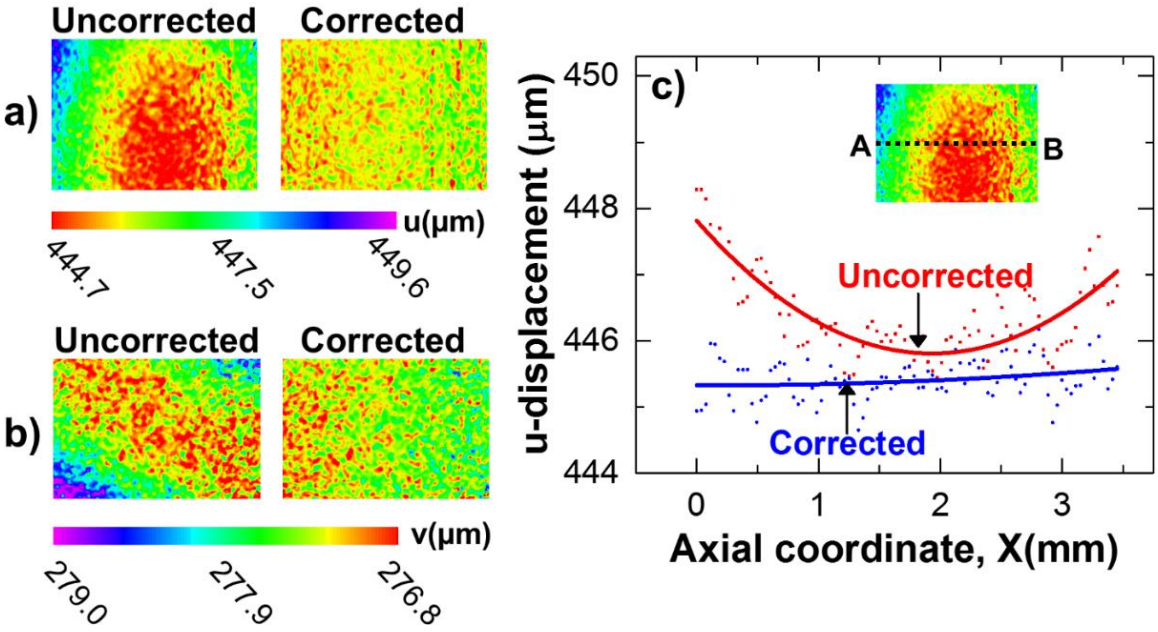

Figure 4.3 (a) Uncorrected and corrected horizontal displacement, (b) Uncorrected and corrected vertical displacement, (c) Uncorrected and corrected horizontal displacement along a line AB.

In order to estimate the strain noise associated with the post-processing of the images at high magnification, we capture 10 undeformed images and post-processed them with the post-processing parameters mentioned in Table 4.2. The mean and standard deviation of the axial, transverse, and shear strain are shown in Figure 4.4 . The mean strain in the full-field measurement remains as low as 0.0063 % (63 µε) for all the 10 images and

the standard deviation of the axial, transverse and shear strain was close to 0.2 %, 0.19 %, and 0.14 % respectively. Therefore, the noise associated with the measurement induces an uncertainty of 4 % when measuring 5 % strain using the experimental setup used in this study. This can be neglected owing to a high strain expected in the dynamic experiment.

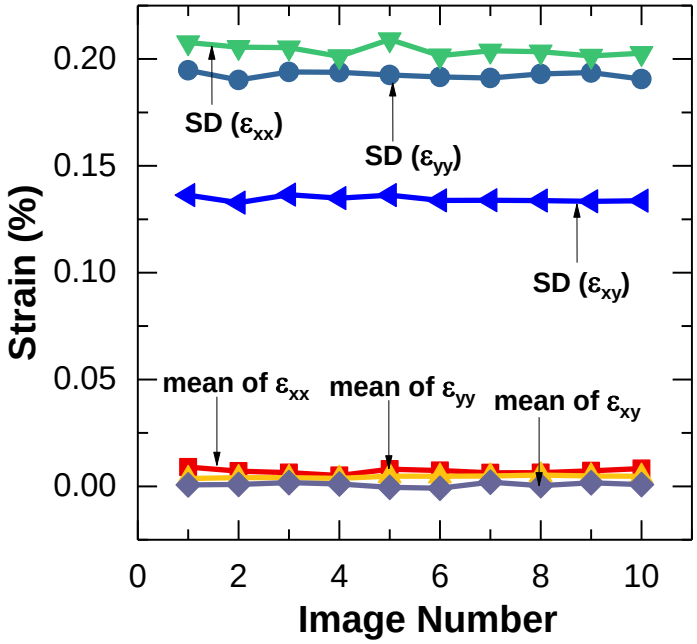

Figure 4.4 Noise in the measurement. Mean and standard deviation of the component strains in an undeformed specimen is shown.

4.6 RESULTS AND DISCUSSION

4.6.1 Macroscale deformation behavior

The strain time signal of the incident, reflected, and transmitted waves are shown in Figure 4.5a. The incident signal has a pulse width of about 1.1 ms which corresponds to the wave transit time in the striker bar. In order to assess the force equilibrium in the specimen during loading, measurement of forces at the left (incident force, Fi) and right end (transmitter force, Ft) of the specimen is required. The forces are calculated from the strain signals using Eq. 4.3. The force time data at the left and right end of the specimen is shown in Figure 4.5b. It demonstrates that the force at the left end-Fi and force at the right

end-Ft are nearly equal, which indicates the attainment of the force equilibrium in the specimen. The stress-strain plot calculated from the strain gage signals is shown in Figure 4.5c. At first, linear elastic deformation behavior is exhibited with a yield stress of 7.5 MPa. It is apparent that the PBS sample shows little or no strain hardening after yielding. The long plateau region after yielding is due to the presence of the soft HTPB binder and incubation of the grain scale failure mechanisms. The failure strain of the sample was around 6.5%, which is consistent with the previous studies in the similar material [13].

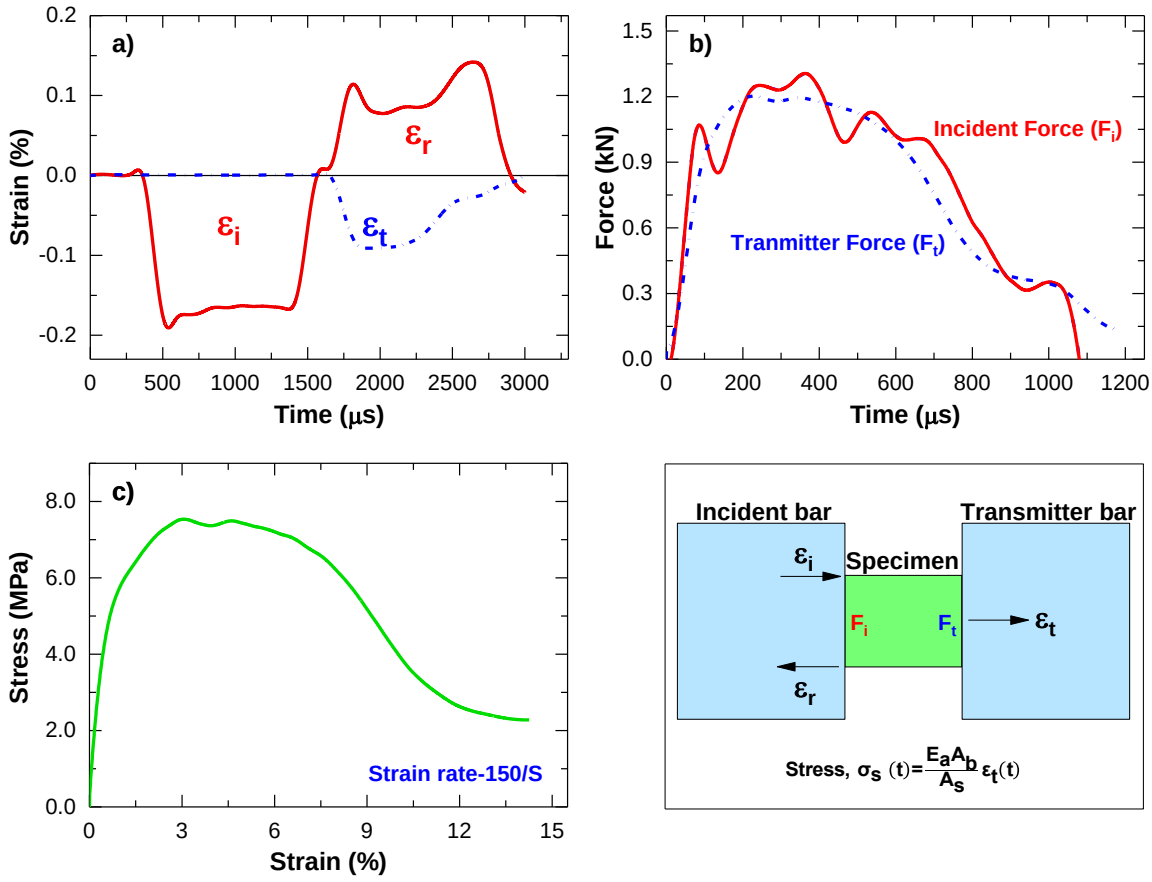

Figure 4.5 (a) The incident, reflected and transmitted strain signal, (b) force with time at incident and transmitter side of the bars, (c) Stress-strain curve obtained from the strain signal.

Macroscopically, the failure of the specimen is occurred due to the shear band formation, as clearly visible in Figure 4.6a. The shear-band is formed at an angle 34 ^{o} with respect to the loading direction. In order to see the grain scale mechanism of material failure, high magnification scanning electron microscope images of the failure surface are obtained, see Figure 4.6. A brittle crystal fracture, failure of the interfaces of the crystal and polymer, and sugar crystal pull-out from the polymer matrix are observed. It should be noted here that a large number of pockets at the failure surface indicates the crystal pull-outs as a result of de-bonding of the weak polymer-crystal interfaces. Small crushed crystals are present at the failure surface owing to crystal fracture at the shearing surface. A crystal with a transgranular fracture is shown in Figure 4.6c and a crystal with an edge fracture are shown in Figure 4.6d.

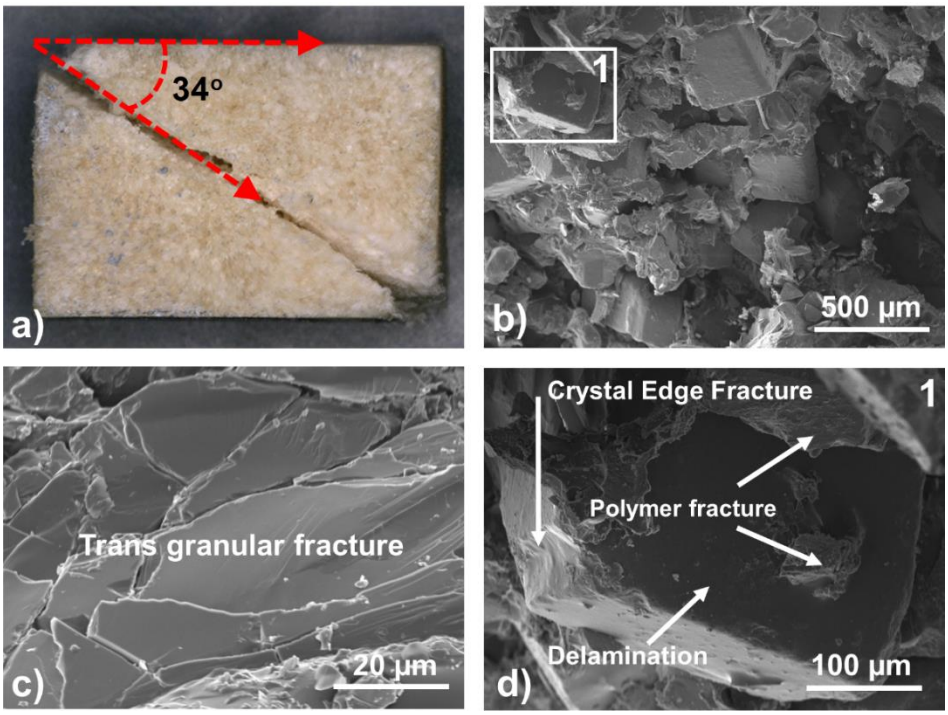

Figure 4.6 (a) Shear band formation, (b) Failure surface with crystal highlighted as region 1, (c) Trans-granular crystal fracture, (d) the magnified view of the region 1 shows crystal edge fracture, polymer fracture, and delamination.

The polymer failure in the form of adhesive and cohesive modes are seen in Figure 4.6d. The residue of the polymer binder on the surface of the crystal is due to the cohesive type failure. Whereas, the clear surface of the crystal shows adhesive type failure of the interface. In the upcoming sections, we discuss the evolution of the meso-scale deformation mechanisms that lead to such failure modes in the material.

4.7 MESOSCALE DEFORMATION BEHAVIOR

In this section, we present the results from the meso-scale experiments. Note that post-processing using Vic 2D is successfully performed for the first 300 μs after loading. In order to relate the microstructure with the strain localization, the microstructure of the AOI is superimposed with the local strain fields. Since the microstructural image of the AOI is obtained before the loading, overlaying of the microstructural image on contour plots of local strain is performed in undeformed reference coordinates. This ensures the concurrence of the contour plots of the full-field local strain with the underlying microstructure.

4.7.1 Local deformation along the loading direction (axial)

The contour plots of the evolution of the local axial strain (ε_{xx}, along the loading direction) during loading is shown in Figure 4.7a. It shows a heterogeneous strain pattern with highly localized strain regions. Interestingly, some regions undergo tensile deformation in the X-direction even at a large global compressive strain of 3.32 %. High strain localization begins to appear in the material well below the yield strength. For example, the local axial strain reaches as high as 10 % for a small global axial strain of 0.58%. It indicates the possibility of incubation of damage in PBS for a small applied load.

The overlay image of axial strain field with the microstructure is shown is Figure 4.7b and the crystal boundaries and polymer rich regions are distinctly visible. Interestingly, the axial strain localization is pronounced in the polymer binder rich region between crystals. The strain localization started at the interface between crystals 2 and 25 and crystals 11 and 14 and serve as a precursor. These regions appear to be nearly perpendicular to the loading direction. Similar observations have been made by LaBarbera [6] in their computational studies on polymer bonded explosives under dynamic loading conditions. The polymer binder between crystals perpendicular to the loading direction will experience more compressive load than the binder between crystals parallel to the loading direction. The polymer binder between crystals that are parallel to the loading direction will have deformation as high as the deformation of the crystals unless the crystals are fractured. As the load increases, more new sites of strain localization are formed, and at this time, the interfaces with strain localizations are no more perpendicular to the loading direction. For example, the interface between crystals 4 and 5 is inclined at 36 ^{o} with the loading direction.

To quantify the strain heterogeneity, a histogram of the data inside the area of interest is plotted in Figure 4.7d. A bin size of 0.085 is used. The frequency diagram of the normalized axial strain shows a wide bell-shaped curve indicating a highly heterogenous strain field as seen in the contour map. Also, as the global axial strain increases, the frequency diagram tends to shrink, which indicates the heterogeneity in the strain field decreases as the global strain increases. The wide histogram at t=100 μs may be due to a dominant polymer binder deformation during the initial stages of the loading. As the load

increases, the crystals in the material began to engage in the load transferring mechanism which possibly reduces the heterogeneity in the strain field

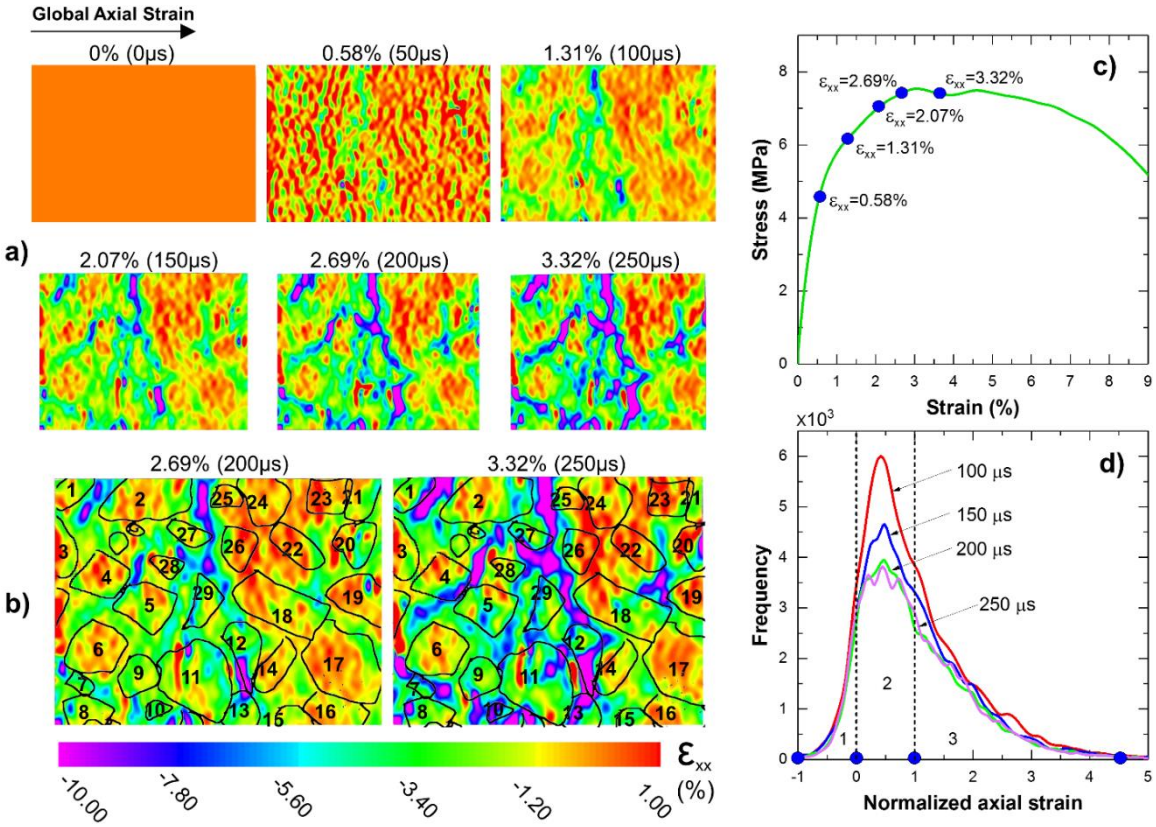

Figure 4.7 (a) Local axial strain evolution with time, (b) Grain boundary overlaid on axial strain field, (c) Global axial strains and its position in stress-strain curve that is presented in the results, (d) Strain histogram at t=100 μs, 150 μs, 200 μs and 250 μs.

4.7.2 Local deformation perpendicular to the loading direction (transverse)

The contour plots of local transverse strain field (ε_{yy}) from the beginning of the loading, t=0 μs, until t=250 μs, is shown in Figure 4.8a. As expected the transverse local strain is heterogeneous, but it is important to note that the strain localization pattern is distinctly different from the axial strain localization. The localized transverse strains are parallel to each other and oriented at ± 36 - 37^{o} with the loading axes, indicating a local shear band as shown in Figure 4.8a. It is also important to note that the magnitude of the

transverse strain is very high, close to the axial strain values, especially in the polymer-rich area. This indicates that the local damage has already occurred causing high local tensile strain along the transverse direction. The more detailed discussion is provided in sections 4.2.4 and 4.2.5.

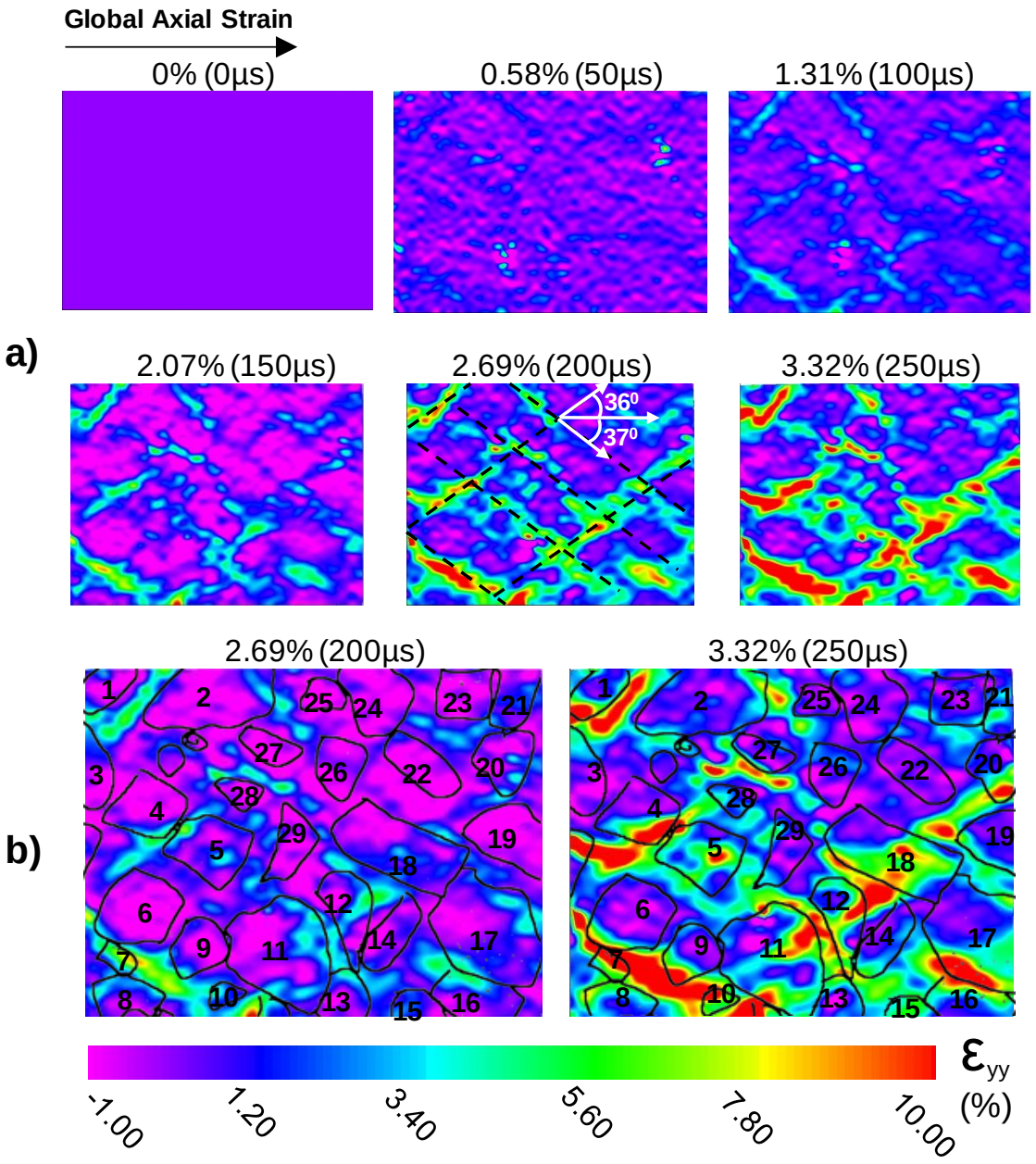

Figure 4.8 (a) Local transverse strain evolution with time, (b) Grain boundary overlaid on transverse strain field.

4.7.3 Local shear deformation

A high shear strain localization is observed at the sub-grain scale as shown in Figure 4.9. Most of the localized shear was observed at polymer rich area and in crystals that experience a fracture. For example, in crystals 12, 18, and 5 very high shear strain, close to -4%, is observed indicating a relative sliding of the crystals after fracture. Also, the high shear strain is observed at the polymer binder rich areas, for example, binder between crystals 4 and 6 and crystals 27 and 28. This large shear strain between crystals could result in the de-bonding type of failure in the material. Therefore, the high local shear strain could lead to two major failure mechanisms occurred in the material, debonding due to matrix failure and crystal fracture.

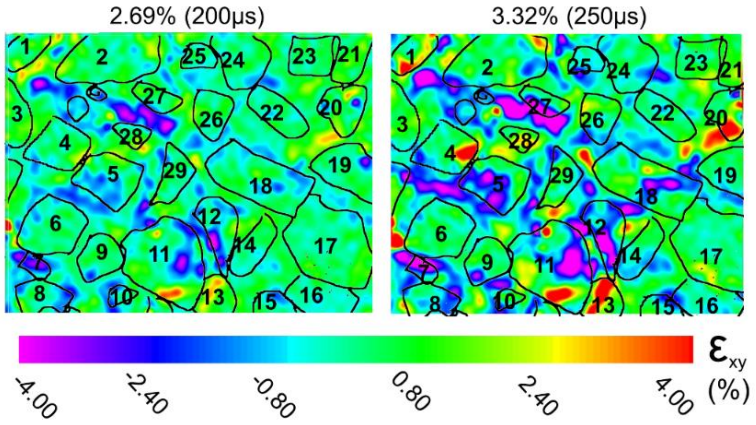

Figure 4.9 Local shear strain evolution with time and grain boundary overlaid on shear strain field

4.7.4 Failure evolution

The failure initiation and its evolution in the material can be characterized by estimating the Poisson's ratio and volumetric strain during loading [1–3] . Poisson's ratio and volumetric strain are calculated from the average strain obtained from the meso-scale experiments. Averaging is performed over 30 crystals and hence it represents the

continuum scale strain, as the representative volume element size of such materials are close to 10 crystals [4,5]. For volume strain calculation, three components of strains are required, though 2D DIC can provide only the in-plane components (ε_{xx} and ε_{yy}). In this study, we assume the lateral strains are equal, $\varepsilon_{yy} = \varepsilon_{zz}$, which is a valid assumption for an isotropic material.

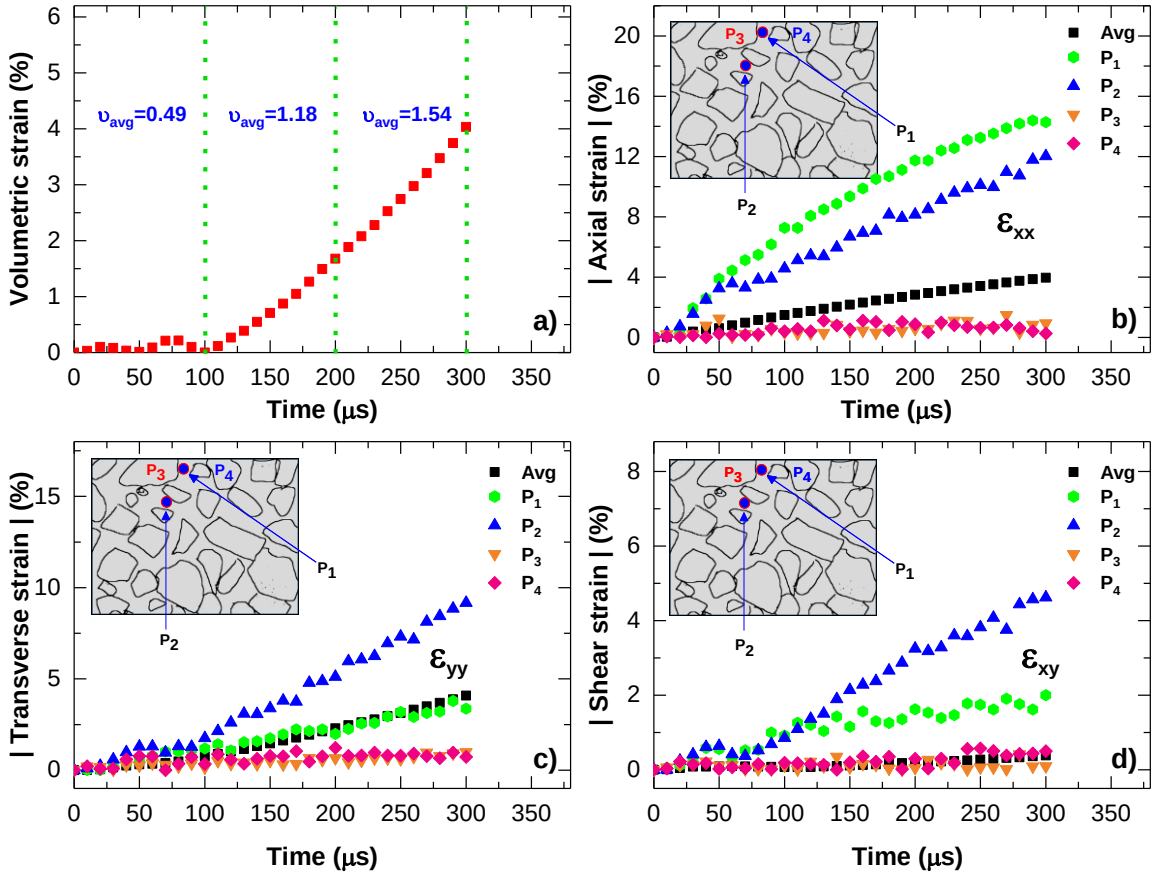

Figure 4.10 (a) Volumetric strain and average Poisson's ratio, (b) Axial strain evolution with time at points P_1, P_2, P_3, and P_4. The location the points are shows in inset figure of microstructure (c) transverse strain evolution with time at points P_1, P_2, P_3, and P_4. The location the points are shows in inset figure of microstructure, (d) shear strain evolution with time at points P_1, P_2, P_3, and P_4. The location the points are shows in inset figure of microstructure.

For the first 100 μs during loading, as shown in Figure 4.10a, the average Poisson's ratio is close to 0.49, a characteristic Poisson's ratio of an incompressible rubbery material

similar to the one used here as a binder. Interestingly, the volumetric strain is close to zero during t ≤100 μs, supporting the incompressibility of the material for the first 100 μs of loading. After that (t>100 μs), the volumetric strain begins to grow non-linearly as shown in Figure 4.10a. An average Poisson's ratio close to 1.18 and 1.54 are observed for 100 μs < t < 200 μs and 200 μs < t < 300 μs, respectively. This is indicative that damage has occurred in the material. The damages as seen above could be a combination of matrix cracking, de-bonding and crystal fracture [2].

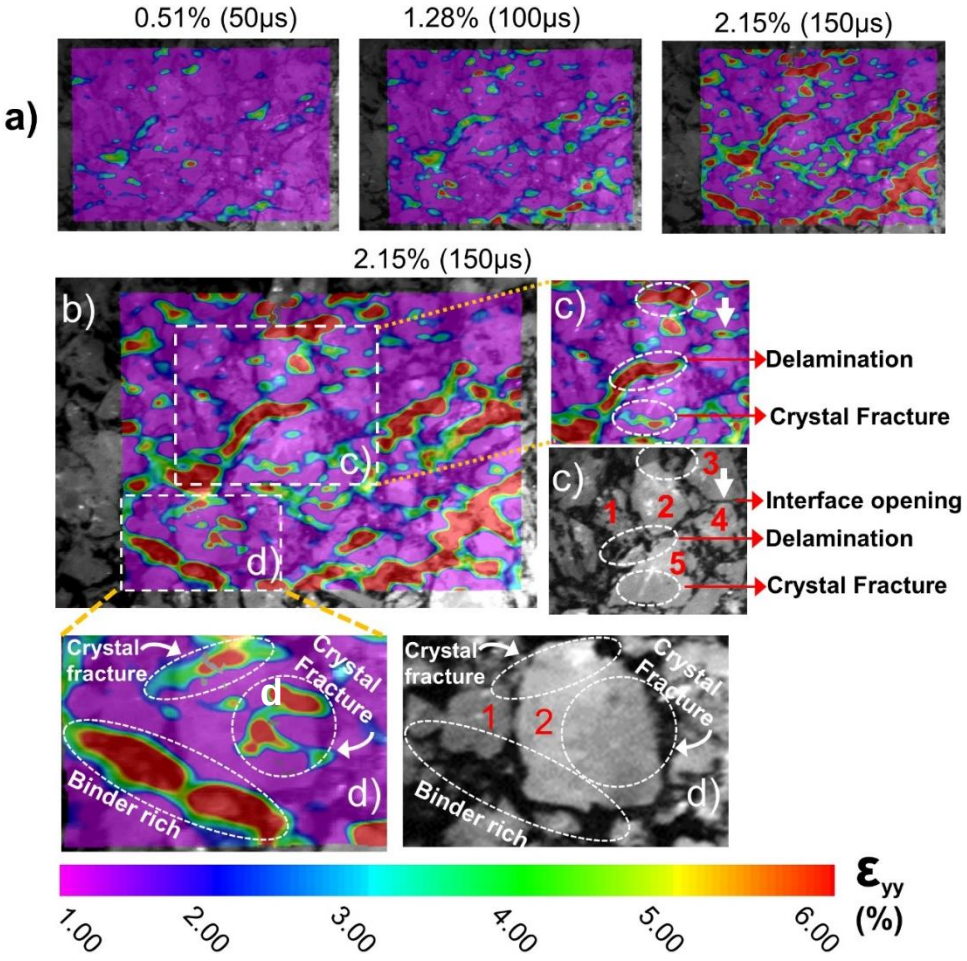

Figure 4.11 (a) Transverse strain evolution (50, 100 and 150 μs), (b) Magnified view of the transverse strain field at t=150 μs, (c) The strain field and the microstructure of the highlighted area shows the crystal fracture and debonding, (d) strain field and microstructure of the highlighted area shows strain localization at the binder rich area and crystal fracture

In order to see the evolution of failure mechanisms, *in situ* experiments have been performed without any speckles on the surface. This experiment shows how the grains and polymer binder rich regions behaves under dynamic loading. By taking advantage of the gray scale intensity variations in the microstructure as speckles and using large subset sizes, the images are processed following the same procedure. The DIC data may have large errors, therefore the post-processed data should be considered as a qualitative representation of the grain-scale deformation. Figure 4.11a, shows the transverse strain field at three different times, t=50μs, 100μs, and 150μs. The contour plots are plotted with 50% transparency in order to roughly see the underlying microstructure. In addition, two areas c and d are marked, and its magnified view of the strain plot and the image of underlying microstructure are shown, see Figure 4.11c and Figure 4.11d. Contour plot has similar characteristics of the transverse strain field obtained in the in section 4.2.2. Importantly, during the initial phase of deformation most of the interfaces have deformed supporting the observation of incompressible deformation of the specimen before the failure initiation. Figure 4.11c shows high transverse strain in crystal-5 an indication of the tensile fracture of the crystal. Multiple high strain regions are observed in crystal-2, see Figure 4.11d indicating Crystal-2 is fractured at multiple locations. It should be noted here that the crystal-2 is significantly larger than that of the crystal-5 in Figure 4.11c which is a suitable condition for the crystal fracture. The binder rich areas marked in Figure 4.11c and Figure 4.11d show high transverse strain, an indication of de-bonding in the material. Therefore, the main deformation mechanisms in this material are the crystal fracture and the de-bonding of the crystals from the polymer binder. It is apparent from the full-field strain field that the plastic strain localization plays a major role in the deformation behavior

of PBX. In addition, most of the strain localization was primarily occur in polymer rich area. This indicates that the major part of the deformation has been accommodated in the polymer binder whereas the crystals are simply reorganizing themselves to accommodate the deformation of the binder. These deformations in the polymer binder can lead to de-bonding of the interface following the failure of the material. The transverse strain field signifies such a damage mode in the material. Also, crystal fracture is apparent which induces high localized transverse strain in the material. In the case of fracture of crystals, cracks are propagated from the crystals to the interface and arrested at the soft binder. Therefore, soft binder act as a shield for crack propagation from crystals in PBX, but it can cause the interface to delaminate from crystal due to stress concentration at the crack tip.

4. Possible mechanism of shear banding and hotspot formation

Shear bands are formed when the mechanical resistance of the material decreases with increasing deformation or strain [6]. Two main mechanisms that are responsible for shear band formation in materials are: 1) mechanical softening due to damage accumulation, 2) thermal softening due plastic strain dissipation as heat. In the present study, we observe the formation of shear band under intermediate strain rate conditions. In metals, shear band formation is due to thermal softening which require a global strain between 10-50%. However, in PBX the strain required to form a shear band is one order magnitude less compared to the shear bands that are formed due to thermal softening. A high strain localization and damage accumulation are apparent even for the small global strain in PBS that is used in this study. These high strain localizations may cause thermal softening, also the microcrack formation. These microcracks causes mechanical softening. Therefore, shear band formation in PBX is due to the combined mechanism of thermal

softening due to high strain localization in the polymer binder and mechanical softening due to damage accumulation in the material.

Computational studies showed that the hot spots are generated as a result of crystal sliding, plastic strain localization, and pore collapse [7–10]. The mechanism of hot spot formation due to pore collapse is not considered; because the low-velocity impact, such as the one in this study, is not capable of generating pore collapse and the following temperature rise. Therefore, during low-velocity impacts, the major hot spot formation mechanism would be a crystal fracture and plastic strain localization. It is seen that the crystal fracture takes place during loading that can cause the frictional heating between the surfaces formed during crack formation. However, it is important to note here that very few crystals are fractured in the material studied. It is greatly possible for higher solid volume fraction material might have more crystal to crystal contacts, therefore, more crystal fracture sites. In addition to crystal fracture, plastic strain localization which is observed in this study can cause viscous heating of the polymer thereby increasing the temperature. However, the time required to transfer heat from the polymer binder to the crystal may be a very important parameter to investigate while considering the plastic deformation of the binder as the hot spot formation mechanism. It is greatly possible that the time required for the heat generated as a result of polymer deformation to reach crystal is higher than the time required for the shear band to form in the material. Therefore, hotspot formation mechanism will be a competition between the mechanism due to crystal fracture and the viscous heating due to plastic strain localization. If the plastic strain localization is the hot spot formation mechanism, then a stiffer binder will help in reducing the number of the hotspot in the material. Whereas a crystal fracture dominated hotspot

formation in PBX can be prevented by embedding explosive crystals in a soft polymer or by increasing polymer binder in the material. To identify which mechanism dominates, it is required to perform temperature mapping during dynamic loading conditions. However, the current experimental diagnostics technique are not capable of measuring the temperature evolution at a smaller length scale at high strain rate. Therefore, experimentally, it is very difficult to distinguish which mechanism dominates in the formation of hotspots in the material.

5. CONCLUSIONS

An experimental method is developed, and strain analysis is performed to study the grain-scale deformation in PBS. The strain evolution and the failure mechanisms are identified by comparing the strain field with the corresponding grain structure. The significance of this experiment is that it enables quantitative analysis of local deformation in the crystals and polymer binder to explain complex local failure modes in PBX.

A highly heterogeneous local strain evolution was observed under dynamic loading. A high transverse strain at the interfaces is observed and could be indicative of de-bonding and crystal fracture. The local failure evolution in the material was quantified by using the Poisson's ratio and volumetric strain evolution. It shows that the mechanical softening due to damage evolution and thermal softening as a result of strain localization causes the shear banding in the material. The possible hot spot mechanism in PBX under intermediate velocity impact loading is primarily the frictional heating due to crystal fracture and the polymer binder deformation.

4.8 LIST OF REFERENCES

[1] Tarver CM, Chidester SK, Nichols AL. Critical conditions for impact-and shock-induced hot spots in solid explosives. J Phys Chem 1996;100:5794–9.

[2] Field JE. Hot spot ignition mechanisms for explosives. Acc Chem Res 1992;25:489–96.

[3] Baer MR. Modeling heterogeneous energetic materials at the mesoscale. Thermochim Acta 2002;384:351–67.

[4] Pierron F, Sutton M a., Tiwari V. Ultra High Speed DIC and Virtual Fields Method Analysis of a Three Point Bending Impact Test on an Aluminium Bar. Exp Mech 2011;51:537–63. doi:10.1007/s11340-010-9402-y.

[5] Drodge DR, Williamson DM. Understanding damage in polymer-bonded explosive composites. J Mater Sci 2016;51:668–79.

[6] LaBarbera DA, Zikry MA. Heterogeneous thermo-mechanical behavior and hot spot formation in RDX–estane energetic aggregates. Int J Solids Struct 2015;62:91–103.

[7] Siviour C., Laity P., Proud W., Field J., Porter D, Church P., et al. High strain rate properties of a polymer-bonded sugar: their dependence on applied and internal constraints. Proc R Soc A Math Phys Eng Sci 2008;464:1229–55. doi:10.1098/rspa.2007.0214.

[8] Barua A, Horie Y, Zhou M. Energy localization in HMX-Estane polymer-bonded explosives during impact loading. J Appl Phys 2012;111:054902. doi:10.1063/1.3688350.

[9] Barua A, Horie Y, Zhou M. Microstructural level response of HMX–Estane

polymer-bonded explosive under effects of transient stress waves. Proc. R. Soc. London A Math. Phys. Eng. Sci., vol. 468, The Royal Society; 2012, p. 3725–44.

[10] Barua A, Kim S, Horie Y, Zhou M. Ignition criterion for heterogeneous energetic materials based on hotspot size-temperature threshold. J Appl Phys 2013;113:64906.

[11] Wu Y-Q, Huang F-L. A microscopic model for predicting hot-spot ignition of granular energetic crystals in response to drop-weight impacts. Mech Mater 2011;43:835–52.

[12] Yan-Qing W, Feng-Lei H. A micromechanical model for predicting combined damage of particles and interface debonding in PBX explosives. Mech Mater 2009;41:27–47.

[13] Dey TN, Johnson JN. Shear band formation in plastic bonded explosive (PBX). AIP Conf. Proc., vol. 429, AIP; 1998, p. 285–8.

[14] Williamson DM, Siviour CR, Proud WG, Palmer SJP, Govier R, Ellis K, et al. Temperature–time response of a polymer bonded explosive in compression (EDC37). J Phys D Appl Phys 2008;41:85404.

[15] Balzer JE, Siviour CR, Walley SM, Proud WG, Field JE. Behaviour of ammonium perchlorate-based propellants and a polymer-bonded explosive under impact loading. Proc R Soc A Math Phys Eng Sci 2004;460:781–806. doi:10.1098/rspa.2003.1188.

[16] Idar DJ, Lucht RA, Straight JW, Scammon RJ, Browning R V, Middleditch J, et al. Low amplitude insult project: PBX 9501 high explosive violent reaction

experiments. Los Alamos National Lab., NM (United States); 1998.

[17] Molinari A, Clifton RJ. Analytical Characterization of Shear Localization in Thermoviscoplastic Materials. J Appl Mech 1987;54:806–12.

[18] Ravindran S, Tessema A, Kidane A. Note: Dynamic meso-scale full field surface deformation measurement of heterogeneous materials. Rev Sci Instrum 2016;87. doi:10.1063/1.4944488.

[19] Ravindran S, Tessema A, Kidane A, Sutton MA. Meso-scale deformation mechanisms of polymer bonded energetic materials under dynamic loading. Conf. Proc. Soc. Exp. Mech. Ser., vol. 7, 2016, p. 451–6. doi:10.1007/978-3-319-21762-8_53.

[20] Ravindran S, Tessema A, Kidane A. Effect of Crystal Density on Dynamic Deformation Behavior of PBX. Challenges Mech. Time Depend. Mater. Vol. 2, Springer; 2017, p. 87–92.

[21] Ravindran S, Tessema A, Kidane A. Local Deformation and Failure Mechanisms of Polymer Bonded Energetic Materials Subjected to High Strain Rate Loading. J Dyn Behav Mater 2016;2:146–56.

[22] Schreier HW, Garcia D, Sutton MA. Advances in light microscope stereo vision. Exp Mech 2004;44:278–88.

[23] Smith PA, Wood JR. Poisson's ratio as a damage parameter in the static tensile loading of simple crossply laminates. Compos Sci Technol 1990;38:85–93.

[24] Lazzeri A, Thio YS, Cohen RE. Volume strain measurements on CaCO3/polypropylene particulate composites: the effect of particle size. J Appl

Polym Sci 2004;91:925–35.

[25] Ravindran S, Koohbor B, Kidane A. Experimental characterization of meso-scale deformation mechanisms and the RVE size in plastically deformed carbon steel. Strain 2017;53.

[26] Hu Z, Luo H, Bardenhagen S, Siviour C, Armstrong R, Lu H. Internal deformation measurement of polymer bonded sugar in compression by digital volume correlation of in-situ tomography. Exp Mech 2015;55.

[27] Liu C. On the minimum size of representative volume element: an experimental investigation. Exp Mech 2005;45:238–43.

[28] Zener C, Hollomon JH. Effect of strain rate upon plastic flow of steel. J Appl Phys 1944;15:22–32. doi:10.1063/1.1707363.

[29] Barua a., Kim S, Horie Y, Zhou M. Ignition criterion for heterogeneous energetic materials based on hotspot size-temperature threshold. J Appl Phys 2013;113. doi:10.1063/1.4792001.

[30] Barua a., Horie Y, Zhou M. Microstructural level response of HMX-Estane polymer-bonded explosive under effects of transient stress waves. Proc R Soc A Math Phys Eng Sci 2012;468:3725–44. doi:10.1098/rspa.2012.0279.

[31] Barua a., Horie Y, Zhou M. Energy localization in HMX-Estane polymer-bonded explosives during impact loading. J Appl Phys 2012;111. doi:10.1063/1.3688350.

[32] LaBarbera D a., Zikry M a. Heterogeneous thermo-mechanical behavior and hot spot formation in RDX–estane energetic aggregates. Int J Solids Struct 2015;62:91–103. doi:10.1016/j.ijsolstr.2015.02.007.

CHAPTER 5

EFFECT OF SOLID VOLUME FRACTION AND STRAIN RATE ON THE MULTISCALE DYNAMIC DEFORMATION BEHAVIOR OF THE POLYMER BONDED EXPLOSIVES

[1]*Ravindran, S.,* Gupta, V., Miller, D & Kidane, A. *In preparation*

5.1 ABSTRACT

Polymer bonded explosives (PBX) are heterogeneous materials that contain solid loading varying from 80-95% and bound together by 5-20% soft binder. An experimental investigation is performed to study the effect of crystal solid loading and strain rate on the failure process of PBX subjected to dynamic loading at different strain rates. Model materials, with sugar crystals and binder, are fabricated with solid loading varying from 80-95%. Then dynamic compression experiments are performed on each specimen using a split Hopkinson pressure bar. During loading, the deformation is captured using the high-speed camera at 0.5 million frames/second. Digital image correlation technique is used to obtain the local and full field deformation and strain fields at each strain rate. Based on the local deformation field and the load data, the failure process of each sample is investigated, and the effect of solid loading and strain rate on the strain localization and failure mode of the PBX is discussed.

5.2 INTRODUCTION

Polymer bonded explosives (PBXs) are viscoelastic particulate composites with high solid volume fraction. The applications of these materials are ranging from solid propellants to explosive charges. Mechanical behavior of PBXs is very complex due to several microscale heterogeneities such as high volume fraction of the solids compared to the matrix, microscale voids and cracks, significant mismatch in the constituent's properties etc [1–5]. These materials undergo loading conditions of varying timescales during transport, machining, storage etc. The sensitivity of PBX is directly related to damage occurs due to such loading of the material. It was seen that the high-temperature local regions called hotspots are formed during impact loading which causes the material

to explode below the threshold shock [6]. This causes significant safety in handling this material. Also, it was observed that the damages in the material during transport, storage, and accidental impacts leads to a high sensitivity of the PBXs. Therefore, the understanding of multiscale material behavior under dynamic loading is critical in predicting the behavior and reliability of the material.

There has been a great deal of numerical and experimental investigation of PBXs are done for the past 40 years in order to predict the behavior of PBXs under different loading conditions [7–9]. Multiscale numerical modeling is well established; however, the number of multiscale experiments is limited due to difficulty in characterizing material at high magnification at faster time scales. Hence, the validation of these models is typically done in one length scale (macroscale), however, the multiscale experiments are essential for accurate numerical modeling. The quantitative investigations of the impact behavior of PBXs very limited due to complexity in high magnification experiments [10]. Recently, an *in-situ* dynamic meso-scale experiments based on digital image correlation (DIC) shows that the main failure mechanisms are de-bonding of the polymer binder and crystal fracture; under intermediate strain rate (150/s) loading [10,11]. This observation was supported by the synchrotron X-ray studies on the model material with few high melting explosive crystals (HMX) in the in hydroxyl-terminated polybutadiene (HTPB) binder. This study proposes that the crystal failure is due to the tensile stress due to force transfer between the crystals through the crystal to crystal contact[12].

It is obvious from the summary of the previous experimental studies that, under intermediate strain rate loading conditions, the mechanisms involved in the failure of PBX are crystal fracture and binder delamination. Therefore, one objective of this study is to

investigate the deformation and failure mechanisms in PBX under different strain rates. In addition, the effect of the solid volume fraction on the deformation behavior and failure mechanisms in the material is investigated. Meso-scale experiments are performed with the help of Hopkinson bar and ultra-high speed-high magnification imaging. Local strain field is measured by using high magnification DIC.

5.3 MATERIALS AND METHODS

5.3.1 Material Preparation and Specimen geometry

A cold pressed polymer bonded sugar (PBS), a mechanical simulant of PBX was used in this study. The sugar simulant contains sugar crystals in place of explosive crystals in the material. This material has been extensively used to characterize the deformation behavior of polymer bonded explosives (PBX) (Ref), because of its similar monoclinic structure of high melting explosives (HMX). In this study, the sugar crystals of size varying from 200-600 μm were used to prepare the sample. The soft binder matrix used is a well-known soft binder, plasticized hydroxyl terminated poly butadiene (HTPB), in the explosive formulation. Binder was prepared by mixing HTPB, di-octyl sebacate (DOS) and toluene diisocyanate (TDI) in the proportion shown in the table. 1. Three PBS samples were prepared by varying the mass fraction of the solid constituent (sugar) in the material. Specimens are named as PBS-80, PBS-87 and PBS-95 depends on the solid mass fraction used in the material. The constituents and mass fraction of each constituent in the material is described in Table.1. A complete preparation steps of the sample is described here. Interested readers can refer to [10].

Table 5.1 Composition of the samples

Specimen	Sugar (%)	HTPB (%)	DOS (%)	TDI (%)
PBS-80	80.0	14.4	3.80	1.8
PBS-87	87.5	9.0	2.41	1.09
PBS-95	95.0	3.6	0.96	0.45

5.3.2 Experimental method

In the present work, three sets of experiments were conducted for a comprehensive understanding. Each of the sets was performed at different strain rates. The first set was macro-scale experiments with speckles on the surface to obtain the full-field macro-scale strain evolution at different rates. The second set was meso-scale experiments that were conducted to obtain the grain scale strain field to understand the local deformation features in the material. The third set of experiments were done without any speckles on the well-polished samples at high magnification to confirm and see the possibilities of additional mechanisms involved in the failure. The last set of experiments help in revealing qualitative grain scale dynamics and features of the crystal failures at different loading rates.

The quasi-static uniaxial compression experiment setup used in this study is shown in Figure 4.2a. The sample was loaded using an Instron machine with a load cell capacity of 5000 N. This small capacity load cell is suitable for the accurate measurement of the load during deformation of the relatively weak specimen used in this study. Displacement controlled loading at the rate of 0.5 mm/min was used in the quasi-static experiments. Dynamic compression experiments were performed on a split Hopkinson pressure bar (SHPB) setup at room temperature. A complete schematic diagram and the photograph of

the experimental setup is shown in Figure 4.2b. The low impedance specimens employed in this study necessitate the use of a low impedance polycarbonate bar to obtain sufficient transmitted signal during loading. Therefore, the incident, transmitter and striker bars used in this study were made of an impact resistant polycarbonate material and were purchased from Macmaster-Carr. Incident and transmitter bars are 1830 mm in length and 25.4 mm in diameter. The duration and amplitude of the incident pulse were controlled by the length of the striker bar and the striker bar velocity, respectively. To measure the strain signals in incident and transmitter bars, strain gages were attached at the middle of the bars. Two strain gages were attached diametrically opposite on the incident and transmitter side to compensate for possible bending of the bar during the wave propagation. These strain gages were connected to a strain amplifier to amplify the strain gage signals which were then recorded using an oscilloscope. The average strain rate, strain, and stress in the specimen were calculated using the following well-known equations,

$$\text{Specimen strain rate, } \dot{e}_s(t) = -\frac{2C_b}{l_0}\varepsilon_R(t) \qquad (5.1)$$

$$\text{Strain in the specimen, } e_s(t) = \int_0^t \dot{e}_s(t)dt \qquad (5.2)$$

$$\text{Stress in the specimen, } \sigma_s(t) = \frac{E_a A_b}{A_s}\epsilon_T(t) \qquad (5.3)$$

Where, 'l_0' is the original length of the specimen, '$\varepsilon_R(t)$' is the time-resolved strain from the reflected pulse in the incident bar. 'C_b' is the velocity of the sound wave in the polymeric bar, and 'E_a' represents the elasticity modulus of the bar material. 'A_b' denotes the cross-sectional area of the bar and 'A_s' is the cross-sectional area of the specimen.

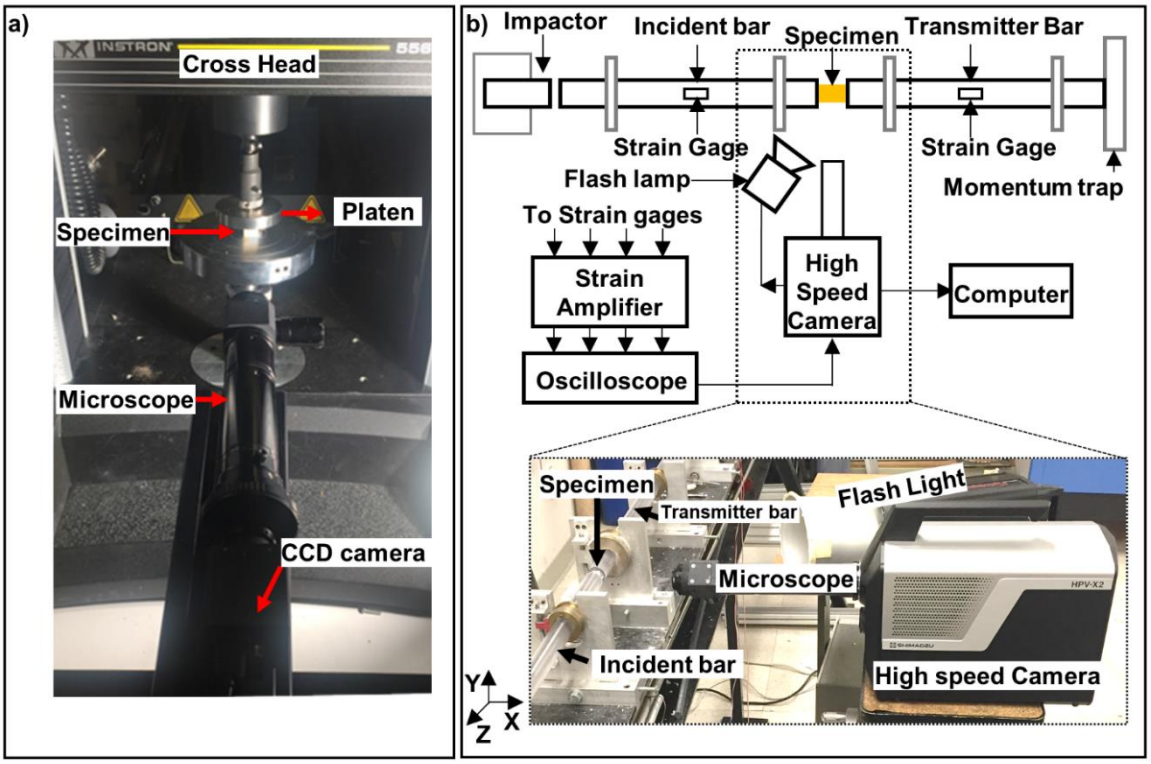

Figure 5.1(a) Complete schematic and the image of the experimental setup, (b) specimen dimension, the area of interest (AOI) and its dimensions, speckles pattern used and the gray scale intensity curve of the speckles used in this study.

To capture the images for macro-scale quasi-static measurement using DIC, a 100 mm Tokina lens was connected to a 5 megapixel (2448×2048 pixel^2) point grey camera. The dimension of the area of interest (AOI) for the macro-scale experiment was 15×20 mm^2 at a spatial resolution of 6 µm/pixel. In the meso-scale experiments, the imaging was performed at high magnification, therefore, a far-field microscope was used in place of Tokina lens, see Figure 5.1a. AOI in the quasi-static meso-scale experiment was 4.22×3.53 mm^2 at a spatial resolution of 1.72 µm/pixel. The illumination for the sample for both the experiments was provided using LED lights. To synchronize the image sequence with the load data, both the images and the load data were captured at the same rates during the experiment.

In dynamic loading, an ultra-high-speed imaging camera HPV-X2 from Shimadzu was used. The full resolution of the camera was 400 × 250 pixel^2 at all framing speeds, with a capability of capturing 128 images. In this study, a framing rate of 0.5 million/second was selected for the macro-scale experiments to capture the complete duration of the dynamic event. Therefore, the total duration of the image capturing sequence was 256 µs. On the other hand, in meso-scale experiments, the framing rate was fixed at 1 million frames/second to capture as many images before the AOI moves away from the focus. In experiments on well-polished samples without speckles, the framing rate was selected as 5 million/second to capture the fast fracture events that could possibly occur in the brittle sugar crystals. The optical setup consisted of the same Tokina lenses used for the macro-scale experiments and far-field microscope for the meso-scale measurement. The magnification optics rendered 4.26×2.65 mm^2 of AOI at a resolution of 10.66 µm/pixel. The illumination of the sample was provided with the help of a Photogenic flash lamp. This lamp has 200 µs rising time to have full intensity, after the rising time, the intensity stays constant for about 3000 µs. Therefore, the lamp was triggered with the help of the oscilloscope by considering the full intensity requirement during deformation.

Cubic samples of 14 mm size with a variability of 0.4 mm were used in this study. Digital image correlation computes the full-field displacement by tracking the points on the surface of the specimen with a random speckle pattern. Therefore, a dense, random, high contrast speckle pattern is required. Before speckling, the sample was dry polished using silicon carbide papers with grit sizes varying from 400-1200, followed by a fine polishing of the sample using smooth polishing cloths. In this study, speckles for the macro-scale study were obtained by an airbrush. A thin coat of white paint was applied to

the sample followed by a black paint using an airbrush. Smaller AOI was used for the meso-scale experiments. Therefore, inscribing an AOI was inevitable to compare the local strain with the microstructure. AOI is marked using the method described in chapter 2.

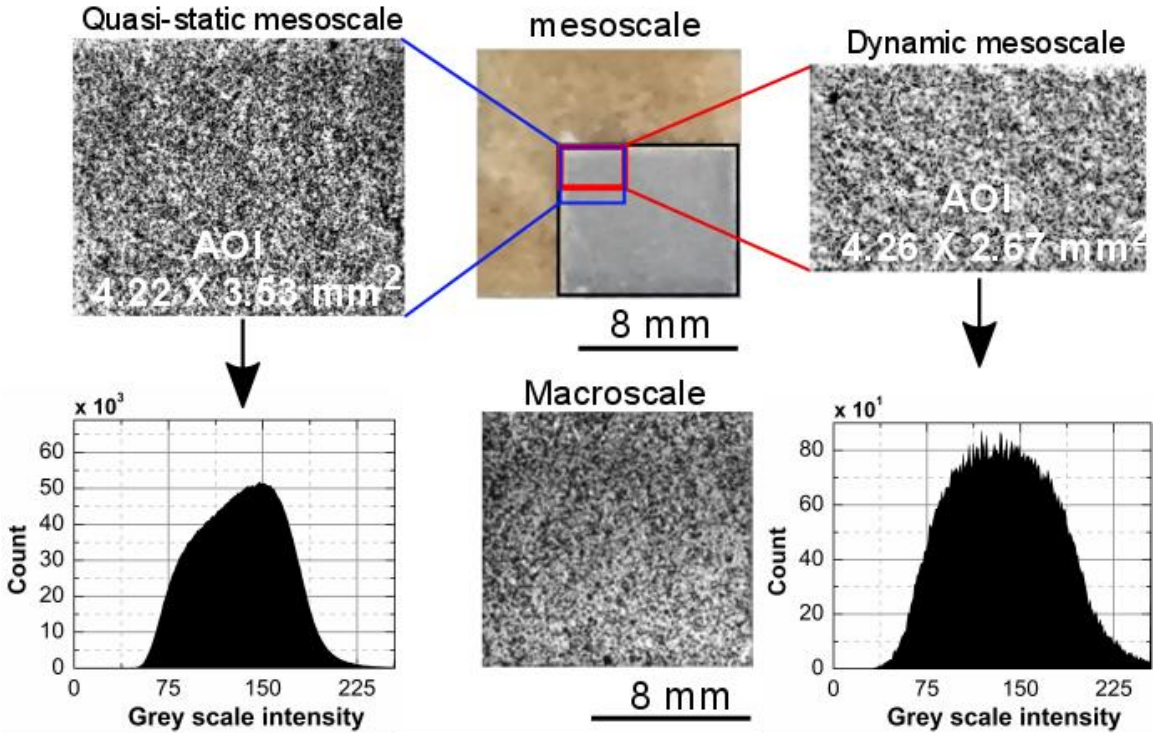

Figure 5.2 Meso-scale speckles and macro-scale speckles used in the experiment. The gray scale intensity values are also shown in the figure.

To relate the underlying microstructure with the local strain field, the microstructural images of the AOI were captured before speckling. Speckling of the specimen was performed as follows. A base coat of white paint was applied on the sample, before the complete drying of the base coat, toner powder was deposited on the surface using an air brush. Same technique was used for meso-scale dynamic and quasi-static measurements. representative macro-scale speckles for both macro and meso scale experiments are also shown in the Figure 5.2. The grey scale intensity pattern for meso-

scale dynamic and quasi-static experiments are also shown in Figure 5.2. It follows a bell-shaped trend which is desirable for the accurate DIC measurements.

The post-processing of the captured images was performed in Vic-2D (Correlated Solutions Inc). For the macro-scale experiment, a subset size of 96 × 96 μm^2 and virtual gage length 96 μm was used. The matching algorithm was selected to be zero normalized squared difference which is insensitive to slight illumination intensity variation coming the flash light. To convert the digital signal into a continuous data, an optimized 8-tap function is employed.

5.4 RESULT AND DISCUSSION

5.4.1 Effect of strain rate

5.4.1.1 Stress-strain curve at different strain rates

A typical strain gauge signal obtained from the oscilloscope for a high rate experiment conducted in this study is shown in Figure 5.3a. Force equilibrium in SHPB experiments is essential to extract a valid stress-strain relation of the material under high rate loading. Therefore, to verify the force equilibrium in the sample, the transmitted strain signal is compared to the sum of the incident and the reflected signal. Figure 5.3a. shows that the sum of incident and reflected, and the transmitted signal are approximately equal. This indicates that the forces on the incident and transmitter side of the sample are in equilibrium. Global stress-strain curve of the material is extracted from the gage signals using the equations shown in section 5.3.2. Three experiments are conducted at each strain rates to check the repeatability and a representative stress-strain curve is used in the discussion.

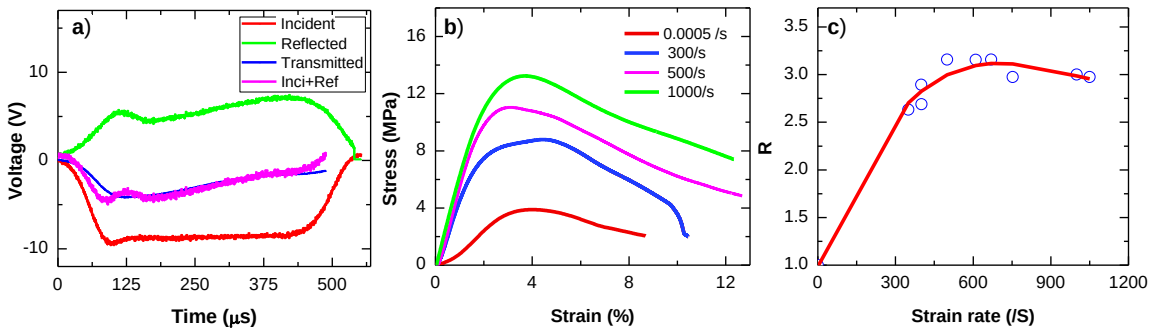

Figure 5.3 (a) Signals recorded from strain gages attached to the incident and transmitter bar, sum of the incident and reflected bar signals show the force equilibrium in the sample, (b) Stress-strain curve at different rates, (c) Strain rate vs. R to obtain the strain rate sensitivity of the material, where $R = \frac{\sigma_{yield-dynamic}}{\sigma_{yield-quasi-static}}$

The representative compressive stress-strain curve at four different strain rates is shown in Figure 5.3b. Clearly, the flow stress increases with increase in strain rate. In quasi-static loading, the flow stress is close to 4 MPa. As the strain rate increases, a stiffer response is observed. The yield stress at a strain rate of 300 s^{-1} is close to 8.5 MPa, whereas at a higher rate (~1000 s^{-1}) the yield stress is close to 13 MPa. In Figure 5.3c, the rate sensitivity of the material is plotted using a parameter R which is the ratio of dynamic yield stress to yield stress at quasi-static loading. The parameter is equal to unity for the quasi-static loading. The parameter shows a drastic increase in yield stress as the strain rate increases and it approximately stays constant after 600 s^{-1} where a flat curve is observed. The strain at failure is also shown in the Figure 5.3c it is also seen increasing and stays nearly constant after 1000 s^{-1}.

5.4.1.2 Macro-scale strain field at different rates

The macro-scale strain components axial (ε_{xx}), lateral (ε_{yy}) and shear (ε_{xy}) in quasi-static and dynamic loading (strain rate 300 s^{-1} and 1000 s^{-1}) conditions are shown in Figure 5.4. The axial strain field shows relatively heterogeneous strain field in all the loading

cases. Interestingly, the shear localization in the dynamic experiments is delayed compared to the quasi-static experiments. In addition, the shear localization in quasistatic experiments is intense and constrained to a small region. Whereas, under dynamic loading, the shear localization is relatively dispersed, and it is appeared to increase with the strain rate. However, the mechanisms that yield to such behavior is unclear at this point, need to see the microscale mechanisms at different strain rates. In order to understand the damage evolution and confirm the type of shear band formed in PBX, the volumetric strain is used.

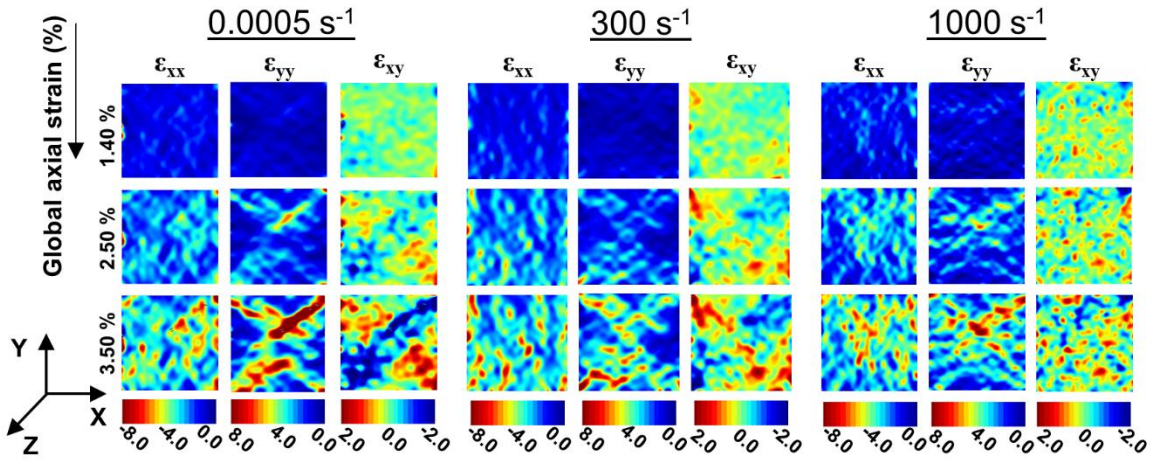

Figure 5.4 Full field axial, lateral and shear strain at different strain rates

5.4.1.3 Volumetric strain as the damage identifier

Volumetric strain can be used to identify the time at which the damage may initiate. The volumetric strain can be calculated using the following equation,

$$\varepsilon_v = \varepsilon_{xx} + \varepsilon_{yy} + \varepsilon_{zz} \qquad (5.4)$$

The experimental measurement was performed on the surface of the sample, and, therefore, only two components (ε_{xx} and ε_{yy}) of the strains are able to obtain from the 2-D DIC measurement. Taking advantage of isotropy, the ε_{zz} can be assumed to be equal to the ε_{yy} which reduces Eq.5.4 to

$$\varepsilon_v = \varepsilon_{xx} + 2\varepsilon_{yy} \qquad (5.5)$$

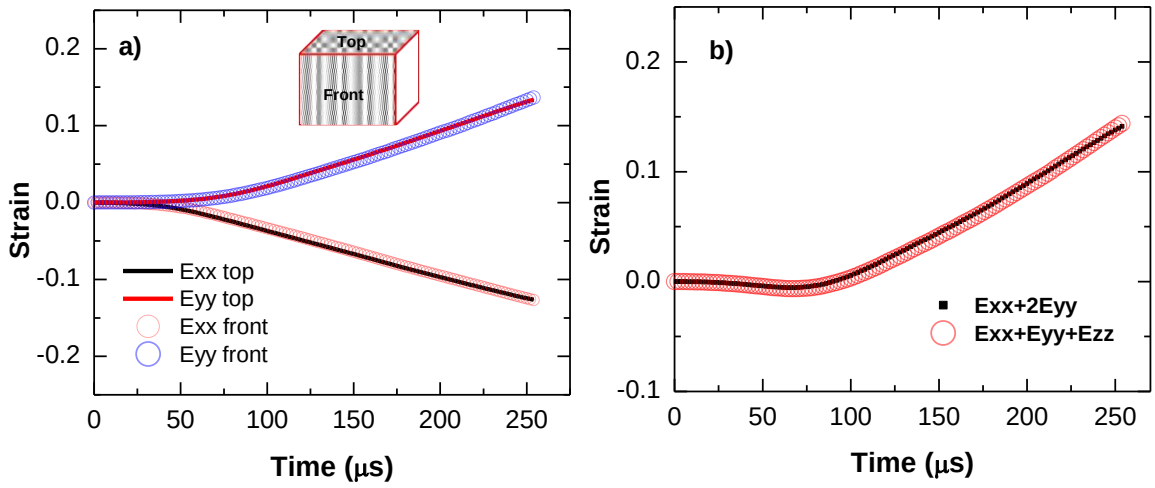

Figure 5.5 (a) Axial lateral strain on the top and front side of the sample, (b) volumetric strain calculated assuming isotropy and without any isotropy assumption.

The assumption is validated by measuring the all the three components of strains by using two cameras that are arranged in 90^o. The measurement was done on the top and front side of the sample. Lateral and axial strains are plotted in the Figure 5.5a. Interestingly, the axial and lateral strains are very close (within 2%) which indicates that the isotropy assumptions hold good for the material used in this study. Figure 5.5b shows the volumetric strain calculated with and without assuming isotropy of the material. The volumetric strain is negative in the initial period of loading, which indicates the closure of gaps in the sample. At t=100 μs, the volumetric strain starts increasing indicating damage initiation in the sample. These high volumetric strains indicate the formation of dilative type shear band where the number of crystal fracture will be less compared to the

compacting type shear band. To understand the mechanisms involved at different strain rates mesoscale experiments are conducted without any speckles on the sample.

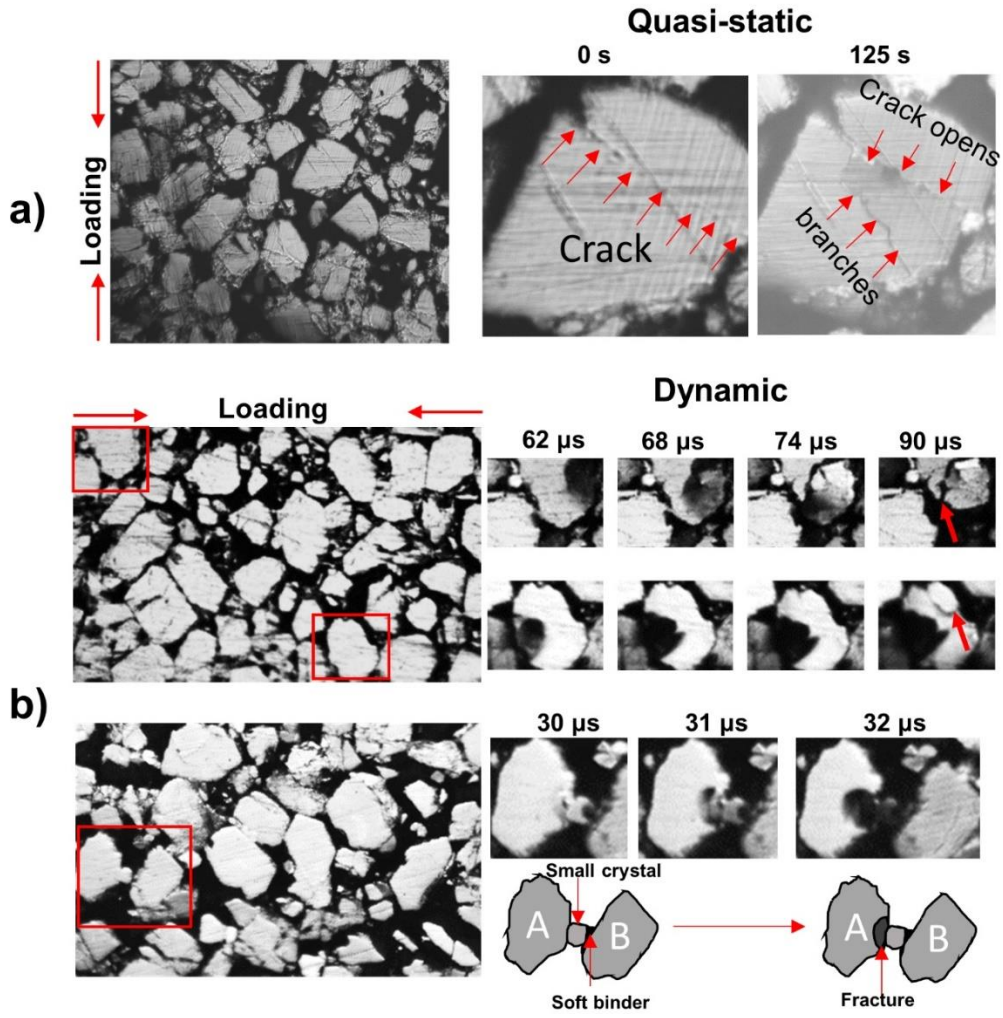

Figure 5.6 Grain scale failure mechanism at (a) quasi-static loading and (b) at a strain rate of 1000 s^{-1}.

Figure 5.6 shows the mesoscale failure mechanism involved in the material under quasi-static loading. In quasi-static loading, it is observed that failure of the material is mainly due to delamination of the binder from the crystal. Also, it is seen that the preexisting cracks open during quasi-static loading. In dynamic experiments, the mechanism involved is significantly different from the mechanism involved in quasi-static loading. It is seen that the crystal-crystal contact location is not undergone fracture during

loading. As the strain rate increases the mechanism of local failure is very different. Delamination of the binder present in the sample, in addition, significant crystal fracture in the crystal-crystal contact locations are identified. For example, severe crystal fracture locations can be seen in the high rate experiment (1000 s^{-1}) Figure 5.6b. The crystals that are separated by binders are not prone to crystal fracture. It should be noticed that not all contact locations undergo crystal fracture which support the observations of force chain formation in the sample.

5.4.2 Effect of Solid loading

5.4.2.1 Macroscale stress-strain behavior

The stress-strain curve for three samples (PBS-80, PBS-87, and PBS-95) at a strain rate of 1,000±50/s is shown in Figure.5.7. After a similar initial linear response, a distinct compression behavior was displayed by all the samples. PBS-95 and PBS-87 exhibit a softening region after yielding, whereas the PBS-80 shows elastic-plastic behavior with a long plastic region. The slope of the post-yielding region is high for PBS-95 compared to PBS-87 indicating lower resistance to the failure compared to PBS-87. The yield strength of PBS-95 and PBS-87 are 16 MPa and 11 MPa, respectively, whereas, PBS-80 exhibit a lower yield strength of 4.5 MPa. A sudden drop in the stress is observed after yielding in PBS-95 and PBS-87. This is due to the macro scale failure initiation in the material. However, PBS-80 shows letter-perfectly plastic response with no evidence of failure up to 25 % of applied axial strain. It is clear that solid mass fraction in the material has a significant effect on the material response. In-depth understanding of the damage mechanisms at meso-scale that yield to such behavior in the material is discussed in the following section.

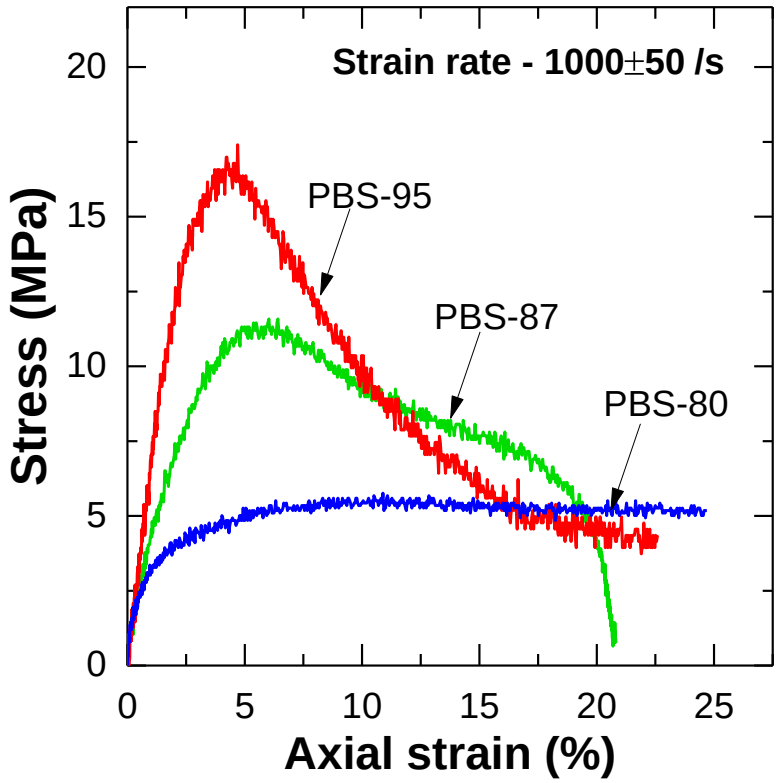

Figure 5.7 Stress strain curve for three different solid loading calculated from the strain gage data, PBS-80, PBS-87, and PBS-95.

5.4.2.2 Meso-scale strain localization

The contour plots of the von Mises strain field for PBS-80, PBS-87, and PBS-95 at three global strains are shown in Figure 5.8a. A highly heterogeneous strain field is apparent for all the material compositions. In addition, the strain heterogeneity increases with increase in applied load. In order to compare the local strain field with the microstructure of the sample, the images of the underlying microstructure are shown in Figure 5.8a. Interestingly, the von Mises strain field in PBS-80 is concentrated in very local regions, whereas the axial strain field in PBS-87 and PBS-95 are more dispersed. This is the direct consequence of the higher solid mass fraction in the material. The higher solid mass fraction increases the number of contacts between the crystals, therefore, the deformation of PBS-95 will be due to the crystal deformation, rather than binder.

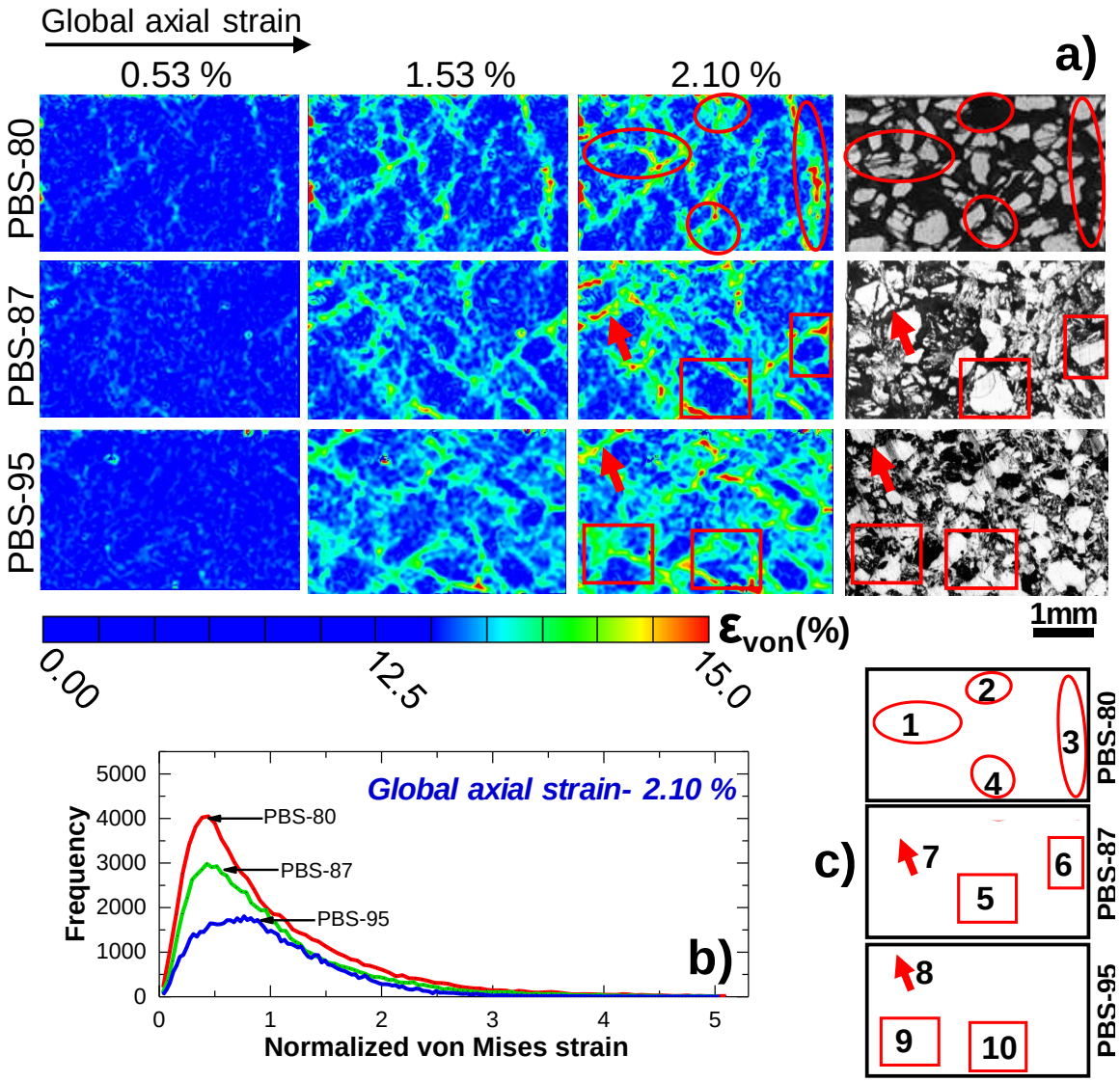

Figure 5.8 (a) Local von Mises strain at different axial global strains for PBS-80, PBS-87 and PBS-95. The underlying microstructure and the crystal and polymer binder locations are marked, (b) histogram of the von Mises strain normalized with the average von Mises strain at a global axial strain of 2.10 % for PBS-80, PBS-87 and PBS-95, (c) numbering of the oval, arrow and rectangular marking used for each local strain field and microstructure to compare the local strain field with the underlying microstructure.

Figure 5.8c shows the histogram of the normalized von Mises strain. It is very clear that for all the samples, the histogram is right skewed, showing the average strain is highly influenced by the high strain values in the area of interest. PBS-80 has a steeper histogram with the peak farthest from the mean indicating the large number of low strain regions. In

PBS-80, as clearly seen in the microstructural image, the number of crystal to crystal contact is limited, therefore, the deformation of the sample is mainly controlled by the polymer binder. As a result, most of the deformation is accommodated in the polymer binder. Whereas, as the solid mass fraction increases, resulting in a greater number of crystal contacts, a more dispersed deformation field with effective force transfer between the crystals are formed. As a result, the peak of the histogram moves closer to the mean as seen in Figure 5.8b. In PBS-95, a sharp peak is not present which is due to the high solid volume fraction causing a higher dispersion in the strain field due to effective load transfer through the contacts of the crystals. The histogram of PBS-87 lies in between PBS-80 and PBS-90 indicating material behavior is affected by the crystal deformation and polymer binder deformation. In order to understand the local deformation mechanism that causes such features, it is required to investigate the local component strain field. It is unclear that the strain induced in the material causes the damage evolution in the material.

5.4.2.3 Damage evolution and local component strain field

Local strain field evolution associated with the global strain from 0% to 2.10% for three different solid loadings is shown in Figure 5.9. It is important to note that in all cases, the axial strain localization occurred at the vertical interfaces of the crystal where the polymer separates one crystal from another. As shown in the figure, the local compressive strain is higher than 5%, for the global strain of 0.53%. It is apparent that the degree of axial strain localization decreases with an increase in solids loading. This could be due to the fact the lowest solid loaded sample has a higher amount of polymer binder (20%) and can absorb most of the deformation locally without deforming the crystals. As the solid loading increases, the amount of polymer in the interface decreases (only 5 % in the case

of PBS-95), resulting in the compressive deformation partially taken by the crystals which lower the localized axial strain.

Similarly, the local transverse strain field at for PBS-80, PBS-85, and PBS-95 are shown in Figure 5.9. Unlike, the axial strain, in this case, the local transverse strain is oriented at 450 with the loading axes, indicating a local shear band formation. Though the degree of localization is different, the shear band formation is observed in all PBS specimen considered. For example, the local transverse strain is highly localized in the case of the highest solid loading (PBS-90) compared with the others. The main reason for the higher strain localization in high solid loading specimen compared to others is not clear at this time. However, it could be due to a fracture caused by local share band formation. The local shear band formation could lead to crystal fracture, and the highest solid loaded PBS is prone to fracture, as a direct crystal to crystal contact is apparent due to a very low polymer content. or a better comparison, the axial strain and transverse strain at 2.12 % global strain and the associated microstructure of the PBS are shown in Figure 5.9. Different locations are marked by a square box for a better visualization of the results. As shown, first the local axial strain is somehow aligned perpendicular, whereas the transverse strain is inclined at 45^{o} with respect to the loading direction, in all of the cases. There is also an indication, in the case of PBS-80 and PBS-87, the axial strain and the transverse strain are highly localized at the interface, whereas, in the case of PBS-95, the transverse strain is localized outside the interfaces. As shown in Figure. 5.9, the crystal to crystal contact is higher in the case of the PBS-95 compared to PBS-80 and PBS-87, and highly

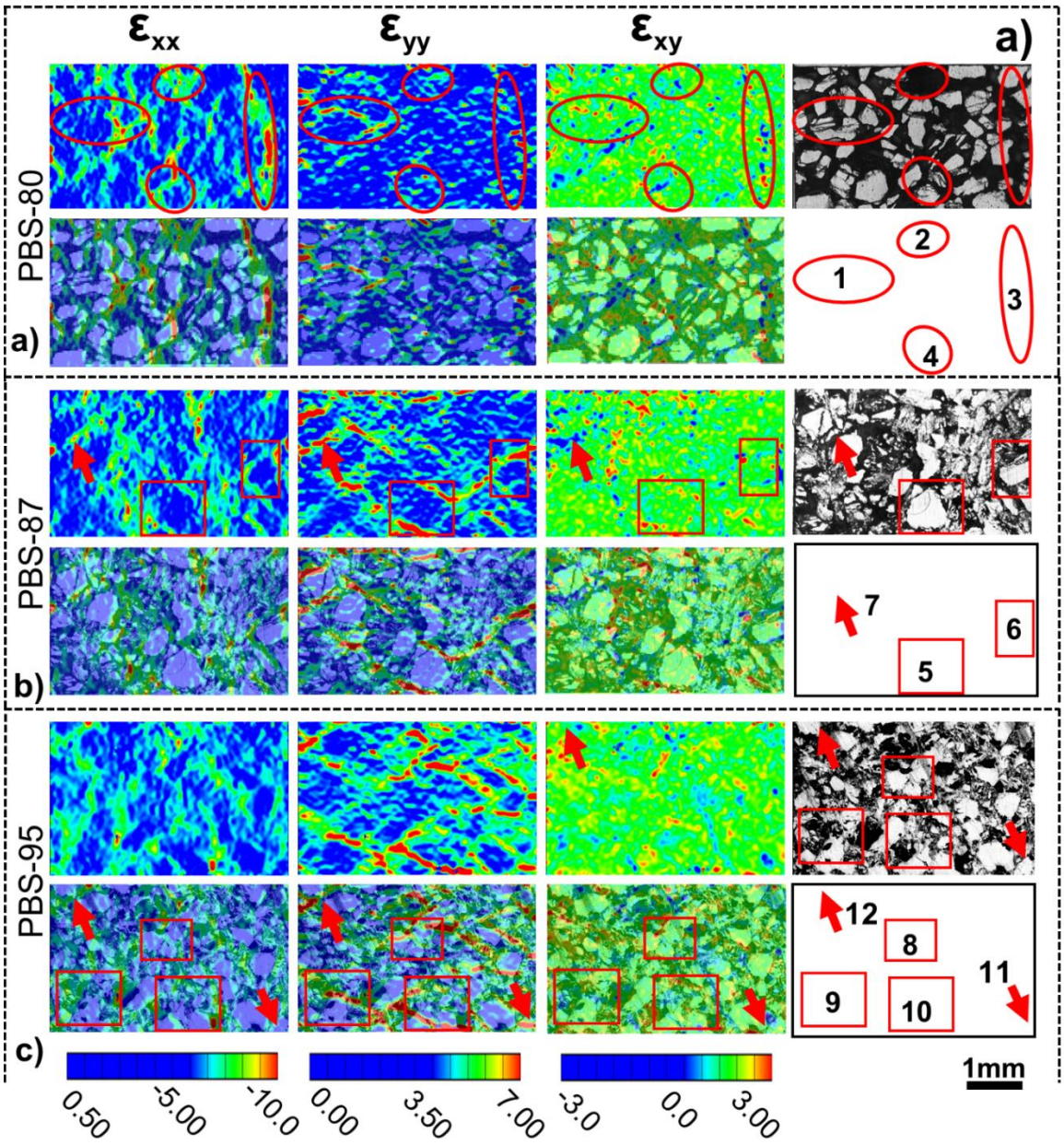

Figure 5.9 Local axial, transverse and shear strain at an axial global strain of 2.10 % (a) PBS-80, (b) PBS-87 and (c) PBS-95. The underlying microstructure and the crystal and polymer binder locations are marked

likely the crystals engaged in the load bearing process. The stiffness of the stress-strain curve shown in Figure 5.7 is additional evidence of this observation. Therefore, the brittle type failure observed in the case of PBS-95 is due to the fracture of crystals due to high-stress concentration at the contact points. On the other hand, the local shear band formed

in the lower solid loaded samples could have been constrained in polymer deformation and delamination of crystals could be the main failure mechanism. The large softening region in the case of PBS-80 and PBS-87 observed in Figure 5.7, supported this observation. It is clear that the deformation mechanisms are possible de-bonding of the interface and the crystal fracture. However, it is not clear whether these high tensile strains cause any incubation of the damage at the interface, which needs to be investigated. The damage initiation and its propagation are discussed with the aid of Poisson's ratio and volumetric strain in the following section.

5.4.3 Damage evolution and possible force chain formation

Damage progression and load carrying mechanisms in composite materials can be studied using the evolution of the Poisson's ratio and volumetric strain with the applied axial strain. Poisson's ratio of the polymer binder and sugars are 0.5 and 0.25, respectively. A Poisson's ratio close to 0.5 while loading indicates the possibility of dominating polymer binder deformation, whereas Poisson's ratio close to 0.25 may indicate a dominant crystal deformation in the material. The Poisson's ratio is obtained by calculating the absolute value of the ratio of the transverse and axial strain. In the case of debonding, micro-voids are formed which essentially increases the volume of the sample, therefore the increase in volumetric strain can be related to the damage initiation in the material. To calculate the volumetric strain, three components of the strains are required. However, DIC calculation on the surface of the sample can only measure the in-plane components ε_{xx} and ε_{yy}. To obtain the third component ε_{zz}, it can be assumed that $\varepsilon_{yy=}\ \varepsilon_{zz}$ without any significant error by assuming of isotropy of the material. Hence, the volumetric strain is calculated using the following equation.

$$\varepsilon_{vol}=\left(\varepsilon_{xx}+2\varepsilon_{yy}\right) \quad (5.4)$$

Evolution of the Poisson's ratio with the applied axial strain is shown in Figure 5.10a. PBS-80 shows a Poisson's ratio close to 0.47 upto ε_{xx}=3.8 % indicating nearly incompressible deformation. Therefore, during the initial period of deformation, the material deformation is confined to the polymer binder locations. This is what we observe in the local axial strain plot of PBS-80 in Figure 5.9a. At the same time, the volumetric strain is negative, and it crosses over to a positive value only after ε_{xx}= 3.8 %. The negative volumetric strain is due to reduction in volume during compression without any damage initiation. Note, the macroscale stress-strain curve shows in Figure.5.7 that the yielding of PBS-80 starts at an axial strain close to 3.5-4%.

In the case of PBS-87, upto ε_{xx}=1 %, the Poisson's ratio is close to 0.47. After that, the Poisson's ratio drastically increases as shown in Figure.5.10a. Therefore, it can be seen that the incubation of the damage in PBS-87 starts before the yielding of the sample. A similar observation can also be seen in PBS-95, but with a faster increase in Poisson's ratio as the axial strain increases. The volumetric strain is positive indicating the dilation of the sample under compression as a result of volume increase, and this is directly related to the damage initiation in the material. Comparing the damage initiation in PBS-80, PBS-87 and PBS-95, the lower solid fraction PBS sample shows higher resistance in developing damage due to high soft polymer content. Whereas, PBS-87 and PBS-95 show a lower resistance to the incubation of the damage. This is because the low amount of polymer causes the crystals to deform and become more prone to de-bonding and crystal fracture. In order to this. an overlay plot of transverse strain on the microstructure is presented. This image is created by making the contour plot transparent for all strains below 3 %.

Therefore, the transparent part has strain less than 3%. It essentially shows how many locations in PBS-80, PBS-87 and PBS-95 have high tensile strain. It is clear as discussed in the previous section the number of high tensile strain locations is higher in PBS-95 compared to PBS-87 and PBS-80. PBS-80 has very few locations with high tensile strain. In PBS-95 crystal fracture locations are visible, whereas in PBS-80 and PBS-87, the crystal fracture locations are greatly reduced or not present. Therefore, the failure mechanism in PBS-80 is mainly de-bonding, whereas, PBS-87 and PBS-95 have a combined mechanism of crystal fracture and polymer binder de-bonding.

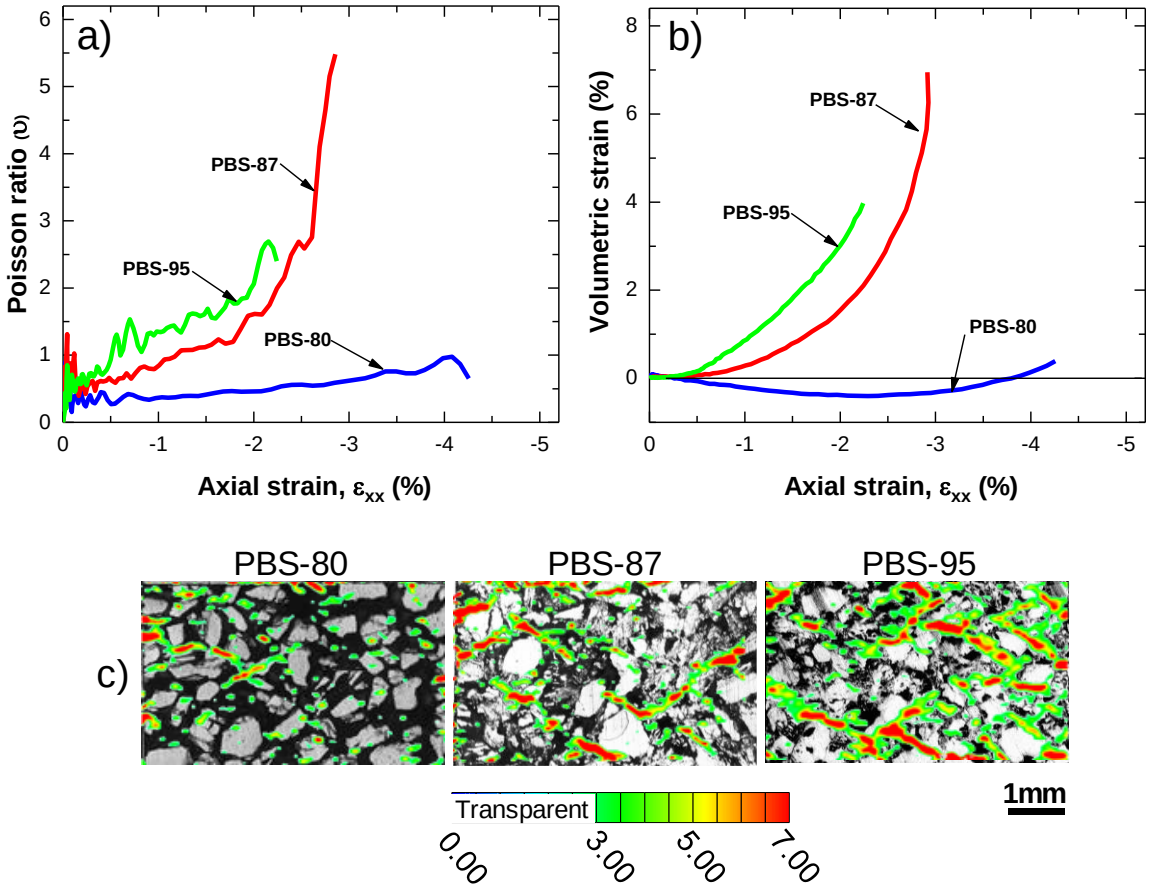

Figure 5.10 (a) Variation of Poisson's ratio of PBS-80, PBS- 87 and PBS-95 with axial strain, (b) volumetric strain developed in PBS-80, PBS- 87 and PBS-95 with axial compressive strain.

The fracture stress of the sugar crystals is close to 200 MPa. However, in this experiment, there is a clear evidence of the crystal fracture in PBS-95 despite a low failure stress of 16 MPa. It is well-known that force chains play an important role in the strain localization and damage behavior of granular composites. Polymer bonded explosives can be considered as a cohesive granular media. It is shown that the cohesive granular assemblies can have the force chains similar to granular material. Rajdai et al showed that the force distribution in a cohesive granular media has an exponential tail [13]. In order to see the possible formation of force chains in the material, the probability distribution of the normalized minimum principal strain is used. It is showed that the force chains under compression is in the direction of the minimum principal strains [14]. Assuming the direction of minimum principal stress is in the direction of the minimum principal strain, the force chain characteristics can be studied in the material by using generic form of the probability distribution of the force chain,

$$P\left(\frac{\varepsilon_p}{<\varepsilon_p>}\right)=\begin{cases} A\left(\frac{\varepsilon_p}{<\varepsilon_p>}\right)^{-\alpha}, & \frac{\varepsilon_p}{<\varepsilon_p>}<1 \\ Ae^{-\beta\left(\frac{\varepsilon_p}{<\varepsilon_p>}\right)}, & \frac{\varepsilon_p}{<\varepsilon_p>}>1 \end{cases} \qquad (5.5)$$

where, $P\left(\frac{\varepsilon_p}{<\varepsilon_p>}\right)$ is the probability of the normalized minimum principal strain, $\frac{\varepsilon_p}{<\varepsilon_p>}$ is the minimum principal strain normalized with the spatial average of the minimum principal strain. Note, that only compressive strains are considered while calculating the probability due to very low tensile strain locations. The force chain has a characteristic β value, it typically lies between 0.9-1.5. The probability distribution function at axial strain of 1.5 % is plotted for three compositions in Figure.5.11. Interestingly, for $\frac{\varepsilon_p}{<\varepsilon_p>}>1$, the β

value is 1.17 and 1.24 for PBS-87 and PBS-95, respectively. Also, for $\frac{\varepsilon_p}{<\varepsilon_p>}<1$, the probability distribution approximately follows a power law distribution, which would be expected the when force chains are present. Therefore, the crystal fracture in these materials can be attributed to strong force chain formation in the material. However, in PBS-80, the data points fit an exponential distribution for the entire probability distribution data points. The β value is close to 0.63 indicating the chances of very localized load transfer and disengagement of the crystals in the load transfer mechanism during the initial phase of loading, which support the macroscale observation of the incompressible Poisson's ratio with the polymer binder dominated mechanism of deformation.

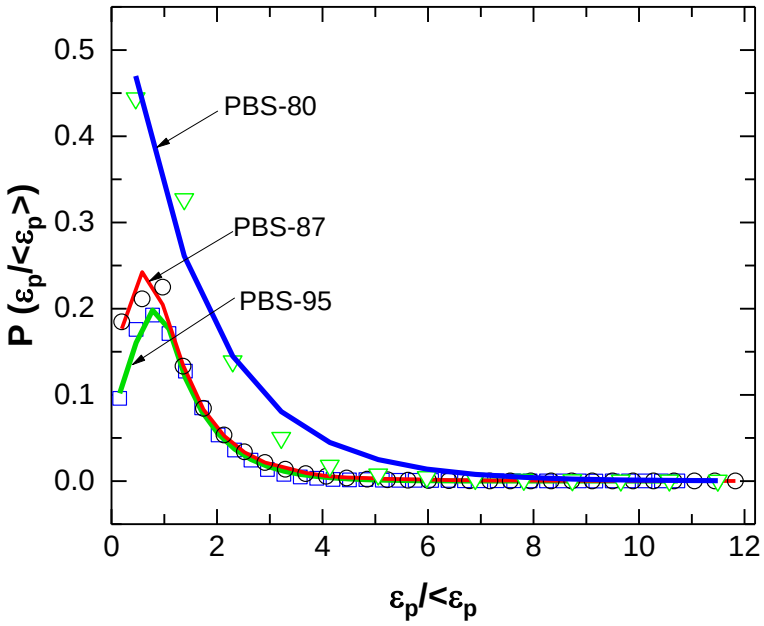

Figure 5.11 Probability distribution of the minimum principal strain

5.5 SUMMARY

The effect of solids loading and strain rate on the local deformation mechanism of energetic materials is investigated using mesoscale digital image correlation at 0.5 million frames per second. The strain rate has a significant effect on the local failure mechanisms.

Macroscopically, it was observed that the shear localization is severe in the quasistatic loading conditions with relatively dispersed shearing at higher strain rates. The reason for such behavior is due to the local crushing of the crystals under higher strain rates. It was observed that the amount of solid loading in PBS can alter the local deformation mechanism. The localized axial strain is higher in the case of low solid loading material than the high solid loading. On the other hand, the transverse strain is highly localized in the case of the highest solid loaded samples. The main failure mechanism in the highest solid loaded sample is crystal fracture whereas the primary failure mechanism in the lowest solid loaded sample is debonding of the crystals.

5.6 LIST OF REFERENCES

[1] Drodge DR, Williamson DM. Understanding damage in polymer-bonded explosive composites. J Mater Sci 2016;51:668–79.

[2] Siviour CR, Grantham SG, Williamson DM, Proud WG, Field JE. Novel measurements of material properties at high rates of strain using speckle metrology. Imaging Sci J 2009;57:326–32.

[3] Barua A, Horie Y, Zhou M. Microstructural level response of HMX–Estane polymer-bonded explosive under effects of transient stress waves. Proc. R. Soc. London A Math. Phys. Eng. Sci., vol. 468, The Royal Society; 2012, p. 3725–44.

[4] Field SGG and CRS and WGP and JE. High-strain rate Brazilian testing of an explosive simulant using speckle metrology. Meas Sci Technol 2004;15:1867.

[5] Balzer JE, Siviour CR, Walley SM, Proud WG, Field JE. Behaviour of ammonium perchlorate-based propellants and a polymer-bonded explosive under impact loading. Proc R Soc A Math Phys Eng Sci 2004;460:781–806. doi:10.1098/rspa.2003.1188.

[6] Tarver CM, Chidester SK. On the violence of high explosive reactions. J Press Vessel Technol 2005;127:39–48.

[7] Barua A, Horie Y, Zhou M. Energy localization in HMX-Estane polymer-bonded explosives during impact loading. J Appl Phys 2012;111:54902.

[8] Barua A, Zhou M. A Lagrangian framework for analyzing microstructural level response of polymer-bonded explosives. Model Simul Mater Sci Eng 2011;19:55001.

[9] Bardenhagen SG, Brackbill JU, Sulsky D. Numerical study of stress distribution in

sheared granular material in two dimensions. Phys Rev E 2000;62:3882.

[10] Ravindran S, Tessema A, Kidane A. Local Deformation and Failure Mechanisms of Polymer Bonded Energetic Materials Subjected to High Strain Rate Loading. J Dyn Behav Mater 2016;2:146–56.

[11] Ravindran S, Tessema A, Kidane A, Sutton MA. Meso-scale Deformation Mechanisms of Polymer Bonded Energetic Materials Under Dynamic Loading. Mech. Compos. Multi-functional Mater. Vol. 7, Springer; 2016, p. 451–6.

[12] Parab ND, Roberts ZA, Harr MH, Mares JO, Casey AD, Gunduz IE, et al. High speed X-ray phase contrast imaging of energetic composites under dynamic compression. Appl Phys Lett 2016;109:131903.

[13] Radjai F, Topin V, Richefeu V, Voivret C, Delenne J-Y, Azéma E, et al. Force transmission in cohesive granular media. Math Model Phys Instances Granul Flows 2010:240–60.

[14] Tordesillas A, Muthuswamy M, Walsh SD. Mesoscale measures of nonaffine deformation in dense granular assemblies. J Eng Mech 2008;134:1095–113.

CHAPTER 6

WEAK SHOCK WAVE PROPAGATION IN POLYMER BONDED EXPLOSIVES

[1]*Ravindran, S.,* Tessema, A., Kidane & Jordan, J. *To be submitted to Philosophical Transactions of the Royal Society A*

6.1 ABSTRACT

Weak shock waves are common in low velocity impact scenarios of polymer bonded explosives. However, experiments that characterize the weak shock wave structure is limited. In this study, a detailed experimental study is conducted to characterize the weak shock formation in polymer bonded explosives. Specimens made of polymer bonded sugar, a well-known simulant of polymer bonded explosives are used for the experiment. The specimen is subjected to impact loading at three impact velocities varying from 53-94 m/s with the help of a modified Hopkinson pressure bar apparatus. The full-field deformation is captured in-situ using an ultrahigh-speed imaging camera. Full-field displacement and strain are extracted from the recorded images using digital image correlation (DIC). Based on the full-field data, the shock wave velocity, shock front thickness, and full-field stresses are calculated. The energy dissipated during shock wave propagation is also estimated based on the full-field stress-strain data estimated from the full-field displacement calculated using DIC. Further, effect of impact velocity on the spatial stress profile, shock wave velocity and energy dissipation discussed.

6.2 INTRODUCTION

Polymer bonded explosives (PBX) are a class of particulate composites with high solid volume fraction. They typically contains 80-95% explosive crystals such as 1,3,5,7-Tetranitro-1,3,5,7-tetrazocane (HMX), 1,3,5-Trinitro-1,3,5-triazinane (RDX), 2,2-Bis[(nitrooxy) methyl]propane-1,3-diyl dinitrate (PETN) etc and 5-20% of the soft polymer binder. The soft polymer binder is used to reduce the shock sensitivity and to improve castablity and machinability. These materials are highly heterogeneous due to a

substantial mismatch in material properties of the constituents and an unavoidable porosity in the material at multiple length scales.

These materials can be subjected to a wide range of loading conditions from low mechanical insults during handling and transportation to strong impacts during accident. It is seen that the weak insults with impact velocity around 40-150m/s, can cause the material to have a deflagration (low-speed combustion) to detonation (high-speed combustion) transition (DDT) [1–4]. There are several experimental and numerical studies that have been performed to understand the deformation mechanisms which trigger such reaction [1,3,5–16]. It is found that bulk load transfer in heterogeneous composites, such as PBX, takes place through particle to particle contacts which lead to stress/strain localization in the area of the contact surfaces, even for weak impact loading conditions [11,12,17]. In addition, the plastic deformation of the binder, void collapse, debonding of the crystals, and frictional heating of the failure surface of the crystals can cause the dissipation of the energy in localized regions in the material [7,9,11,17]. These local energy dissipation mechanisms produce small regions of high temperature called hotspots.

Numerical studies in PBXs shows the propagation of the compaction type wave at low impact velocities (50-200 m/s) [18]. Though, there are several shock propagation experimental based investigations are available to quantify the shock nature in PBX in different loading regimes [19–21], there is no attempts have been made to measure the spatial stress profile, which is essential in estimating the energy dissipation during the shock wave propagation. Especially in the weak shock regime, the full field information is critical due to expected finite shock thickness. Recently, digital image correlation (DIC) based high strain rate experiments have been developed, which allows for full-field strain

and displacement measurements at high spatial resolution under dynamic loading conditions [6,16,22,23]. It is a promising method to measure the local strain field and velocity profile during the propagation of the compaction wave. Recently, X-ray in conjunction with DIC was used to capture the propagation of compaction front in granular ceramics [24].

In this paper, a full field deformation measurement technique at high rates is presented to provide insight into the weak shock propagation. Using this technique, a detailed study of the weak shock wave properties such as wave velocity, spatial stress profile, energy dissipated and the wave thickness at three impact velocities were estimated from the experiment.

6.3 MATERIALS AND METHODS

6.3.1 Material Preparation and Specimen geometry

Polymer bonded sugar, a mechanical simulant of HMX based PBX is used in this study. Sugar crystals have a similar monoclinic crystal structure [25] and morphological characteristics to HMX and they are a suitable mechanical surrogate to for HMX. Polymer bonded sugar has been extensively used as an inert simulant for PBX under different loading conditions [6,10,13,14,26–28]. The Polymer bonded sugar specimens used in this study were prepared by cold pressing of sieved sugar crystals of bimodal particle size distribution as shon in Figure 6.1 and plasticized hydroxyl terminated polybutadiene (HTPB) mixture. The formulation composed of 87.5/9.0/2.4/1.1 wt % of sugar / Hydroxyl-terminated polybutadiene (HTPB)/ di-octyl sebacate (DOS) / Toluene diisocyanate (TDI), where HTPB is the monomer, DOS is the plasticizer and TDI is a curing agent. The HTPB is mixed with the plasticizer (DOS) and curing agent (TDI), then, the sugar crystals are

added to the mixture. The mixture is stirred to ensure thorough mixing, and then placed in a vacuum oven for 6-7 hours at 80 ^{o}C for partial curing. The partially cured, gluey mixture is pressed at 30 MPa pressure in a cylindrical mold of bore diameter 25 mm to produce cylindrical billets. These billets are then completely cured at 80 ^{o}C for 120 hours and cooled slowly to room temperature. Samples for the experiments are machined from the cylindrical billets using a milling machine. The extracted samples are mechanically dry polished with abrasive grinding paper up to a grit of 1200 to have a flat and smooth surface appropriate of DIC imaging. The density of the pressed PBS samples is 1.34 g/cm^3. The theoretical maximum density of the sample is calculated to be 1.47 g/cm^3 and the porosity present in the pressed sample is about 9 % $\left(\varphi = \left(1 - \frac{\rho_{bulk}}{\rho_{TMD}}\right) 100\%\right)$.

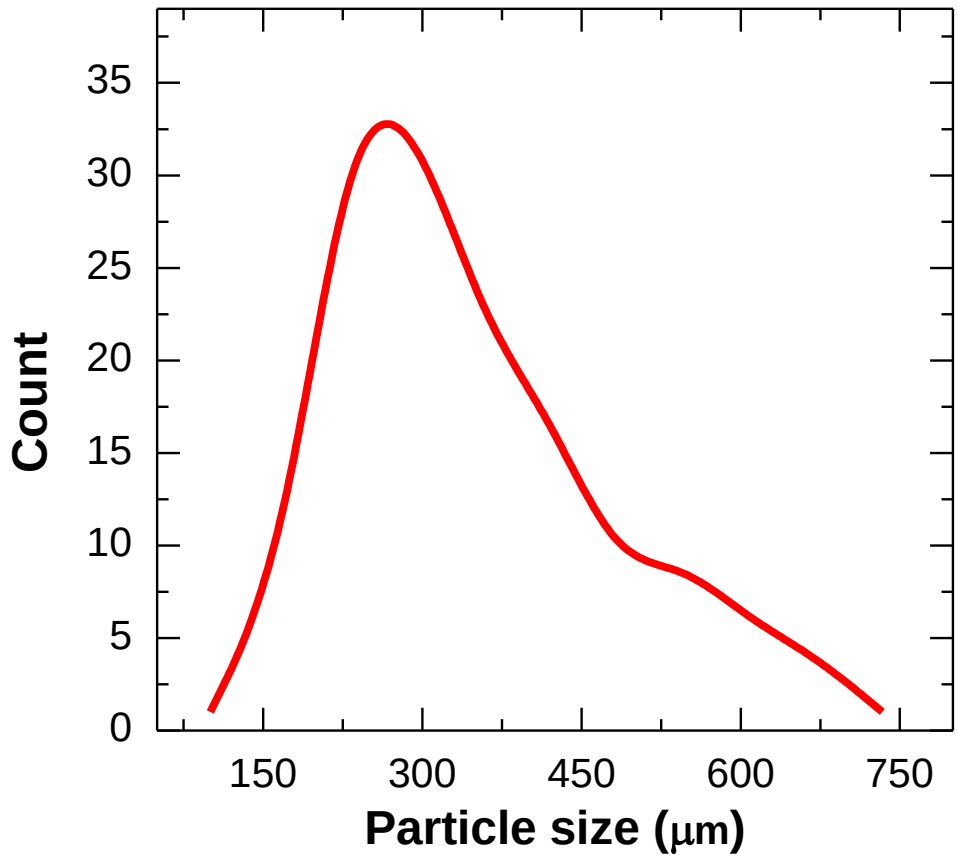

Figure 6.1 Particle size distribution in the specimen

Quasi-static experiments were performed to obtain the elastic properties of the material and to calculate the bulk sound velocity in the pressed samples. The elastic modulus and Poisson's ratio were found to be 59 MPa and 0.46, respectively. Using well-known equations, the bulk sound velocity was calculated to be 428 m/s. Interestingly, the sound velocity in the cast polymer bonded sugar was estimated previously as 420 m/s using pulse echo technique which is close to the velocity estimated in this study [29].

6.4 EXPERIMENTAL SETUP

A complete schematic representation of the experiment setup used in this study is shown in Figure 6.2 The direct impact Hopkinson pressure bar is modified for a projectile impact loading application. It consists of a gas gun, impactor, a fixed transmitter bar, and imaging system. The gas gun is composed of two main parts: a pressure chamber and a launching tube. The gas gun uses inert helium for launching the projectile. In this setup, a transmitter bar is mounted on linear bearings aligned precisely with the launching tube to have a plane impact on the specimen. It should be noted that the transmitter bar is 150 mm long and fixed at one end. One side of the specimen is attached to the transmitter bar with the help of a thin layer of lithium grease. The other side of the specimen is free and close to the barrel of the launcher facing the impactor. In contrast to typical split Hopkinson pressures bars, there is no incident bar in this setup; instead, an impactor directly contacts the specimen upon exiting the launching tube that is kept close to the specimen. In this study, polycarbonate is used for both the transmitter bar and impactor. Sound velocity and density of the impactor and transmitter bar are 1437 m/s and 1.2 g/cm^3. The time required for the complete deformation of the material was first measured by performing preliminary experiments on a similar material. In light of this, the length of the impactor (88 mm) is

chosen in such a way that the time required for the reflected wave to reach impact face of the specimen was always higher than the total time required for the wave to reach the supported end of the sample. This avoids any reloading of the specimen from the reflected wave. The experiments were conducted at three impact velocities 56 m/s, 75 m/s and 94 m/s. In order to check the repeatability of the experiment three experiments are conducted at 56 m/s and two experiments are conducted at 75 m/s.

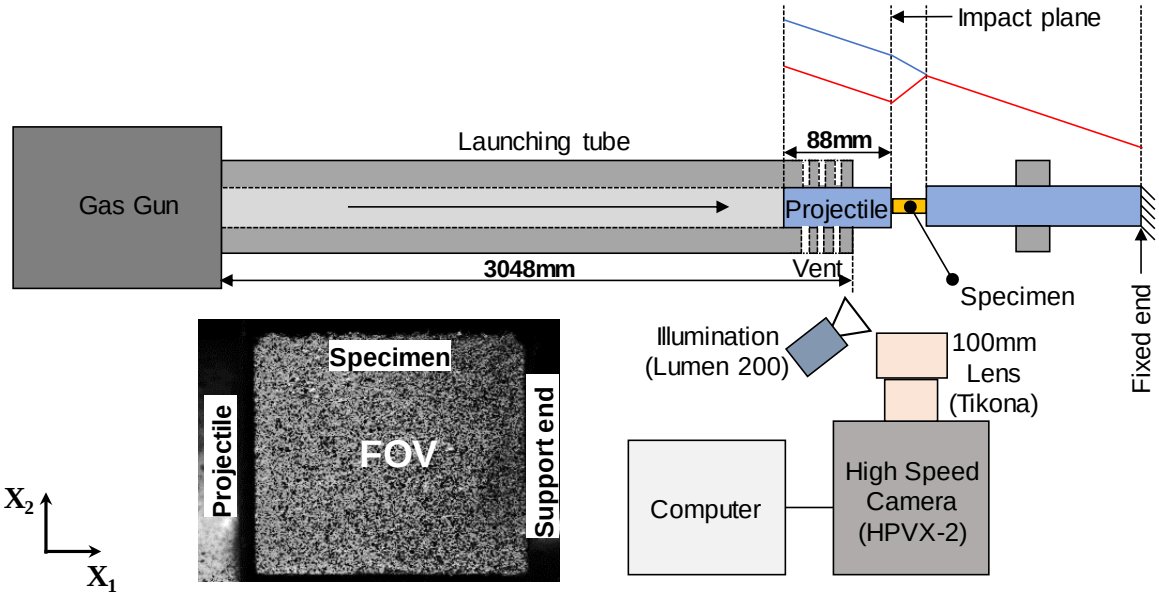

Figure 6.2 Schematic of the complete experimental setup. Image of the speckled sample shows the field of view (FOV) of the imaging setup used. Specimen is attached to the incident bar of a Hopkinson bar.

To observe the full-field macro-scale deformation in-situ, a high-speed camera equipped with a 100 mm Tikona lens is used. An ultrahigh-speed camera HPVX-2 (Shimadzu Inc.), at a framing rate of 2 million frames/sec was employed for high-speed imaging. The camera can capture 128 images at all framing speed with a fixed resolution of 400×250 pixels^2. A metal arc lamp (Lumen 200) is utilized to illuminate the samples, which provides sufficient light for acquiring images at a 2 million/second. The arc lamp is a high intensity, continuous illumination system, which does not require the complicated

triggering that is needed for flashlights commonly used in high-speed photography. The specimen is illuminated only for 10 s to avoid any heating of the sample.

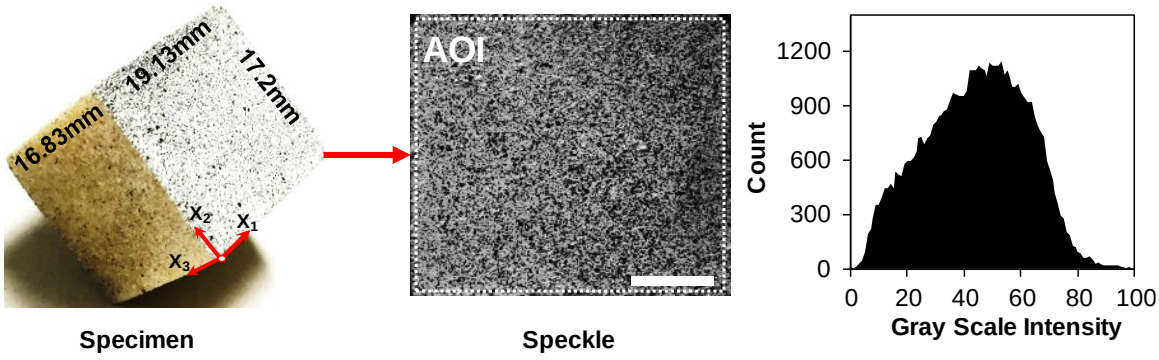

Figure 6.3 (a) Specimen geometry and dimension, (b) typical speckle pattern, (c) gray scale intensity of the speckle pattern.

To facilitate DIC measurement, a high contrast, random, and isotropic speckle pattern must be applied on the surface of the specimen. The size of speckles is carefully selected by considering the image resolution of the optical system used in the experimental setup. As a rule of thumb, for good displacement resolution and accuracy, every speckle has to be sampled by at least 3-5 pixels [30]. The image resolution for the optical setup in this experiment is 74 µm /pixel and, therefore, a speckle size of 240-400 µm is required. These speckles are obtained using an airbrush and flat paint. First, a thin layer of white paint is applied on the surface of the specimen, and after complete drying of the white paint, black paint is sprayed on the top of the white layer using an airbrush. The specimen dimensions and the speckle pattern for the macro-scale DIC measurement are shown in Figure 6.2; a bell-shaped intensity curve is obtained which is ideal for DIC strain measurements. The area of interest (AOI) selected for the DIC calculation in shown on the speckle pattern.

Table 6.1The complete imaging setup camera and post-processing parameters.

Imaging Parameter	Post Processing
Imaging lens- 100 mm Tikona **Illumination**-Lumen 200 PRO, Metal arc Lamp **Imaging Framing Rate**- 2 Million **Resolution**- 400×250 pixel^2 **Field of view**-32×20 mm^2 **Length to pixel ratio**-74 µm/pixel	**Subset Size** -15x15 pixel^2 **Step Size**- 3 pixels **Filter Size**-9

The images acquired in-situ during the deformation process of the specimen are imported in Vic 2D software (correlated solution Inc.) for post processing, following a well-documented procedure available in the literature [30]. As mentioned above, the resolution of the macro-scale experiment is 74 µm/pixel and the average speckle size is 300 µm. Hence, a subset size of 15×15 pixel^2 (1.11×1.11 mm^2) is used considering a minimum of 3×3 speckles in one subset. To gain a good number of data points and to reduce the noise, a step size of 3 pixels and filter size of 9 pixels are selected. The strain calculation in this study was done with the exhaustive search mode, which enables the highest amount of data recovery when correlation fails at the expense of processing time. A higher order interpolation function (Optimized 8-tap) is used to convert discrete digital data points into continuous data. The correlation criterion is chosen to be zero normalized, which is insensitive to the scaling of light intensity. The complete imaging and post-processing parameters are listed in Table 6.1.

6.5 SPATIAL STRESS CALCULATION

The density field can be calculated by using the full-field displacement field obtained from the experiment. Consider the initial density of the specimen as ρ_0, then the density of the material and the initial density of the specimen are related by the following Equation,

$$J\rho = \rho_0 \tag{6.1}$$

Where J is the Jacobian at a point at any time t, and it is calculated by $J=detF$, where F is the deformation gradient and is calculated from the displacement field *(d)* obtained from DIC.

$$F = \begin{bmatrix} 1+\frac{\partial d_1}{\partial X_1} & \frac{\partial d_1}{\partial X_2} & \frac{\partial d_1}{\partial X_2} \\ \frac{\partial d_2}{\partial X_1} & 1+\frac{\partial d_2}{\partial X_2} & \frac{\partial d_2}{\partial X_1} \\ \frac{\partial d_3}{\partial X_1} & \frac{\partial d_3}{\partial X_2} & 1+\frac{\partial d_3}{\partial X_{31}} \end{bmatrix} \tag{6.2}$$

$$J = \det F \approx (1+\varepsilon_{11})(1+\varepsilon_{22})(1+\varepsilon_{33}) \tag{6.3}$$

The compression wave stress before the wave reaches the support end of the specimen can be calculated using the acceleration field obtained from the full-field displacement. A brief description of the method is outlined below. Figure 6.4 shows a depiction of the direct impact experiment in which the wave propagates along the loading direction. The DIC measurement is performed on the face *abcd.*

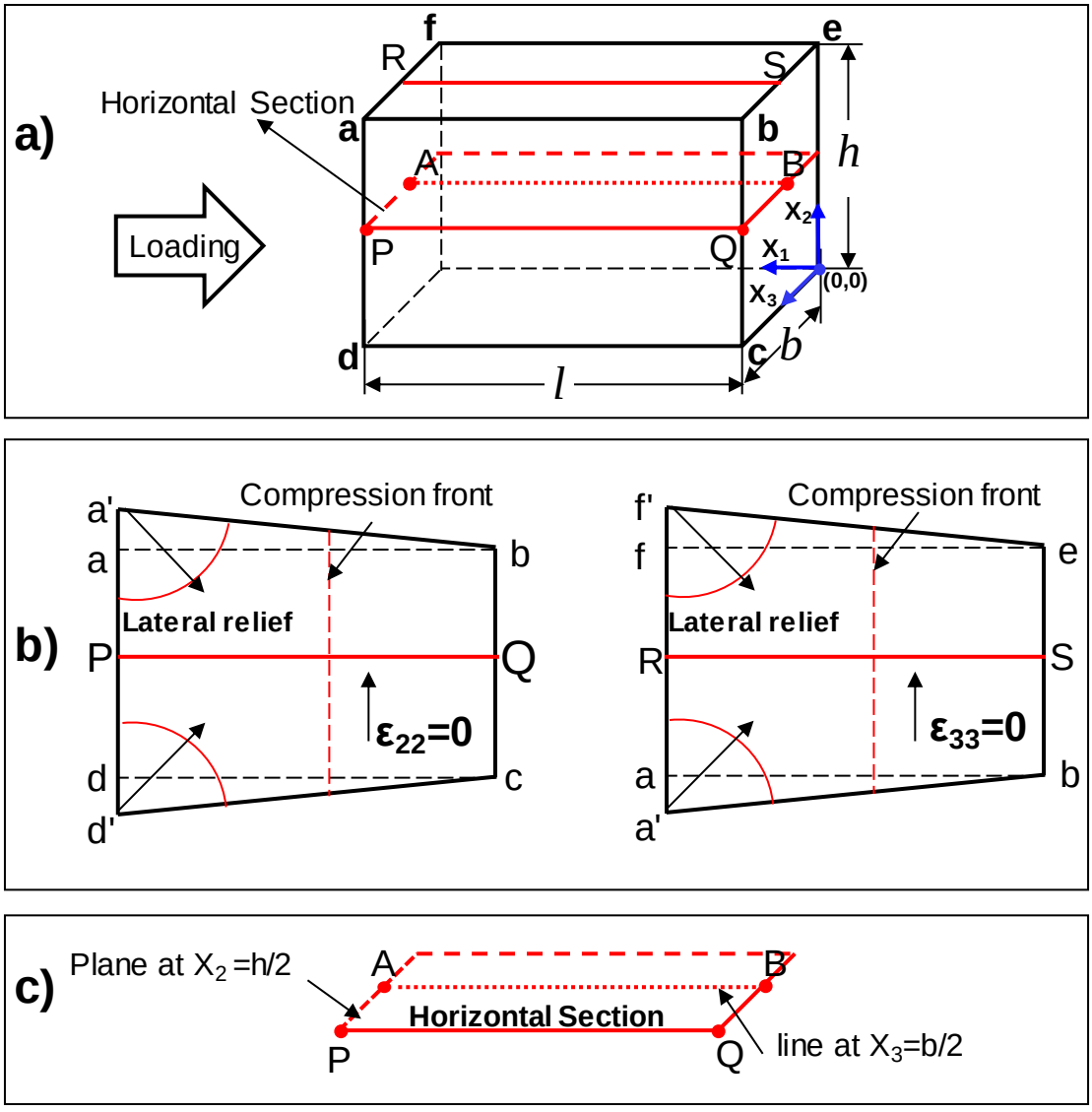

Figure 6.4 a) Depiction of wave propagation and a horizontal section, (b) Lateral relief wave on face abcd and afed, (c) Horizontal section with a small strip marked at X_3= h/2.

The linear momentum conservation in the Lagrangian description by neglecting the body force term can be written as,

$$\nabla \bullet P = \rho_0 \frac{\partial u}{\partial t}\Big|_{X=constant} \qquad (6.4)$$

Where P is the *First Piola Kirchoff's* stress and $\frac{\partial u}{\partial t}$ is the Lagrangian acceleration. The expansion of Eq. 6.4 gives

$$\frac{\partial P_{11}(X_1,t)}{\partial X_1}+\frac{\partial P_{12}(X_1,t)}{\partial X_1}+\frac{\partial P_{13}(X_1,t)}{\partial X_1}=\rho_0\frac{\partial u_1}{\partial t} \quad (6.5)$$

In order to calculate the stress at a point in the specimen Eq. 6.6 is integrated over a differential area dX_2dX_3

$$\int_A\left(\frac{\partial P_{11}(X_1,t)}{\partial X_1}+\frac{\partial P_{12}(X_1,t)}{\partial X_1}+\frac{\partial P_{13}(X_1,t)}{\partial X_1}\right)dX_2dX_3=\int_A\rho_0\frac{\partial u_1}{\partial t}dX_2dX_3 \quad (6.6)$$

The shear terms are negligible which reduces Eq.6.7 to

$$\frac{\partial P_{11}(X_1,t)}{\partial X_1}=\rho_0\frac{\partial u_1}{\partial t} \quad (6.7)$$

Integrating Eq.6.7 to calculate $P_{11}(X_1,t)$ gives the following Eq.,

$$P_{11}(X_1,t)=\int_0^{X_1}\rho_0\frac{\partial u}{\partial t}dX_1 \quad (6.8)$$

In order to calculate the true stress (Cauchy's stress), $P_{11}(X_1,t)$ has to be transformed to the deformed coordinates incorporating change in the volume which can be done by the following general equation,

$$\sigma=J^{-1}F^TP \quad (6.9)$$

Substituting Eq. 6.2 and Eq. 6.3 in Eq. 6.9 gives the axial true stress as,

$$\sigma_{11}(X_1,t)=\frac{P_{11}(X_1,t)}{(1+\varepsilon_{22}(X_1,t))((1+\varepsilon_{33}(X_1,t))} \quad (6.10)$$

Eq. 6.10 is valid at every point in the material. A similar equation was proposed in [31,32]. In this experiment 2D DIC is used, therefore, only in-plane components of strains ε_{11} and ε_{22} are available. However, assuming material isotropy, ε_{33} will have the

same characteristics and value as of ε_{22} at the top edge *(ab)* of the sample. Therefore, all unknowns in Eq. 6.10 can be obtained from the in-plane DIC measurement which enables us to calculate the stress at any points on the face *abcd* of the sample. As shown in Figure. 6.4a, the wave front propagates from the impact end to the support end. At the same time, a tensile lateral relief wave is initiated at the edges of face *abcd* and propagates toward the center of the specimen, as shown in Figure 6.4b. A similar observation can be seen on face *afeb*. The component ε_{22} will be zero in the horizontal line on face *abcd* until the tensile wave reaches the center. A similar observation can be made for ε_{33} on face *afeb*. Therefore, the surface of the specimen is not in uniaxial strain condition at any time 't', however, material points along line *AB* at the center of plane $X_2 = h/2$, see Figure 6.4c, can be regarded as under uniaxial strain condition until the lateral relief from both the edges reaches the center.

In case of uniaxial strain condition, the Eq. 6.10 will be reduced to,

$$\sigma_{11}(X_1,t) = P_{11}(X_1,t) \qquad (6.11)$$

In this study, the measurements are performed on the surface of the sample. Therefore, the stress estimated should be corrected for the out of plane deformation which will significantly affect the stress calculation at higher impact velocity. The correction was performed by calculating stress at the top edge of the sample, which is affected by the lateral deformation in X_3 and X_2 direction. Whereas, the material points along the line joining AB is affected only by the lateral deformation in X_3 direction until lateral relief wave reaches the center. The difference in the stress ($\Delta\sigma$) that is calculated along the top and middle material gives the error in stress calculation due to lateral deformation in one

direction. Therefore, Δσ was added to the stress calculated along the material points PQ in order to estimate the stress along material points along AB. Energy dissipation was estimated from the plastic work rate calculated from the Cauchy's stress, and strain rate calculated from the experiment. The plastic work rate is the product of Cauchy's stress and with the plastic strain rate,

$$\dot{W}_p = \sigma_{ij} : \dot{\varepsilon}_{ij} \qquad (6.12)$$

The energy dissipated per unit volume was computed by integrating Eq.6.12 with time.

6.6 MEASUREMENT PERFORMANCE

To evaluate the performance of displacement measurement, the images that are captured before the projectile impact the specimen were processed using Vic2D software. The post-processing parameters are described in Table 6.1. For an ideal system, before impact, the strain and displacement in the field should read zero everywhere in the field of view. However, a non- zero displacement and strain will be generated in the field due to sources of error such as camera sensor noise, poor speckling, lighting, and improper subset selection.

In order to quantify the error associated with the experiment, the mean value of the axial strain and its standard deviation (SD) are plotted for 10 images of the undeformed specimen as depicted in Figure 6.5a. The mean strain, mainly due to bias, remained very small, less than 0.0015%. The standard deviation is also very small, less than 0.060% compared to the large deformation expected in the impact experiments. The displacement field indicates a SD of about 0.7μm as shown in Figure 6.5b. Uncertainty on the order of 0.7μm is negligible, however the first and second derivative of the displacement field to get acceleration causes significant error in the stress calculation. Therefore, a temporal and

spatial data smoothing was performed using weighted nonlinear smoothing. The smoothed data shows lower SD (~0.25μm) compared to the unsmoothed data. The velocity and acceleration were calculated from the smoothed displacement data and plotted in Figure 6.5c and d which shows that the uncertainty in velocity and acceleration are 0.08m/s and 0.175×10^5 m/s^2 respectively, this value is negligible compared to the expected material velocity (~45m/s) and acceleration (~10^6 m/s^2) in the experiment.

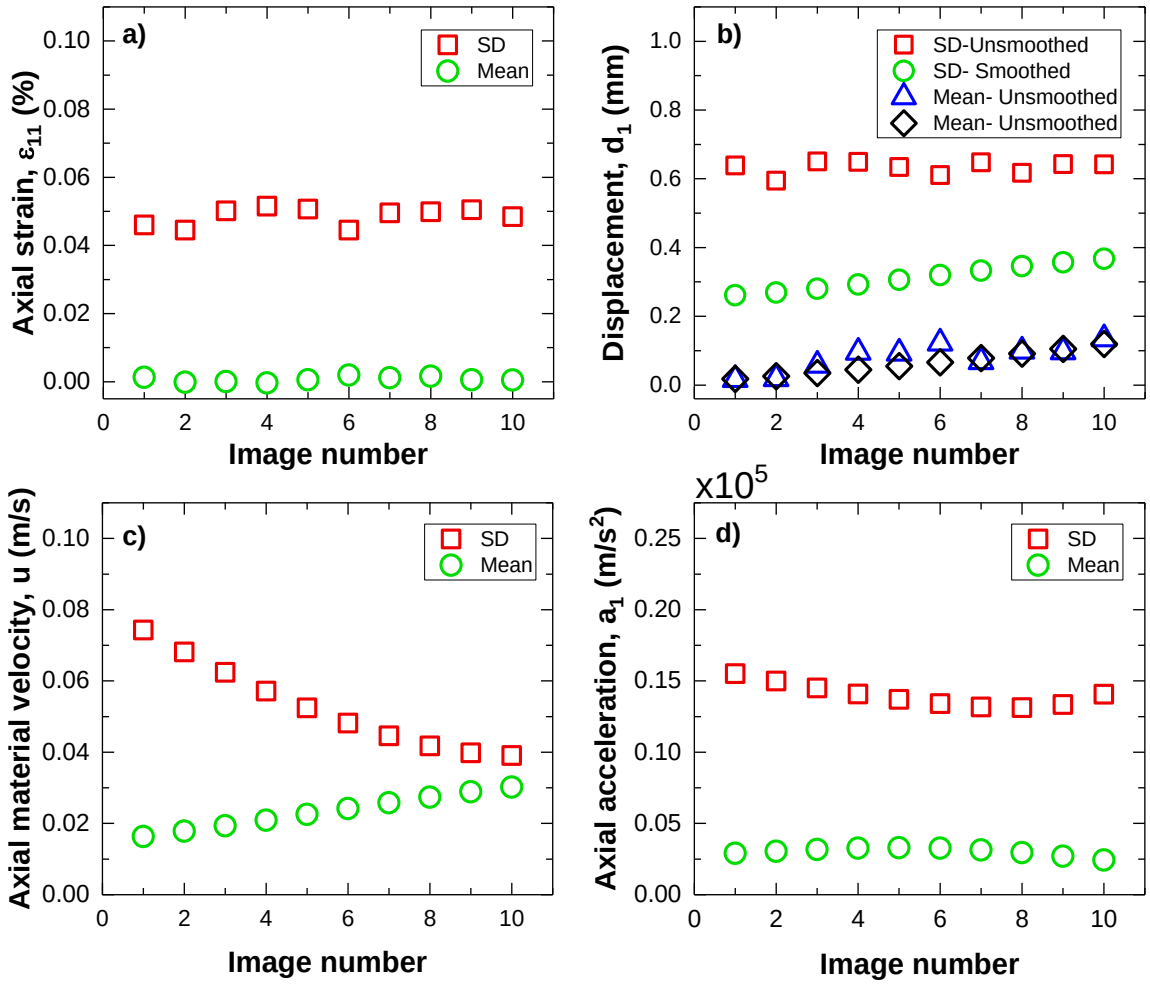

Figure 6.5 Mean and the standard deviation of, (a) strain, (b) displacement, (c) axial material velocity, and (d) axial acceleration in 10 undeformed images of the speckled specimen.

The acceleration and displacement data are used to calculate the Cauchy stress in the material. The propagated uncertainty in the stress calculation was calculated based on the uncertainty values of the acceleration and displacement. In the true stress calculation, the variables that are required are the acceleration, Jacobian, and deformation gradient. The true stress uncertainty can be calculated by the following equation,

$$\frac{\delta\sigma}{\sigma} = \sqrt{\left(\frac{\delta J}{J}\right)^2 + \left(\frac{\delta a}{a}\right)^2 + \left(\frac{\delta F}{F}\right)^2} \qquad (6.13)$$

Uncertainty in Jacobian, acceleration, and deformation gradients are calculated from the displacement uncertainty in the measurement system.

6.7 RESULT AND DISCUSSION

It should be noted that all the discussions are limited to the time duration of the propagation of the wave from the impact end to the support end of the sample. The full-field data at each point reported by the DIC analysis is an average value of a subset size of 15×15 pixel^2. The data is calculated at the center of the subset, which leaves out about 8 pixels from each side of the area of interest. In addition, due to the insufficient contrast of the speckles close to the impact face, region 4 pixels away from the boundary is selected as the area of interest for DIC post-processing Therefore, the displacement and strain fields obtained are 12 pixels (X_1=0.894 mm) away from the impact face. The term "impact face" corresponds to a location 0.894 mm away from the face of contact between the projectile and the specimen. Due to the similarity between the results, the full analysis for the 56 m/s experiment are presented and the higher velocity results are included for comparison where needed.

6.7.1 Axial stress wave and lateral stress relief

The distribution of true full-field axial strain along the length of the specimen at time t=0, 5, 10, 15, 20, 25, and 35 μs is shown in Figure 6.6a. From the figure, it is evident that a compression wave was formed and propagated from the impact end to the support end of the specimen. The compressive axial strain behind the wavefront, is significantly high, whereas ahead of the wavefront, the axial strain is zero indicating undisturbed region. The strain vs time plot at point A shown in Figure 6.6c indicates that the axial strain linearly increases with time until time t=8-9 μs. After this point, the axial strain is approximately constant which indicate compaction type wave seen in the granular explosives. It is possible that a maximum compaction, ie. Quasi-steady condition, in the region, is achieved. The axial strain field in Figure 6.6a ascertains two points, 1) the wavefront has a finite thickness that changes with time, and 2) the wavefront is planar at the beginning but becomes non-planar as it propagates across the specimen. The wide compaction type band observed indicates a weak shock nature and could be due to a low impact velocity applied to the specimen. On the other hand, the non-planar wavefront observed at a later time of wave propagation could be due to the arrival of a lateral relief wave from the two edges of the sample. In order to investigate the formation of the non-planar front, lateral strain (ε_{22}) is plotted in Figure 6.6b. The lateral strain field shows a tensile strain expanding from the left corners of the area of interest of the sample as discussed in section 2.4. This lateral deformation generates a diagonally propagating expansion stress wave (lateral relief) towards the center of the specimen at a velocity close to the sound velocity of the material in the compressed region. To visualize the propagation of the lateral relief, a quiver plot is shown in Figure 6.6b, which clearly shows the propagation of the lateral relief wave. The

axial and lateral strain at point A (X_2=h/2=8.65 mm) is plotted in Figure 6.6c to find the time at which the lateral relief reaches the center of the specimen. Lateral strain ε_{22} is close to zero for a time period of 16 μs after the impact. At time t=16 μs, a non-zero lateral strain is observed, and it increases linearly with time, as shown in Figure. 6.6c. Later, these two tensile waves merge together and propagate along the loading direction of the sample as shown in Figure 6.6b. A similar observation can also be expected on the face aefg, where, ε_{33} will be zero at the center along the material points in line RS, until t=16μs, as shown in Figure 6.4b. Therefore, until the relief wave due to transverse deformation in X_2 and X_3 reaches the line AB, center plane X_2=h/2, the deformation along line AB will be under uniaxial strain condition. Therefore, the axial stress that is calculated along line AB using the Eq. 6.11 assuming axial displacement of material points in line AB is same as that of PQ and will be approximately equal to the stress associated with the stress wave under uniaxial strain assumption. Figure 6.6d shows the axial strain field at 10 μs for the three impact velocities considered in this study. It shows that the wave front position for higher impact velocity is farther from the impact comparing to the lower impact velocity indicating higher wave speed at higher impact velocity.

It is very important to note that, in granular materials, the compaction waves are formed by the distortion of the crystals when the local stress exceeds the yield strength of the crystal. In case of low-velocity impact (stresses below the yield strength of the constituent material), the plastic deformation of the crystals is primarily due to the stress concentration associated with the force chain formation. In this study, as discussed later in section 3.5, the maximum average stress behind the compaction front is about 25 MPa for the lowest velocity impact loading (56 m/s), which is very far from the yield stress (110 MPa) of the

sugar crystal. Furthermore, the material used in this study is comprised of a soft binder in addition to crystals which reduces the number of crystal-crystal contact points, therefore, less stress concentration locations and the plastic deformation of the crystals. In the present case, the primary mechanism of the compaction is the deformation of the soft binder which squeezes out the pores. The plastic deformation of the crystals may be playing a minor role in the compaction wave formation and propagation.

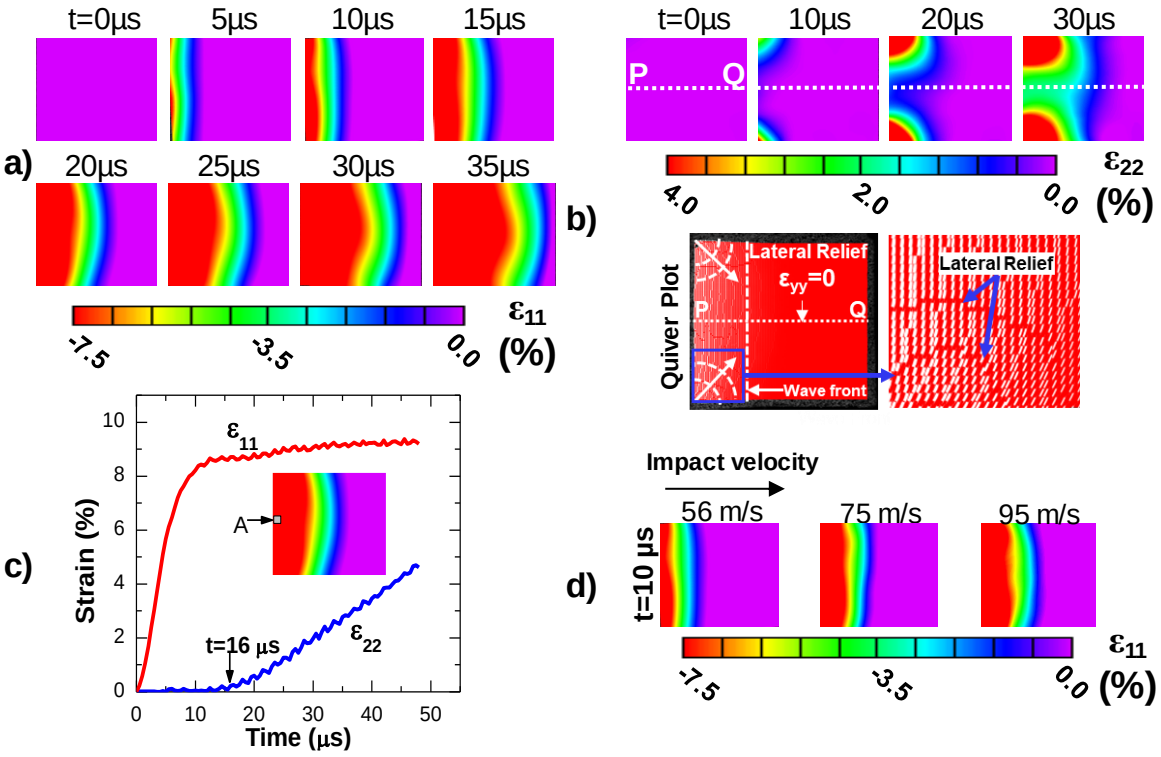

Figure 6.6 (a) Axial strain field at t=0,5,10,15,20,25,30 and 35 µs, propagation of the compressive wave from the impact end and to support end is manifested, (b) transverse strain field at t=0, 5, 10.15,20,25,30 and 35 µs, lateral relief wave from both the left corners is shown in Quiver vector plot. (c) axial and transverse strain at a location A with time. The figure inside shows the point at which the strains are extracted, (d), axial strain field at t=10 µs for the impact velocities 56, 75 and 95 m/s.

6.7.2 X_1-t diagram and spatial density variation

The X_1-t diagram in Figure 6.7a shows the location of the wavefront at different times. A linear fit is obtained for the wavefront location with time indicating no change in

the wave velocity with time. The wavefront velocity of 505 m/s is obtained by calculating the slope of the linear fit. Wave velocity estimated as 1.18 times the sound speed in the material indicating a weak shock formation in the material. In this study, the shock wave velocity estimated is higher compared to the porous explosives that were investigated previously under similar impact velocities [33]. This is due to the presence of binder in the material which provides more paths for the force transfer between crystals compared to porous explosives in which the sole mechanism of force transfer is crystal-to-crystal contact [15]. In addition, the porosity in the material used in this study is less compared to the porous explosives which also increases the shock wave velocity in the material. Figure.6.7b shows shock velocity estimated for three different impact velocities considered in the study. Shock velocity for the impact velocities 73±2 m/s and 94±3 m/s gives relatively a wave speed close to 706.5±80 m/s and 825 ± 50 m/s, see Figure 6.7b.

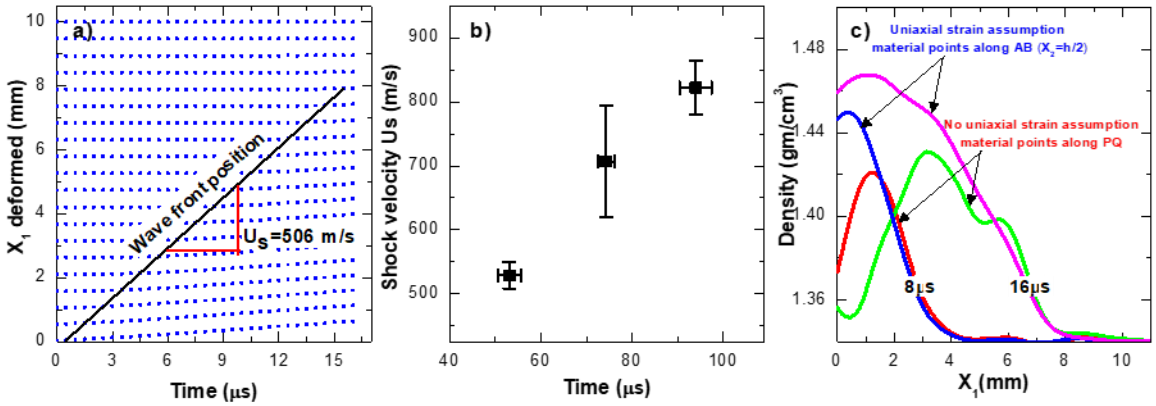

Figure 6.7 (a) X_1-t diagram for the impact velocity 56 m/s and slope of the linear fit gives the shock velocity U_s=506 m/s, (b) shock velocity for three impact velocities, 53.1±2.6 m/s, 74.3±1.83 m/s and 94±3.5 m/s, (c) spatial density variation at t=8 μs and 16 μs at impact velocity 56 m/s.

The instantaneous density of the material is calculated using Eq.6.2. The variation of the density along the line PQ at a different location is plotted in Figure 6.7c. A maximum density of 1.425 g/cm3 is observed in the compacted region behind the front. For an ideal

shock (uniaxial strain) condition, a constant density is expected behind the shock front. However, for unconfined experiment considered in this work, due to the transverse strain in X_3 and X_2 direction, the density in the region behind the shock front is not constant. The density profile is shown to have a low density close to the impact end due to the high transverse strain in the X_3 direction. As discussed above, the transverse strain in X_2-direction is negligible until t=16 μs. On the other hand, the density calculated along the line material points AB where uniaxial strain condition prevails gives a maximum density behind the shock front as 1.46g/cm^3. The density behind the front is close to the theoretical maximum density of the sample. In addition, the density is nearly constant behind the shock front.

6.7.3 Full-field particle velocity

The full-field particle velocity is qualitatively similar to the axial strain field shown in section 6.7.1 (see Figure 6.6a and Figure 6.8a). The particle velocity across the specimen is divided by a thick shock front with a constant velocity behind the shock front (fully compacted). Whereas, ahead of the shock front, a zero-velocity region (undisturbed) is observed. The velocity along the centerline at seven different Lagrangian locations, at X_1=0, 1, 2, 3, 4, 5 and 6 mm from the impact end, is shown in Figure 6.8b. Note that, the impactor has a significantly higher impedance compared to the polymer-bonded sugar samples. Therefore, the particle velocity in the sample is expected to be close to the impact velocity of the projectile. The impact velocity is 56 m/s and the peak particle velocity is found to be 41 m/s at the impact end. The rise time at the impact end (X_1=0) is close to 8μs, whereas at X_1=6 mm, the rise time is 10μs. Also, as the shock wave travels across the specimen, the peak particle velocity decreases from 41 m/s at X_1=0 to 37 m/s at X_1=6 mm,

indicating, a reduction in shock strength. The decrease in the wave strength is an indication of energy dissipation in the material. The mechanism of the dissipation is not determined from the experiments; it is possibly attributed to localized plastic deformation of the binder, crystal fracture, and frictional heating can contribute to the energy dissipation [12,16]. In order to see the shock wave profile, the particle velocity is plotted along X_1 as shown in Figure 6.8c. interestingly, the wave profile is very similar to the weak shock profile seen in the piston compression numerical simulation of disordered brittle spheres [34]. The particle velocity at the impact face behind the shock wave front increases from 0 m/s at t=0 μs to 40 m/s at t=8 μs. Interestingly, the particle velocity behind the shock front after t=8μs is nearly constant indicating a possible attainment of a quasi-steady state.

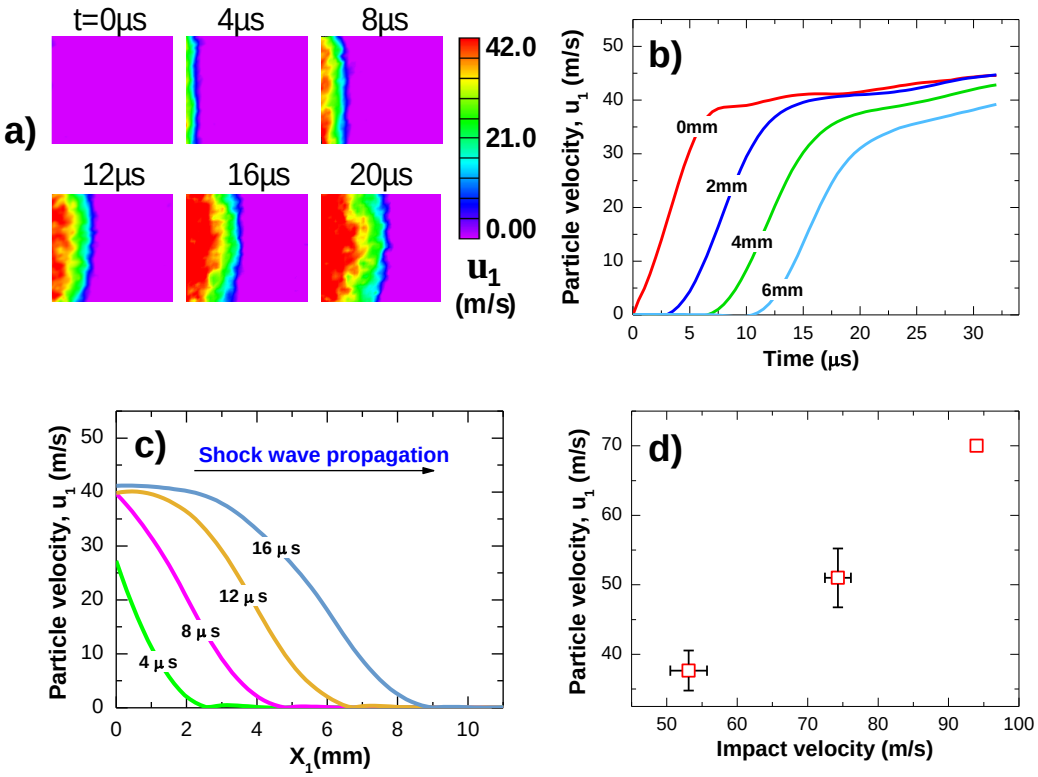

Figure 6.8 (a) Contour plot of axial particle velocity with time at t=0, 4, 8, 12, 16 and 20 μs, (b) axial particle velocities at different Lagrangian locations with time, (c) particle velocity along Lagrangian axial coordinates at t= 4, 8, 12 and 16 μs. Uncertainty in the velocity is 0.08 m/s, (d) particle velocity for three impact velocities.

6.7.4 Shock thickness

In the case of an ideal strong shock front, gradient across the shock wave front will be infinite. Nevertheless, a real shock wave will have a finite rise time corresponding to material deformation, and the slope of the shock wave front will vary with the strength of the shock wave. Across the shock wave front, discontinuity in strain, stress and material velocity is expected. It is important to note here, in the case of weak shock waves, the front will have a finite thickness and therefore the gradient across the shock wave front will not be sharp compared to a strong shock as shown in Figure 6.9a. Hence, in order to understand the process of shock formation under weak shock condition characteristics, a complete analysis of the shock wave thickness is required. Shock front wave thickness is an important quantity which determines the gradient of stress, strain or velocity across the wavefront. The shock wave thickness 'δ' can be defined as shown in Eq. (6.14)

$$\text{Shock wave thickness, } \delta = \frac{u_1}{\max\left(\frac{\partial u_1}{\partial x}\right)} \qquad (6.14)$$

Where 'u_1' is the particle velocity behind the compaction front. Since the material velocity is directly calculated from DIC, the compaction wave thickness can be easily calculated from Eq.6.14.

The particle velocity, as well as its gradient at three different instances across the length of the specimen, is shown in Figure 6.9a. The axial location of the maximum velocity gradient is indicated by a circular marker. The gradient of the velocity shows a sharper peak at t=8 μs compared to velocity gradient peak at t=16 μs. This is attributed to the dispersion or dissipation of the shock wave as it travels across the specimen.

The shock wave thickness is calculated using Eq. (6.14) and plotted in Figure 6.9b. Inside the shock front, the pores are collapsed, and the crystals reorient themselves and may even fracture due to the stress concentrations as a result of force chain formation. It is seen that the shock wave thickness is close to ~3.4-3.8 mm (6-7 crystals) and it is nearly constant for a time period of t=8-12 μs, however, after t=12μs, the shock thickness gradually increases to ~4.1-4.5 mm (8-9 crystals). Interestingly, the numerical simulation of the compaction wave in porous high melting explosives under constrained experiments shows a constant wave thickness of 5.1 mm.

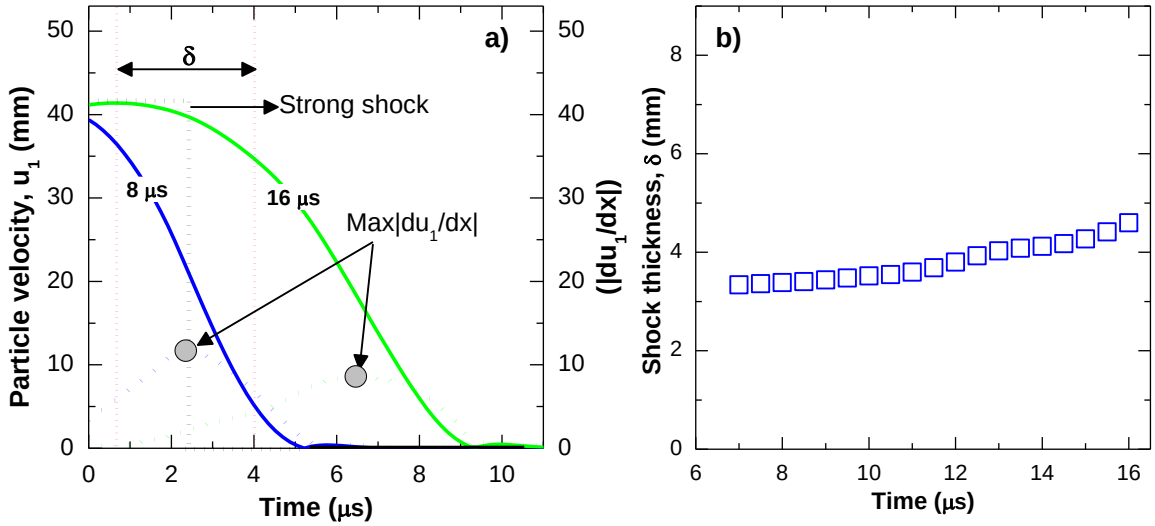

Figure 6.9 (a) The particle velocity and its gradient along different Lagrangian axial coordinates. (b) shock wave thickness evolution with time.

A dissipative compressive front will always tend to broaden; however, the material nonlinearity effect steepens the wavefront [35]. In the case of a steady shock wave, there is a balance between the broadening due to dissipation and steepening due to non-linearity. Therefore, in this study, a nearly constant shock thickness right after the attainment of quasi-steady condition would indicate a balance of dissipation and nonlinear steepening. However, at later times (> 12μs), the increased broadening is attributed to either dissipation

becoming dominant or the transformation of the planar front to a non-planar front due to lateral wave release. Shock experiments on the granular material at very high impact velocity shows a similar increase in thickness of the front with time. In order to distinguish the shock front widening mechanisms, it would be ideal to perform a constrained experiment in which the effect of relief wave will be minimal. However, this is out of the scope of this work and could be a future research subject. In this study, the dissipation of the energy by estimating the stress and strain from the displacement field was calculated. For other impact velocities considered in this study, the shock thickness was not appeared to be significantly different from the 56 m/s.

6.7.5 Axial stress from full-field acceleration and energy dissipation

Spatial acceleration profile is plotted in Figure 6.10a. It is seen that the acceleration at any Lagrangian axial location increases to a peak value when the shock wave arrives and drops to zero when it departs as shown in Figure 6.10b. The acceleration profile is shown in Figure 6.10c has a typical structure of a stress wave in materials. The peak value of the acceleration is dropping as the wave traverses across the sample (See Figure 6.10b and Figure 6.10c). This could be due to energy dissipation or/and possible dispersion of the shock wave discussed in previous sections. The acceleration dropping drastically behind the peak indicates an attainment of constant velocity behind the shock front. For instance, consider t=8 μs and 16 μs, two important points to be noted. 1) A decrease in the peak value of acceleration and, 2) widening of the pulse with time. The drop in peak acceleration is calculated as 8.48×10^{5} m/s^{2} which are 15% of the peak acceleration at t= 8μs. This indicates the dissipative characteristics of the shock wave.

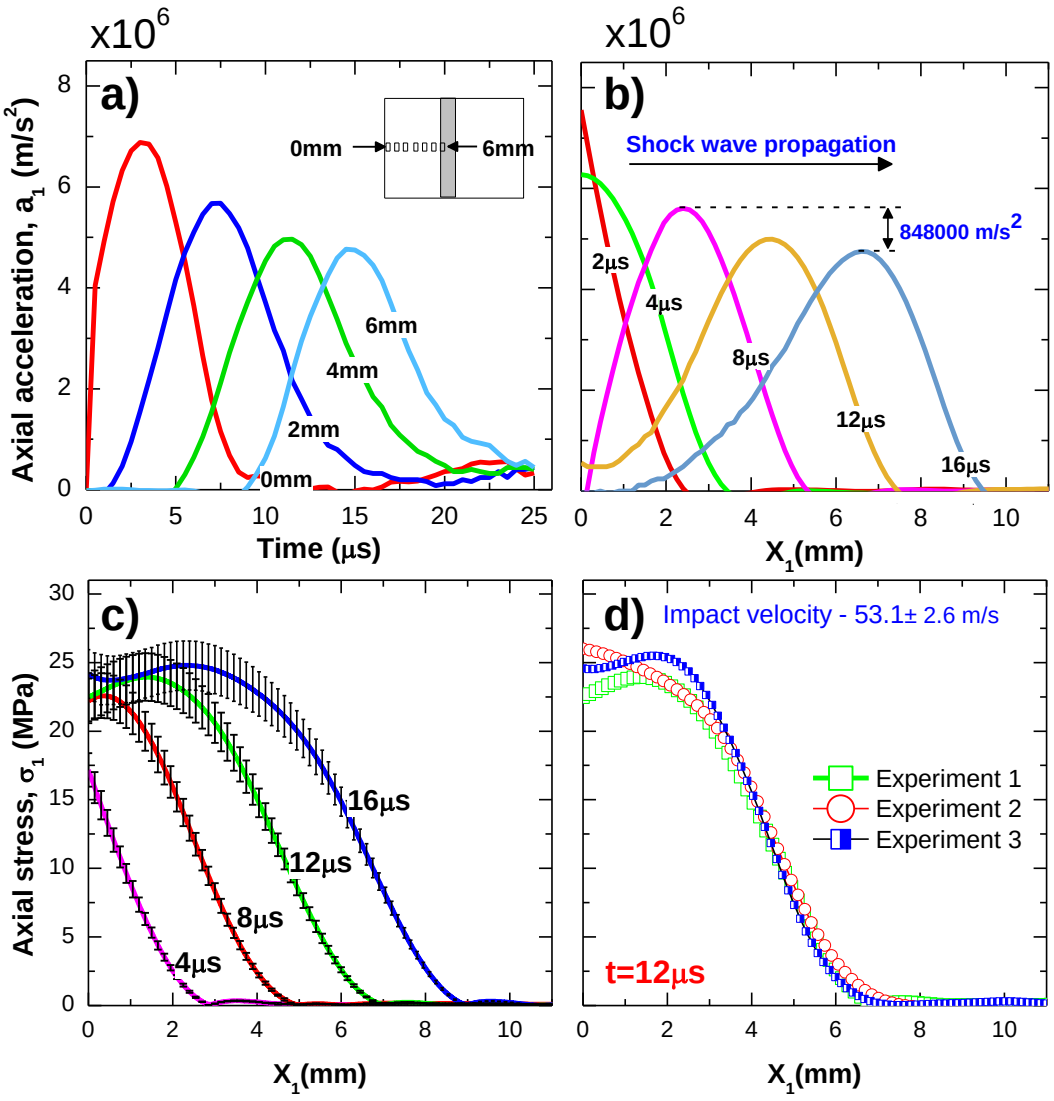

Figure 6.10 (a) axial acceleration different Lagrangian locations with time, (b) axial acceleration along the axial Lagrangian coordinates at a different time, (c) axial stress different Lagrangian locations with time, (d).) axial stress different Lagrangian locations for three different experiments. Uncertainty in acceleration is 1.8×10^4 m/s^2.

To quantify the energy dissipated, the axial stress is calculated using the inertia stress analysis discussed in section 6.4. The first Piola-Kirchhoff stress is calculated using Eq. (6.9). In order to calculate the true stress Eq.6.11 is used and the correction to the stress was performed as described in the methods section. The axial stress at a different Lagrangian location along the specimen at different time step t=4, 8, 12 and 16 μs are shown in Figure 6.10c. Behind the shock front, stress is approximately constant (close to

25 MPa) and ahead of the front stress is zero. The plot also shows the measurement and experimental error interval for each stress calculations. To confirm the repeatability of the stress estimation, the results from two more experiments at impact velocity close to 56 m/s were presented, see Figure 6.10d. Interestingly, the axial stress profiles are identical and the stress behind the front is within 10 %.

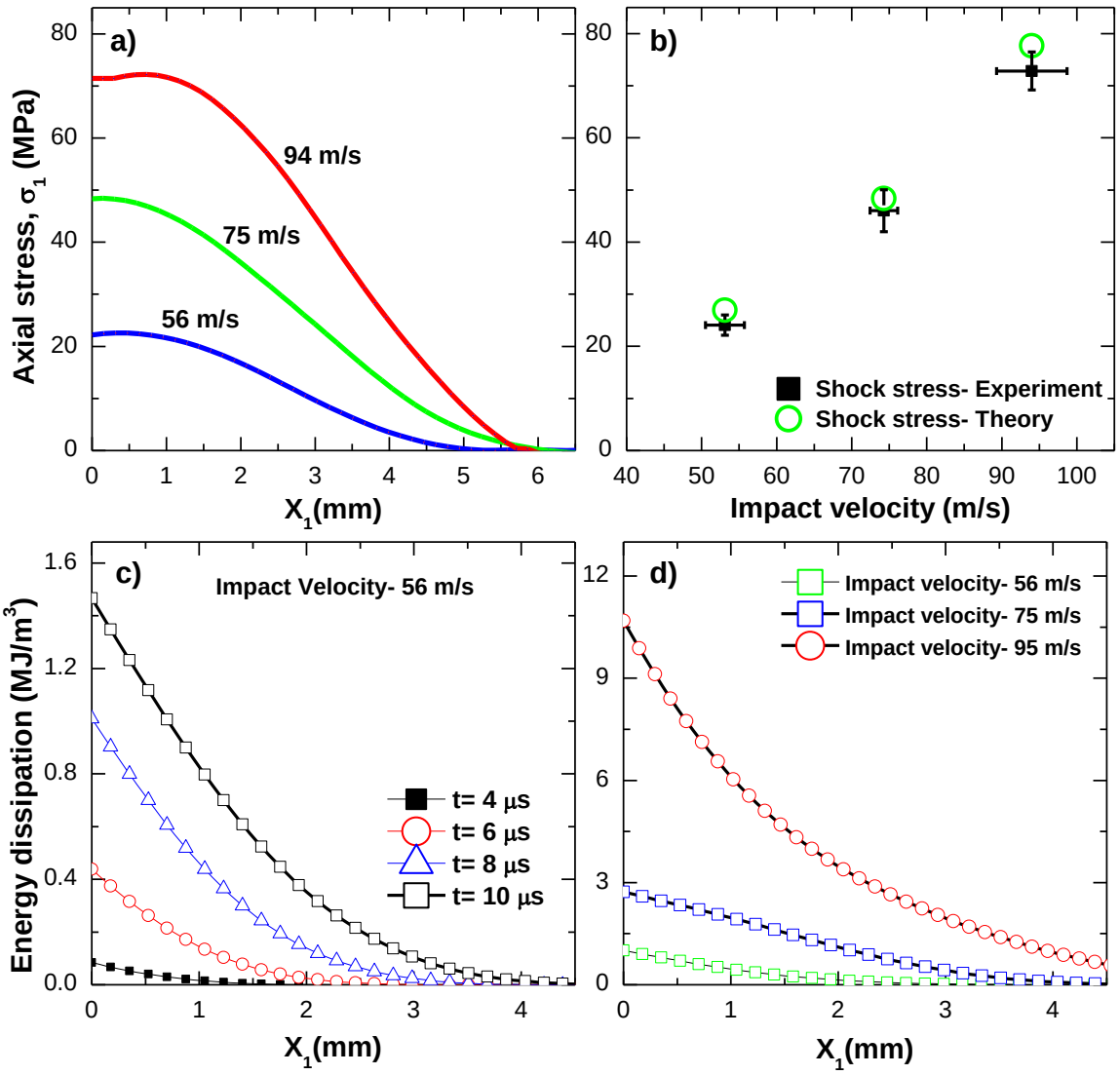

Figure 6.11 (a) Axial along different Lagrangian axial coordinates for three impact velocities, 56 m/s, 75 m/s and 94 m/s, (b) stress behind shock front from experiment and theory for three impact velocities, (c) energy dissipation at t=4, 6, 8 and 10 μs for impact velocity 56 m/s, (d) energy dissipation at t= 8 μs for impact velocities 56 m/s, 75 m/s and 94 m/s.

Stress profile for three impact velocities considered in this study is shown in Figure 6.11a. The stress behind the shock front for impact velocities 56, 75 and 94 m/s are close to 25, 48 and 72 MPa, respectively. The shock theory predicted axial stress of 27.81, 51.2 and 78.6 MPa for the impact velocities 56, 75 and 94 m/s, respectively. As the impact velocity increases, the error associated with the stress estimation seems to be slightly increasing which is probably due to significant out plane deformation.

Figure 6.11c shows the energy dissipation calculated using Eq.6.12 for impact velocity of 56 m/s. The energy dissipation is high near to the impact end and it increases with time. The energy dissipation for three impact velocities (56, 75 and 94 m/s) at t=8 μs is shown in Figure 6.11d. Dissipation profile for all the impact velocities are relatively identical and the energy dissipation was seen to drastically increase with the higher impact velocity. The energy dissipation near impact face for impact velocity 56, 75, and 94 m/s is close to 0.9, 2.9 and 10.23 MJ/m^3, respectively. An increase in dissipated work indicates a higher temperature for higher impact velocity and which may cause hotspot formation and a following sensitization of the explosives.

The possible energy dissipation mechanisms in PBS are fracture of crystals, plastic deformation of the binder, and frictional relative movement of the crystals [8,9,11,15,16]. However, a detailed understanding of grain scale mechanisms can be achieved by performing high spatial and temporal resolution experiments. The present study is limited to the macro-scale investigation but a meso-scale study could be a future research that can unfold the mechanisms associated with the energy dissipation. Authors are currently performing experiments at higher magnification to quantify the deformation mechanisms at the microscale.

6.8 CONCLUSION

In this work, we have developed an optical-based experimental method to investigate the weak shock wave properties of PBS subjected to impact loading. Specimens made of polymer bonded sugar are subjected to projectile impact and the propagation of the weak shock wave is captured with the help of high-speed optical imaging. A quantitative analysis of the shock wave structure, such as shock wave velocity, shock front thickness and full-field strain and stress is performed with the help of digital image correlation. The energy dissipated as a function of time is also calculated based on the stress-strain relation obtained in the experiment. The key findings are summarized as:

- For the material considered in this study the shock wave velocity is close to 506 m/s for a projectile impact velocity of 56 m/s. The shock wave velocity was slightly higher than the sound speed in the material. The wave structure was observed to be of weak shock nature with a wide shock front.
- The time required to achieve the quasi-steady condition was close to 8 μs, which appears to increase as the wave propagating along the specimen.
- The experimental study indicates that compaction wave can generate in PBX at a stress much less than the plastic deformation of the crystals. In this case, the compaction is generated due to plastic or viscoelastic deformation of the binder.
- The shock wave front thickness was experimentally estimated from the material velocity. It is nearly constant (3.1-3.4 mm) after the attainment of quasi-steady condition and it gradually increases as it propagates (4.1-4.6 mm). Widening may be due to the dissipation domination or the evolution of the non-planar front as a result of

a lateral relief wave. The thickness of the shock front is close to the numerically estimated value of 5.1 mm in porous explosives by [36].

- The shock wave stress in the material is effectively estimated based on the full-field deformation measured using DIC and validated using 1D shock wave calculation.
- Energy dissipated during shock propagation calculated from the stress-strain relation obtained from the estimated stress and measured axial strain.

6.9 LIST OF REFERENCES

[1] Baer MR. Modeling heterogeneous energetic materials at the mesoscale. Thermochim Acta 2002;384:351–67.

[2] Beckvermit JC, Peterson JR, Harman T, Bardenhagen S, Wight CA, Meng Q, et al. Multiscale Modeling of Accidental Explosions and Detonations. Comput Sci Eng 2013;15:76–86.

[3] Field JE. Hot spot ignition mechanisms for explosives. Acc Chem Res 1992;25:489–96.

[4] Tarver CM, Chidester SK. On the violence of high explosive reactions. J Press Vessel Technol 2005;127:39–48.

[5] Ravindran S, Tessema A, Kidane A. Effect of Crystal Density on Dynamic Deformation Behavior of PBX. Challenges Mech. Time Depend. Mater. Vol. 2, Springer; 2017, p. 87–92.

[6] Ravindran S, Tessema A, Kidane A, Sutton MA. Meso-scale Deformation Mechanisms of Polymer Bonded Energetic Materials Under Dynamic Loading. Mech. Compos. Multi-functional Mater. Vol. 7, Springer; 2016, p. 451–6.

[7] Chakravarthy S, Gonthier KA. Analysis of microstructure-dependent shock dissipation and hot-spot formation in granular metalized explosive. J Appl Phys 2016;120:24901.

[8] Parab ND, Roberts ZA, Harr MH, Mares JO, Casey AD, Gunduz IE, et al. High speed X-ray phase contrast imaging of energetic composites under dynamic compression. Appl Phys Lett 2016;109:131903.

[9] Wang X, Wu Y, Huang F, Jiao T, Clifton RJ. Mesoscale thermal-mechanical analysis

of impacted granular and polymer-bonded explosives. Mech Mater 2016;99:68–78.

[10] Hu Z, Luo H, Bardenhagen S, Siviour C, Armstrong R, Lu H. Internal deformation measurement of polymer bonded sugar in compression by digital volume correlation of in-situ tomography. Exp Mech 2015;55.

[11] Barua A, Horie Y, Zhou M. Energy localization in HMX-Estane polymer-bonded explosives during impact loading. J Appl Phys 2012;111:54902.

[12] Barua A, Zhou M. A Lagrangian framework for analyzing microstructural level response of polymer-bonded explosives. Model Simul Mater Sci Eng 2011;19:55001.

[13] Trott WM, Baer MR, Castañeda JN, Chhabildas LC, Asay JR. Investigation of the mesoscopic scale response of low-density pressings of granular sugar under impact. J Appl Phys 2007;101:24917.

[14] Field SGG and CRS and WGP and JE. High-strain rate Brazilian testing of an explosive simulant using speckle metrology. Meas Sci Technol 2004;15:1867.

[15] Bardenhagen SG, Brackbill JU, Sulsky D. Numerical study of stress distribution in sheared granular material in two dimensions. Phys Rev E 2000;62:3882.

[16] Ravindran S, Tessema A, Kidane A. Local Deformation and Failure Mechanisms of Polymer Bonded Energetic Materials Subjected to High Strain Rate Loading. J Dyn Behav Mater 2016;2:146–56.

[17] Panchadhara R, Gonthier KA. Mesoscale analysis of volumetric and surface dissipation in granular explosive induced by uniaxial deformation waves. Shock Waves 2011;21:43–61.

[18] Barua a., Horie Y, Zhou M. Microstructural level response of HMX-Estane

polymer-bonded explosive under effects of transient stress waves. Proc R Soc A Math Phys Eng Sci 2012;468:3725–44. doi:10.1098/rspa.2012.0279.

[19] Tarver CM, Forbes JW, Garcia F, Urtiew PA. Manganin gauge and reactive flow modeling study of the shock initiation of PBX 9501. AIP Conf. Proc., vol. 620, AIP; 2002, p. 1043–6.

[20] Gustavsen RL, Aslam TD, Bartram BD, Hollowell BC. Plate impact experiments on the TATB based explosive PBX 9502 at pressures near the Chapman-Jouguet state. J. Phys. Conf. Ser., vol. 500, IOP Publishing; 2014, p. 52015.

[21] Dick JJ, Martinez AR, Hixson RS. Plane impact response of PBX 9501 and its components below 2 GPa. Los Alamos National Lab., NM (United States); 1998.

[22] Ravindran S, Tessema A, Kidane A. Note: Dynamic meso-scale full field surface deformation measurement of heterogeneous materials. Rev Sci Instrum 2016;87:36108.

[23] Bodelot L, Escobedo-Diaz JP, Trujillo CP, Martinez DT, Cerreta EK, Gray GT, et al. Microstructural changes and in-situ observation of localization in OFHC copper under dynamic loading. Int J Plast 2015;74:58–74.

[24] Huang JY, Lu L, Fan D, Sun T, Fezzaa K, Xu SL, et al. Heterogeneity in deformation of granular ceramics under dynamic loading. Scr Mater 2016;111:114–8.

[25] Asadi M. Beet-sugar handbook. John Wiley & Sons; 2006.

[26] Millett JCF, Bourne NK. The shock Hugoniot of a plastic bonded explosive and inert simulants. J Phys D Appl Phys 2004;37:2613.

[27] Siviour C., Laity P., Proud W., Field J., Porter D, Church P., et al. High strain rate properties of a polymer-bonded sugar: their dependence on applied and internal

constraints. Proc R Soc A Math Phys Eng Sci 2008;464:1229–55. doi:10.1098/rspa.2007.0214.

[28] Peterson PD, Mortensen KS, Idar DJ, Asay BW, Funk DJ. Strain field formation in plastic bonded explosives under compressional punch loading. J Mater Sci 2001;36:1395–400.

[29] Drodge DR, Williamson DM, Proud WG. Split Hopkinson Pressure Bar Techniques for the Estimation of a High Strain-rate Elastic Modulus 2008.

[30] Sutton MA, Orteu JJ, Schreier H. Image Correlation for Shape, Motion and Deformation Measurements: Basic Concepts,Theory and Applications. Springer Science & Business Media; 2009.

[31] Koohbor B, Kidane A, Lu W-Y, Sutton MA. Investigation of the dynamic stress–strain response of compressible polymeric foam using a non-parametric analysis. Int J Impact Eng 2016;91:170–82.

[32] Othman R, Aloui S, Poitou A. Identification of non-homogeneous stress fields in dynamic experiments with a non-parametric method. Polym Test 2010;29:616–23.

[33] Sandusky HW, Liddiard TP. Dynamic compaction of porous beds. DTIC Document; 1985.

[34] Gómez LR, Turner AM, Vitelli V. Uniform shock waves in disordered granular matter. Phys Rev E 2012;86:41302.

[35] Grad H. The profile of a steady plane shock wave. Commun Pure Appl Math 1952;5:257–300.

[36] Baer MR. Numerical studies of dynamic compaction of inert and energetic granular materials. J Appl Mech 1988;55:36–43.

CHAPTER 7

MULTISCALE WEAK SHOCK WAVE PROPAGATION IN POLYMER BONDED EXPLOSIVES

[1]*Ravindran, S.,* Tessema, A. & Kidane, A. *In preperation.*

7.1 ABSTRACT

In this study, we present a multiscale experimental investigation of polymer bonded explosives under dynamic loading conditions to characterize compaction wave propagation. The measurement is performed with the help of ultrahigh-speed photography incorporating digital image correlation (DIC). From the macroscale experiment, the compaction wave velocity was estimated to be 505m/s. In addition, the compaction profile was of weak shock nature with an increase in compaction wave thickness with time. The increase in compaction wave width is observed to be due to the dissipation of the energy. Whereas the mesoscale experiment shows a force chin structure within the compaction band. The dissipation mechanisms at mesoscale was observed to be grain fracture, plastic deformation and possible relative sliding because of the realignment of crystals.

7.2 INTRODUCTION

Polymer bonded explosives (PBX) are the class of granular composites with high explosive solid crystals dispersed in a lean binder matrix. Main reasons for such formulation are to reduce impact sensitivity and improve castability. However, these materials undergo unexpected detonations under mild impact loading conditions pauses safety concerns during handling and transport. For instance, the macroscale intermediate impact velocity experiments on PBX9501 (95% explosive crystals and 5% soft binder) showed a low threshold ignition initiation velocity of 54.4-57m/s [1], whereas a high threshold ignition is critical for safety. The impact-induced explosion of this material is a complex process that involves multiple length scale features ranging from the atomic scale to macroscale. It is widely accepted that the formation of highly localized temperature regions called ‘hot spots’ is responsible for such expositions [2]. However, the fundamental

understanding of the process that controls the hotspot formation in the material is still not clear.

In the last two decades, a significant amount of research has been devoted to understand the deformation mechanisms that lead to hotspot formation. The mild impacts in the material generate compaction wave with elastic-plastic or weak shock nature depends on the magnitude of the impact with respect to the strength of the composite [3]. Numerical modeling of these impact scenarios shows that the fracture of crystals due to stress concentration resulting from force chains, localized plastic deformation of the soft binder, grain/binder debonding and propagation of the preexisting cracks are the dominant deformation mechanisms [4–12]. Consequently, significant heating at the grain scale (meso) due to viscoelastic deformation of the binder, frictional heating because of the crystal-crystal interaction, binder to crystal interaction and the relative sliding of the crack faces. However, it was argued that the fracture of the crystals may not produce hot spots due to the low surface energy of the crystals [13].

Weak shock wave structure in the granular material is observed in a piston driven problem. The compaction wave formed was observed to be propagating as a shock with the significant width [14]. The thickness of a weak shock wave is observed to have 10-50 particle diameters. The shock is dissipated as it propagates which probably can relate to the hotspot formation in the energetic materials. But no experimental support for such observations. There is convincing evidence that the wave structure at the macroscale is dominantly controlled by the events that occur at grain scale. Therefore, understanding the deformation behavior at multiple length scales is of foremost importance to explain the

macroscale phenomenon. However, there is no grain scale (mesoscale) experimental studies that have been conducted to understand the small-scale compaction structure.

Recently, in situ experiments revealed, the crystal fracture is one of the main deformation mechanism [15–17] and it is due to the tensile stress induced because of crystal to crystal force transmission [18]. However, these experiments are limited to low impact velocity (in the order of 4-10m/s), therefore, no compaction wave formation which a most common feature of an intermediate velocity is (40-200 ms^{-1}) impacts.

There are no full-field meso scale experiments to understand the mesoscale deformation mechanisms that lead to the observations at the macroscale. In this study, we have performed the intermediate velocity impact (56ms^{-1}) experiments with the newly developed experimental setup in our lab incorporating digital image correlation technique (DIC). This can capture the deformation field at high spatial and temporal resolution. The main purpose of this study is to understand the mesoscale deformation mechanisms that lead to the compaction wave characteristics observed at the macroscale.

7.3 MATERIALS AND METHODS

7.3.1 Material Preparation and Specimen geometry

Polymer bonded sugar (PBS), a mechanical simulant of high melting explosive (HMX) based polymer-bonded explosive (PBX) is used in this study. The polymer-bonded sugar (PBS) samples are prepared by cold pressing of the plasticized hydroxyl-terminated polybutadiene and sugar crystal mixture at 30MPa. Composition and the constituents in the material prepared for this study is shown in Table 1. Material preparation steps are briefly described below. HTPB is mixed with the plasticizer (DOS) and curing agent (TDI), followed by adding sugar crystals to the mixture. The mixture is mechanically mixed for

15-20minutes in order to thoroughly coat the surface of the sugar crystals with the soft binder. Then, the mixture was kept in a vacuum oven for 6-7 hours at 80^0C for partial curing. Then the partially cured mixture was pressed at 30MPa pressure in a cylindrical mold of bore diameter 25mm to cylindrical billets. These billets are completely cured at 80^0C for 120 hours and cooled slowly to a room temperature. The pressing density of the PBS materials was 1.34g/cm^3. Samples for the experiments are machined from the cylindrical billets using a milling machine. The extracted samples are mechanically polished with abrasive grinding paper up to a grit of 1200 to have a flat, smooth surface to facilitate imaging for DIC. Final dimensions of the samples were 19.13mm×17.2mm×16.83mm, 19.80mm×18.70mm×17.20mm for macroscale and mesoscale respectively.

Table 7.1 Material constituents and composition

Material constituents	**Composition (% of weight)**
Solid Constituent- Sugar Crystal	87.5
Monomer- Hydroxyl terminated polybutadiene	9.00
Plasticizer- Di-octyl Sebacate (DOS)	2.40
Curing agent- Toluene diisocyanate (TDI)	1.10

To facilitate DIC measurement, a high contrast, random and isotropic speckle pattern has to be applied on the surface of the specimen [19]. It is important to choose the right size speckles according to the image resolution of the optical system used in the experimental setup. As a thumb of rule for a good displacement resolution and accuracy, every speckle has to be sampled by at least 3-5 pixels[20]. The image resolution for the

macroscale experiment is 75µm /pixel and, therefore, speckle sizes of 240-400µm were required. These speckles were obtained using an airbrush and flat paint. First, a thin layer of white paint was applied on the surface of the specimen, and after it gets dried completely a black paint was sprayed on the top of the white layer using an airbrush. The average speckle size obtained for macroscale experiment was 300µm. In the case of the meso-scale experiment, the image resolution is 10.66 µm /pixel and hence speckle sizes of 30-50 µm were required. To speckle the specimen, first a thin layer of white paint was applied on the surface of the specimen and before the paint gets dried completely a black toner powder was deposited on the top of the thin white coat using compressed air. The specimen dimensions and the speckle pattern for the macroscale and mesoscale DIC measurement are shown in Figure 7.1, a bell-shaped intensity curve was obtained which is ideal for DIC strain measurements. For comparing the microstructure with the mesoscale local strain field the procedure described in [16] was followed.

A complete schematic of the experimental setup is shown in Figure 7.2. In this study, a direct impact configuration of the Hopkinson bar setup was used for loading the sample. It consists of a gas-gun attached to the launching tube of length 3040mm. The bore diameter of the launching tube was 25.4mm. Compressed helium was used in gas-gun to propel the projectile. The vent holes at the front side of the launch tube help in releasing the gas once the projectile is launched. An impact resistant polycarbonate bar of 25.35mm in diameter and 88mm long was used as a projectile. The length of the projectile was selected in such a way that no reloading of the sample occurs because of the reflected wave from the other end of the projectile. The specimen was attached to the transmitter bar with the help of a grease.

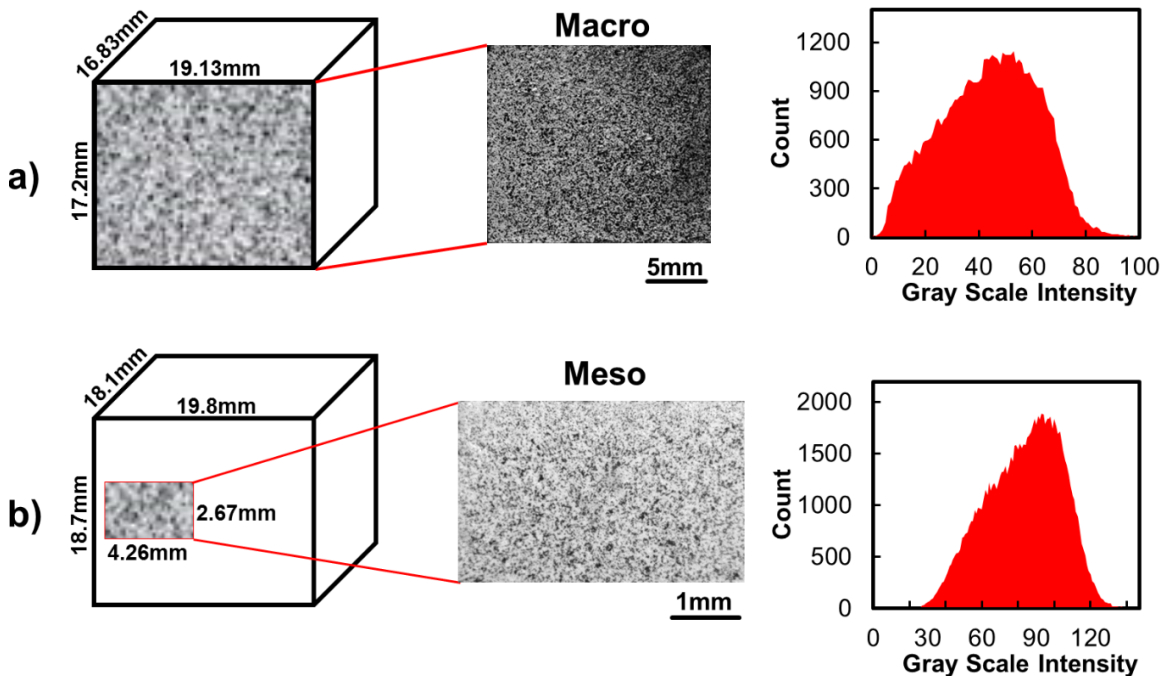

Figure 7.1. The specimen dimensions, airbrush speckle, and gray scale intensity plot, (a) Macroscale, the average size of the speckle is 300 µm, (b) Mesoscale experiments, the average size of the speckle is 25-35 µm. Both the speckles follow a bell-shaped curve.

Impact face of the projectile was precisely aligned with the transmitter to ensure the plane impact on the specimen. It should be noted that we are interested in the deformation features of the material before the compaction wave reaches the distal end from the impact end. Therefore, the transmitter bar was fixed at one end as shown in the schematic, it serves the purpose of a fixture, no measurements were taken from the transmitter bar.

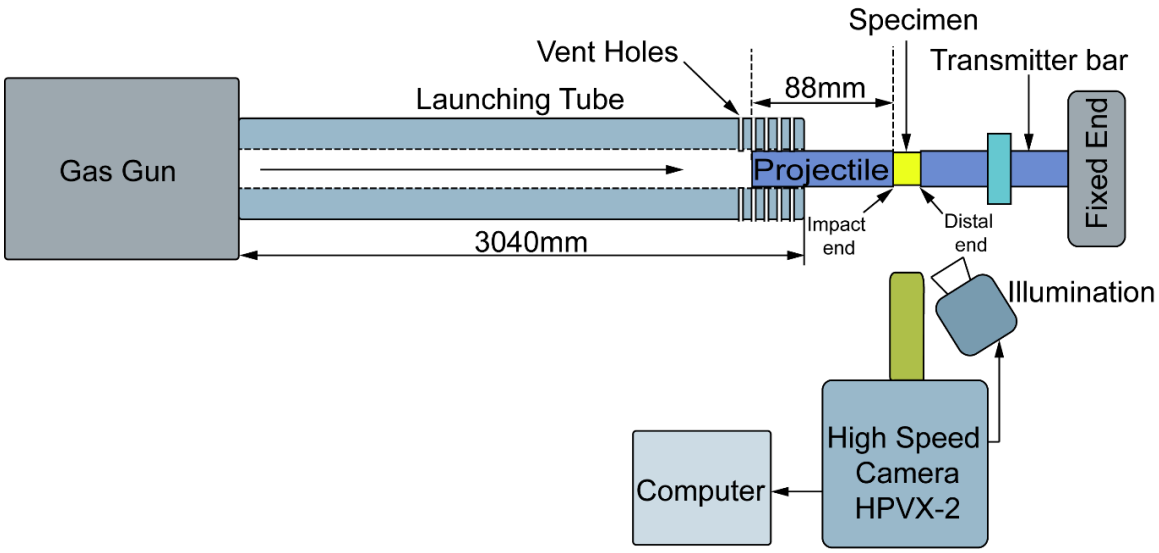

Figure 7.2 Complete schematic of the experimental setup (not to scale).

To observe the full-field deformation *in-situ*, a high-speed camera HPV-X2 from Hadland imaging was used. This high-speed camera was capable of capturing images at 5million frames/second at a resolution of 400x250 pixel^2. For the macroscale experiment, a 200mm Tikona lens was used as the objective. The illumination was provided with the metal arc lamp (Lumen 200). For the mesoscale full-field deformation measurement, a high magnification imaging lens from Navitar was employed. In this case, the illumination was provided using a flash lamp (Photogenic) due to the requirement of high intensity lighting in the high-magnification experiments. Flash lamp requires 200µs to reach its highest intensity, and it stays at a constant intensity for 1ms. Therefore, the triggering of the camera and the flashlights were performed carefully to utilize the maximum illumination during the deformation of the sample. An optical resolution of 10.66 µm/pixel was achieved using the proposed method, which is enough to obtain strain fields inside a grain of size about 400 µm. The complete details of the optical parameters used in the two systems can be found in Table.2.

Table 7.2 Imaging Parameters

Macroscale Experiment	**Mesoscale Experiment**
Imaging lens -100mm Tikona	Imaging lens Navitar Extension tube
Lighting- Lumen 200PRO, Metal arc Lamp	Lighting- Photogenic flash lamp
Imaging Framing Rate- 2 Million	Imaging Framing Rate- 2 Million
Resolution- 400×250 $pixel^2$	Resolution- 400×250 $pixel^2$
Field of view-30×18.75 mm^2	Field of view- 4.26×2.65 mm^2
Magnification factor-75 µm/pixel	Magnification factor -10.66 µm/pixel

7.4 POST PROCESSING

For macroscale and mesoscale strain field calculation, the images are processed using Vic2D, a commercial digital image correlation software by correlated solutions Inc. As mentioned above the resolution of the macroscale experiment was 75 µm/pixel and the average speckle size is 500 µm. Hence, subset sizes of 1.1×1.1 mm^2 are used considering a minimum of 3×3 speckles in one subset. The strain calculation in this study was performed with the exhaustive search mode, which enables the highest amount of data recovery when the correlation fails in the expense of processing time. A higher order interpolation function (Optimized 8-tap) was used to convert discrete digital data points to continuous data. Correlation criterion was chosen to be zero normalized, which is insensitive to the scaling of light intensity. Similarly, in the case of mesoscale strain field calculation, post-processing was done with the exhaustive search mode similar to the macroscale. However, a subset size of 96×96 μm^2 is employed in this case which enables to have at least ~14 subsets in one grain of 400µm size. Measurement performance, data smoothing and uncertainty propagation.

7.5 RESULTS AND DISCUSSION

The full-field axial strain at different times (t=0, 4, 6, 8, 10, 12, 14, and 16μs) after the impact is shown in Figure 7.3a. It illustrates, the propagation of a smooth compaction wave front across the specimen. The impact velocity was measured to be 56m/s (see Figure 7.3a). The compaction wave front separates two states in the material. Ahead of the compaction front, the axial strain is 0%, whereas behind it the axial strain is close to 6%. The transition from the compressed to the undisturbed region through the wide band and its width is called compaction wave thickness (δ).

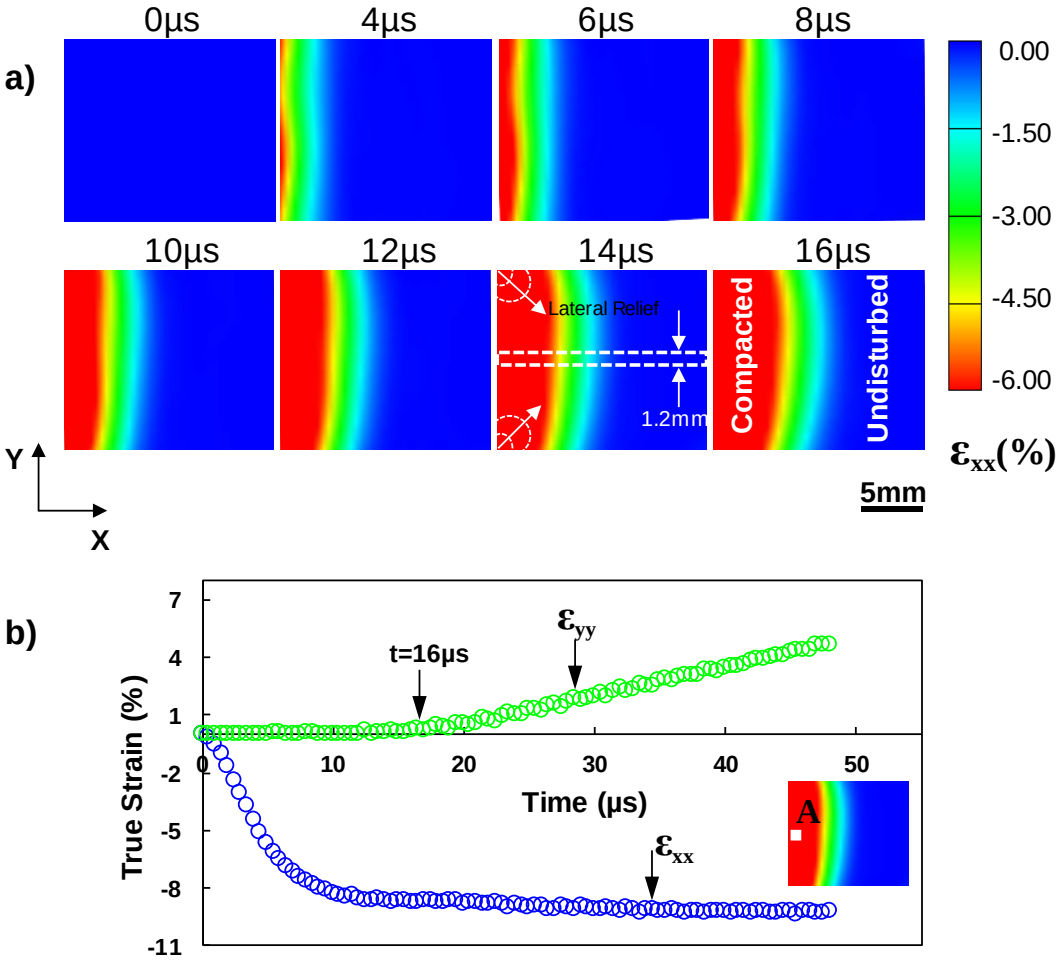

Figure 7.3 (a) Axial strain field from the macroscale experiment at t=0, 4, 6, 8, 10, 12, 14, and 16 μs. (b) evolution of axial and lateral strain at point A shows the arrival of lateral relief wave at the center of the sample at t=16 μs

We note the thickness of the compaction wave front is significant during its propagation in the material. Furthermore, the compaction wavefront is planar in the beginning ($0<t\leq10\mu s$) and gradually transforming to the non-planar wave front. This is due to the arrival of the lateral relief wave from the lateral free surface (schematically shown in Figure 7.3a at $t=14\mu s$). We found that the time required for the lateral wave to reach the centerline of thickness 1.2mm is 16μs by calculating the transverse strain induced in a small strip at the center. Therefore, a region that is of thickness 1.2mm at the center is considered, to approximately meet the uniaxial strain condition for the shock analysis of the experimental results. In this study, we transversely (y-direction) averaged the data in the small strip taking the advantage of the planar front at the center.

The instantaneous velocity of the projectile as a function of time shown in Figure 7.4a is calculated by tracking a prescribed point on the projectile. A constant projectile velocity of 56 m/s was observed prior to the impact ($t<0$ μs). After the impact, during the time $0\ \mu s \leq t \leq 8\ \mu s$, the projectile velocity dropped to 46 m/s and remains nearly constant (46±0.5 m/s) for about 5-7 μs (up to t=16 μs). It is presumable that a quasi-static equilibrium is achieved in 8 μs after the impact. After t=16μs, the projectile gained about 4m/s in 7μs and remained constant at 50m/s for the rest of the time. This increase in velocity from 46 m/s to 50 m/s could be due to the failure initiation in the material or a lateral relief wave arrival at the center of the specimen, which both offer less resistance to the projectile in a deforming the material.

The finite width of the compaction wavefront necessitates the identification of the compaction wavefront to calculate the velocity of the compaction wave. To locate the compaction front, the acceleration profile was calculated, and the axial location

corresponds to the acceleration peak is defined as the compaction wavefront (x_c) (see Figure 7.4b). Compaction wavefront location (x_c) with time is shown in Figure.7.4b. The slope of the linear fit gives a compaction wave propagation velocity (U_s) of 505m/s which is close to 1.11 times the sound velocity (C) in the material. Therefore, the compaction wave is a shock and, in this paper, the term 'compaction wave' and 'shock wave' represent the same quantity.

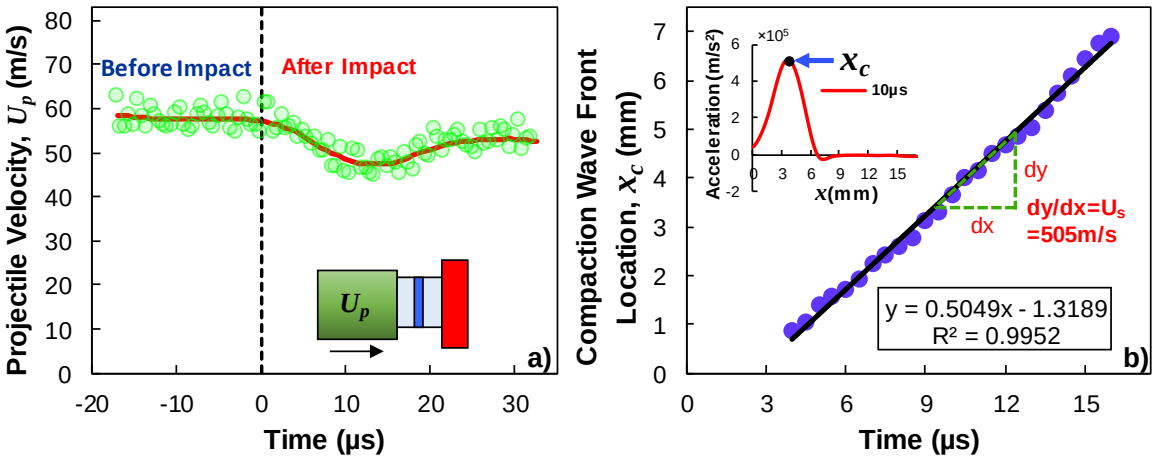

Figure 7.4 (a) Projectile velocity with time, (b) Compaction front location (x_c) with time is shown, the slope of the linear fit gives the compaction front velocity of 505m/s. Axial acceleration plot along different axial locations (x) is shown in the top left corner of Figure.7.4b. 'x' corresponds to the peak acceleration is the compaction front location (x_c).

To characterize the compaction wave profile, the particle velocity u_p along the axial direction (in the x-direction) as a function of x at different times is plotted in Figure 7.5a. The material behind the compaction band moves at a constant velocity of 41m/s, whereas ahead of it, the material is at rest. In addition, the wave profile shows a relatively gradual transition from the high-velocity region to low-velocity region which is a typical characteristic of a weak shock front. We use two important parameters, compaction wave thickness, and asymmetry of the wave profile [21–23], to fully characterize the shock front. These two parameters are defined as follows,

$$\text{Asymmetry parameter, } Q = \frac{Q_2}{Q_1} = \frac{\int_{x^*}^{\infty} u(x)dx}{\int_{-\infty}^{x^*} (u_i - u(x))dx} \qquad (7.1)$$

$$\text{Compaction wave thickness, } \delta = \frac{u_{-\infty} - u_{+\infty}}{\max\left(\left|\frac{du(x)}{dx}\right|\right)} \qquad (7.2)$$

Where $u_{-\infty}$ and $u_{+\infty}$ are the particle velocity behind and ahead of the compaction front, u(x) is the particle velocity as a function of x at any time t, u_i is the particle velocity in material close to the impact face, and x* is such that $u(x)=u_i/2$. The physical meaning of the two parameters is shown in Figure 7.5b. The typical characteristics of a weak shock front are a significant compaction front thickness (the length scale important in shock wave studies), and high symmetry in the wave profile [21]. For a perfect symmetric profile, $Q_1=Q_2$, and the asymmetry parameter Q will be equal to 1. Whereas, the strong shock will always have an asymmetric profile due to the steepening of the front arises from the nonlinear effects. Therefore, the Q value is far smaller than 1 in the case of strong shock. In addition, the steepening of the front decreases the compaction wave thickness which leads to high-velocity gradient across the front compared to weak shock waves.

We found that the Q values of the wave profile in this study are 0.91,0.90 and 0.85 at t=12,14,16μs, which is close to 1, indicating a weak shock propagation in the material. It is well-known that a stable shock front profile is the result of competition between the steepening of the wave front due to nonlinear response of the material, and front widening due to dissipation and dispersive effects. In our study, the low-velocity impact imparts low strain energy in the material. In this case, the energy dissipation dominates the steepening of the wave front which leads to the formation of a weak shock. In order to see the strength

of the compaction wave as it transverse across the material, the stress-time plot is obtained from the inertia stress calculation, see Figure 7.6a. It is seen that peak stress is dropping from 26 MPa to 19 MPa when the wave travel from x=1.6 mm to x=6 mm.

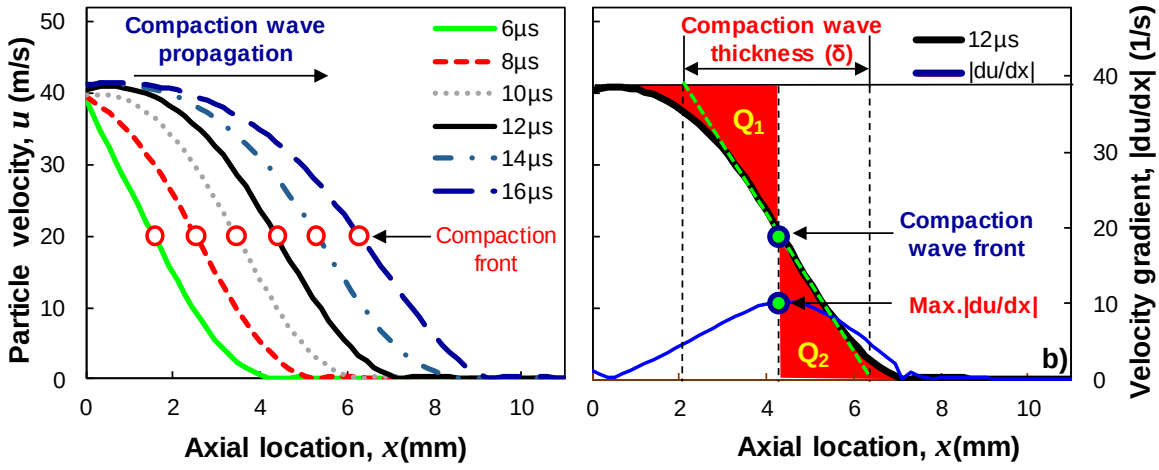

Figure 7.5 (a) The particle velocity profile of the shock at different times obtained by averaging velocity in the y-direction in the small strip at the center of thickness 1.2mm. (b) compaction wave thickness, symmetry and location of the compaction front.

We estimate the energy dissipated during shock propagation by calculating the dissipation power from the stress (σ_{ij}) and strain rate data obtained from the experiments.

$$\dot{W}_p = \sigma_{ij} : \dot{\varepsilon}_{ij} \qquad (7.3)$$

The energy dissipated per unit volume was computed by integrating Eq.7.3 with time. The time evolution of the energy associated with the compaction wave is shown in Figure 7.6c. It is shown that the energy dissipated at the impact face is significantly high. Also, the strength of the wave is decreasing as it propagates indicating the energy dissipation of weakens the compaction wave strength as it propagates along the sample. Therefore, the primary reason for the widening of the band is the dissipation dominated propagation of the compaction wave in the material.

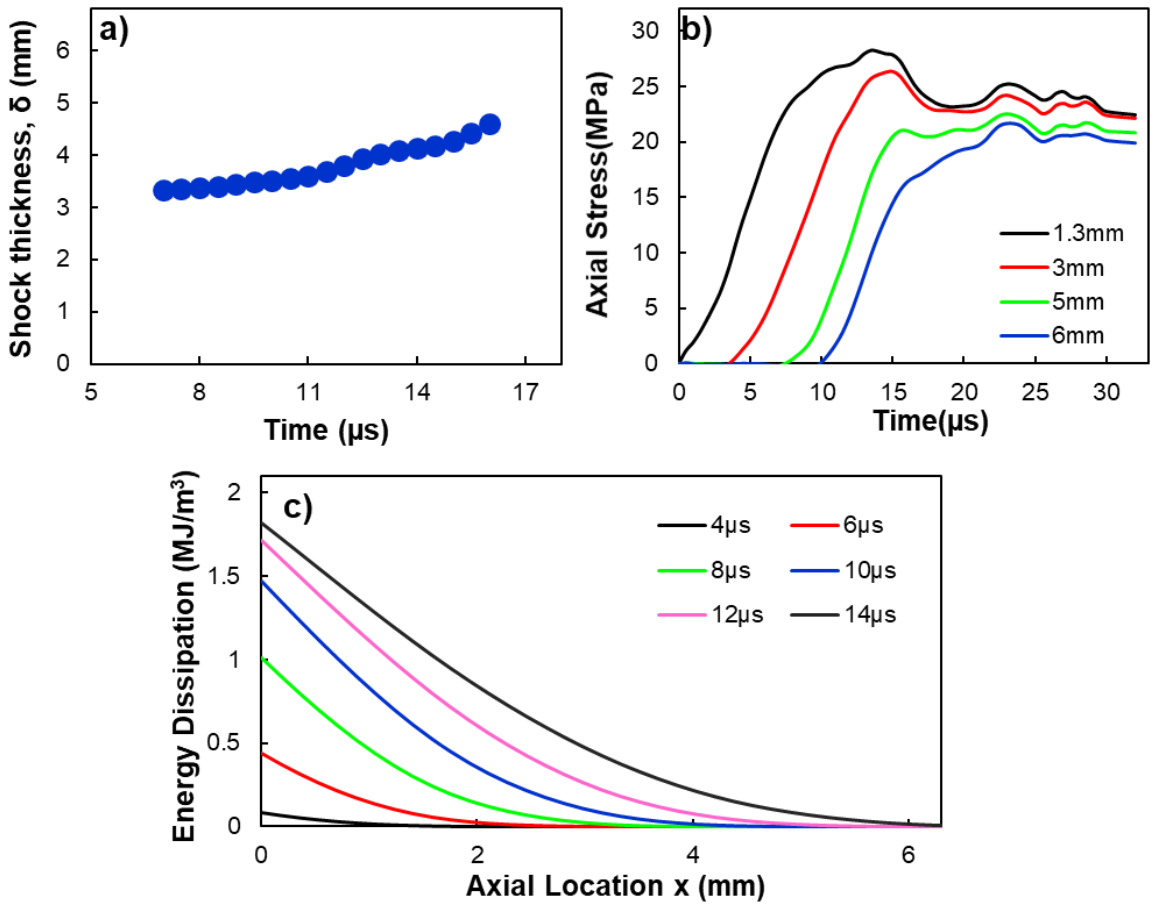

Figure 7.6. (a) Shock thickness evolution with time, (b) axial stress evolution at the different spatial location, (c) spatial energy dissipation profile at different times.

7.6 MESOSCALE STRUCTURE OF THE WEAK SHOCK WAVE

Mesoscale axial strain field shows the propagation of a heterogeneous compaction front across the material (see. Figure 7.7). The compaction front location is identified by the procedure and the compaction velocity was estimated to be 512m/s. Several features of the meso-scale axial strain field are noteworthy,1) a large strain localization, and a rough wave front in contrast to the macroscale observation, 2) strain localization spreads ahead of the compaction front. For example, at t=6μs, the compaction wave front is at x=2.3mm. However, the strain localization is observed to be extended up to x=3.1mm (2-3 crystals).

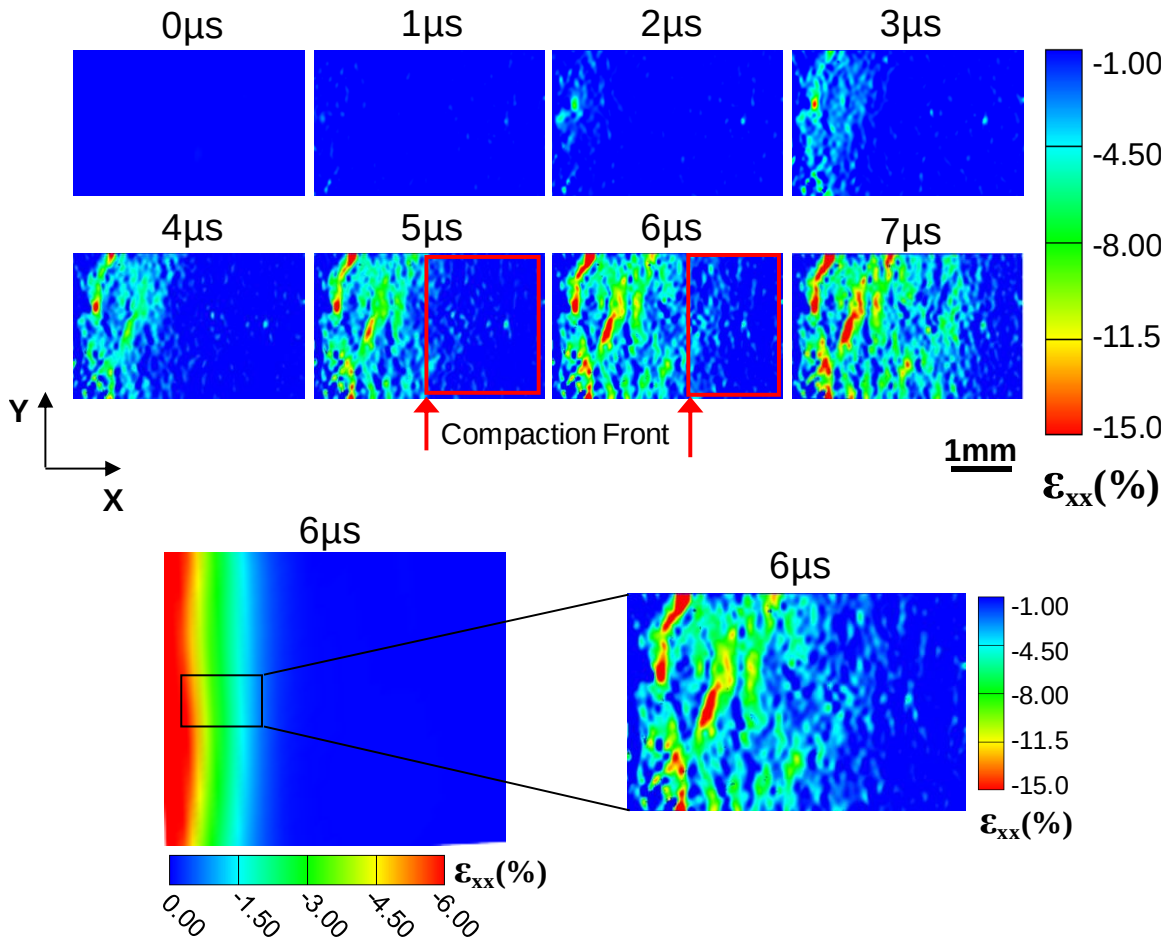

Figure 7.7. Axial strain field from the meso-scale experiment at t=0, 1, 2, 3, 4, 5, 6, and 7μs. It shows significant strain localization and propagation of a rough compaction front in the material.

This may be due to the well-known, force chain formation in granular materials. We have studied the possibility of force chain formation in the material by comparing the probability distribution of the localized axial strain with the probability distribution characteristics of the forces in granular materials. It is seen that the probability distribution of forces in granular materials with force chains has been an exponential tail [24–26]. The probability distribution function has a general form, $P(f^*) \propto \exp^{-\beta f^*}$, f^* is the force f normalized with the mean force $\langle f \rangle$ and β is the exponent.

In our study, we have obtained the local strain field at grain scale under dynamic compression. To see if the strain localization in these materials the characteristics of force chains has, we have calculated the probability distribution of the axial strain normalized with its spatial average at t=6, 7μs. An excellent fit is obtained for the probability of the axial strain normalized with its spatial average using the general probability density function (Eq.7.3) that is used in force chain characterization (see Figure 7.8). The constants have been obtained with the help of nonlinear least squares. The values obtained for the exponent 'β' is 0.91 and 0.94. Strikingly, we observed, the β values are close to the exponents of the probability distribution function in force chains in granular materials. In addition, the β exponent is close to the exponent observed for the exponential probability distribution function of stresses in granular soft matrix composites [27]. The semi-log plot shows the exponential tail of the probability distribution function which is qualitatively similar to the probability distribution of the forces in force chains (see inset Figure 7.8). These observations are consistent with the results obtained in granular ceramics which follows the similar procedure in identifying the force chain characteristics.

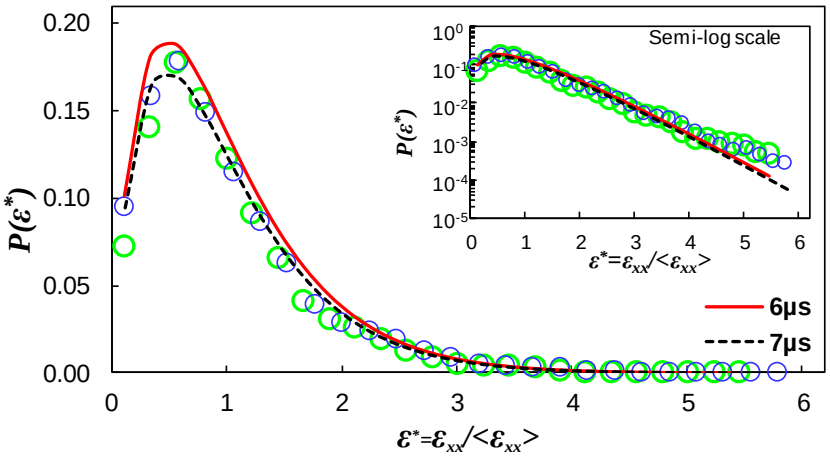

Figure 7.8 The probability distribution of the axial strain with the normalized axial strain. The probability distribution in semi-log scale is shown (to right) shows the exponential tail similar to the force chain in granular material.

$$P(f) = \alpha f^{\beta} e^{-(1+\beta) f} \qquad (7.3)$$

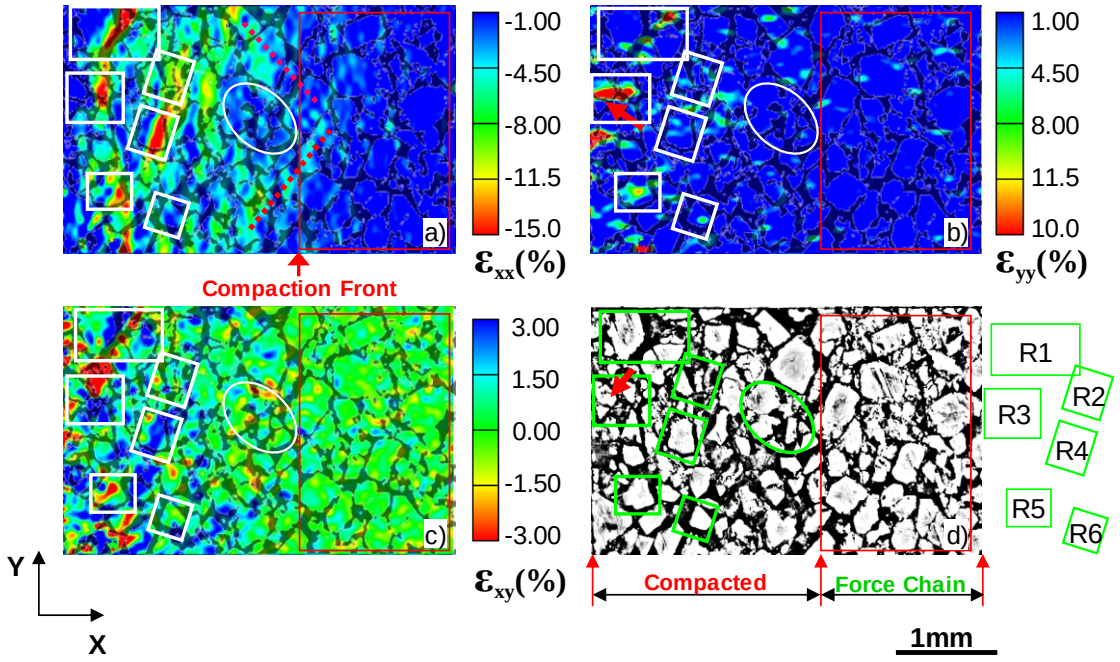

Figure 7.9 The microstructure is overlaid on the local strain field in undeformed coordinates at t=6μs, (a) axial strain field (b), transverse strain field and (c) shear strain field. (d) The microstructure of the AOI is shown and marked with rectangles. The rectangles are numbered to compare the local strain field with the microstructure.

In order to compare the strain localization and the underlying microstructure, the axial, transverse and shear strain field in undeformed coordinates are overlaid on the microstructure as shown in Figure 7.9. Accordingly, the location of the grains and strain localization are identified**.** For better visualization of the deformation mechanisms, six rectangles (R) markings are used and named as shown in Figure 7.9. For instance, consider R1, two crystals are separated by a thick polymer binder where we have high axial strain close to 15% because of compression of the polymer binder between two crystals. The load from the left crystal is transferred to the right and there it transferred to several small crystals through multipoint contacts (R2). The force diffuses to small crystals. The transverse strain in the area is significantly low whereas shear strain is close 3% indicating the possibility of shearing between the crystals. Therefore, the location is prone to

debonding of the crystals from the polymer. This is due to the tendency of crystals to realign to accommodate the high axial strain in the soft binder. The realignment of the crystal is occurring by the movement of the crystal in transverse and axial direction. In the case of thin interfaces where the crystal-crystal contact transfers the load, the chances of crystal fracture are apparent. For example, in R4, a small crystal undergoes large deformation in the order of 15% indicating the fracture of the crystal. It should be noted that the crystal is not surrounded by a thick polymer binder as in R1. The shear strain in the crystal is as high as 3% which shows the relative tangential movement of the formed crack surfaces which causes the energy dissipation in the form of heat. Surprisingly, it is observed that some areas are not undergoing any plastic deformation even locations close to the impact face. For instance, R6, where the crystal is surrounded by polymer binder, the axial strain in that region is as low as 2% which gives the support for the force chain characteristics of the deformation field. The region surrounded by two strong links of force chain is marked using an oval shape. The local strain in the region is considerably low comparing to the strain around the region. The crystals that are fractured during the processing, see R3, the crystal contains crack from the material processing which starts to propagate upon loading showing high transverse strain. However, the crack propagation is short lived and stopped at the polymer interface not extending it to the surrounding crystals.

7.7 **DISCUSSION AND CONCLUSION**

We have conducted an experimental investigation to understand the compaction wave structure at both macro and mesoscale using high speed photography incorporating DIC. It is observed that the compaction wave propagates at 505m/s which is slightly higher compared to the compaction wave velocity reported for porous samples without binder.

This is due to low porosity because of the presence binder between the crystals which gives more paths for the force transfer between the crystals. The compaction wave is of weak shock nature with symmetric wave profile. No steepening of the wave was observed instead, a dissipation dominated compaction wave propagation occurs. This leads to the widening of the compaction front with time.

The meso-scale experiment reveals that the grain scale strain field possesses force chain structure, similar to granular materials. The force transfer between the crystals is mediated through the soft binder. A smooth compaction wave front is observed at the macroscale. However, the mesoscale compaction wave is highly heterogeneous with the rough front. The roughness of the front is mainly due to the force chain formation in the material. The force chain formation leads to the formation of wide wave front structure in the material and widening of it is due to the dissipation of the energy.

The fracture stress of sugar crystal close to 210MPa [28]. Strikingly, we observed crystal fracture even for the very small average stress of 26 MPa behind the compaction front lending support to the force chain formation in the material. Consequently, the force chains are responsible for the force transfer in the material that leads, some crystals to take high loads which lead to stress concentration and fracture of the crystals. This is one of the important dissipation mechanisms. In addition, frictional heat dissipation due to the relative motion of the fracture surface and crystals contributes to the dissipated energy. Another, energy dissipation mechanism is the viscoelastic deformation of the polymer binder, as plastic deformation is inherently dissipative.

7.8 LIST OF REFERENCES

[1] Idar DJ, Straight JW, Osborn MA, Skidmore CB, Phillips DS, Buntain GA. PBX 9501 high explosive violent reaction: phase II baseline and aged experiments. See Http//Www Fas Org/Sgp/Othergov/Doe/Lanl/Lib-Www/La-Pubs/00538217 Pdf 2000.

[2] Bowden FP, Yoffe AD. Initiation and growth of explosion in liquids and solids. CUP Archive; 1952.

[3] Dick JJ, Martinez AR, Hixson RS. Plane impact response of PBX 9501 and its components below 2 GPa. Los Alamos National Lab., NM (United States); 1998.

[4] Wang X, Wu Y, Huang F, Jiao T, Clifton RJ. Mesoscale thermal-mechanical analysis of impacted granular and polymer-bonded explosives. Mech Mater 2016;99:68–78.

[5] LaBarbera DA, Zikry MA. Heterogeneous thermo-mechanical behavior and hot spot formation in RDX–estane energetic aggregates. Int J Solids Struct 2015;62:91–103.

[6] Barua A, Kim SP, Horie Y, Zhou M. Computational Analysis of Ignition in Heterogeneous Energetic Materials. Mater. Sci. Forum, vol. 767, Trans Tech Publ; 2014, p. 13–21.

[7] LaBarbera DA, Zikry MA. The effects of microstructural defects on hot spot formation in cyclotrimethylenetrinitramine-polychlorotrifluoroethylene energetic aggregates. J Appl Phys 2013;113:243502.

[8] Barua A, Horie Y, Zhou M. Energy localization in HMX-Estane polymer-bonded explosives during impact loading. J Appl Phys 2012;111:54902.

[9] Barua A, Zhou M. A Lagrangian framework for analyzing microstructural level

response of polymer-bonded explosives. Model Simul Mater Sci Eng 2011;19:55001.

[10] Bardenhagen SG, Brackbill JU, Sulsky D. Numerical study of stress distribution in sheared granular material in two dimensions. Phys Rev E 2000;62:3882.

[11] Field JE, Bourne NK, Palmer SJP, Walley SM, Sharma J, Beard BC. Hot-Spot Ignition Mechanisms for Explosives and Propellants [and Discussion]. Philos Trans R Soc London A Math Phys Eng Sci 1992;339.

[12] Coffey C, Sharma J. Plastic deformation, energy dissipation, and initiation of crystalline explosives. Phys Rev B 1999;60:9365–71. doi:10.1103/PhysRevB.60.9365.

[13] Siviour C., Laity P., Proud W., Field J., Porter D, Church P., et al. High strain rate properties of a polymer-bonded sugar: their dependence on applied and internal constraints. Proc R Soc A Math Phys Eng Sci 2008;464:1229–55. doi:10.1098/rspa.2007.0214.

[14] Gómez LR, Turner AM, Vitelli V. Uniform shock waves in disordered granular matter. Phys Rev E 2012;86:41302.

[15] Ravindran S, Tessema A, Kidane A. Effect of Crystal Density on Dynamic Deformation Behavior of PBX. Challenges Mech. Time Depend. Mater. Vol. 2, Springer; 2017, p. 87–92.

[16] Ravindran S, Tessema A, Kidane A, Sutton MA. Meso-scale Deformation Mechanisms of Polymer Bonded Energetic Materials Under Dynamic Loading. Mech. Compos. Multi-functional Mater. Vol. 7, Springer; 2016, p. 451–6.

[17] Ravindran S, Tessema A, Kidane A. Note: Dynamic meso-scale full field surface

deformation measurement of heterogeneous materials. Rev Sci Instrum 2016;87:36108.

[18] Parab ND, Roberts ZA, Harr MH, Mares JO, Casey AD, Gunduz IE, et al. High speed X-ray phase contrast imaging of energetic composites under dynamic compression. Appl Phys Lett 2016;109:131903.

[19] Chu TC, Ranson WF, Sutton MA. Applications of digital-image-correlation techniques to experimental mechanics. Exp Mech 1985;25:232–44. doi:10.1007/BF02325092.

[20] Sutton MA, Orteu JJ, Schreier H. Image Correlation for Shape, Motion and Deformation Measurements: Basic Concepts,Theory and Applications. Springer Science & Business Media; 2009.

[21] Turner AM, Vitelli V. Uniform Shock Waves in Disordered Granular Matter 2012:1–12.

[22] Torrilhon M, Struchtrup H. Regularized 13-moment equations: shock structure calculations and comparison to Burnett models. J Fluid Mech 2004;513:171–98.

[23] Schmidt B. Electron beam density measurements in shock waves in argon. J Fluid Mech 1969;39:361–73.

[24] Majmudar TS, Behringer RP. Contact force measurements and stress-induced anisotropy in granular materials. Nature 2005;435:1079–82.

[25] Mueth DM, Jaeger HM, Nagel SR. Force distribution in a granular medium. Phys Rev E 1998;57:3164.

[26] Radjai F, Jean M, Moreau J-J, Roux S. Force distributions in dense two-dimensional granular systems. Phys Rev Lett 1996;77:274.

[27] Radjai F, Topin V, Richefeu V, Voivret C, Delenne J-Y, Azéma E, et al. Force transmission in cohesive granular media. Math Model Phys Instances Granul Flows 2010:240–60.

[28] Gibbs TR. LASL explosive property data. vol. 4. Univ of California Press; 1980.

CHAPTER 8

SUMMARY AND RECOMMENDATIONS

8.1 SUMMARY

Experimental evidence and understanding of the multiscale deformation mechanisms in polymer bonded explosives were exceptionally limited. Therefore, to observe and quantify the full-field multiscale behavior of PBX, a new high spatiotemporal resolution experimental setup based on digital image correlation was developed. The experimental setup was capable of measuring deformation and failure behavior of heterogeneous materials at a spatial resolution of 10 μm/pixel at a temporal resolution of 200 ns. In this study, multiscale experiments are conducted at different strain rates to elucidate the local failure mechanisms and its connection to the macroscopic failure modes. Mainly, two loading cases are considered in this study. The first study was focused on the understanding the local deformation and failure mechanisms in PBX at a varying strain rate (150- 1000 s^{-1}). The main observations and conclusions are described below,

1. Using the developed experimental setup, multiscale failure mechanisms at an intermediate strain rate is performed in polymer bonded sugar samples. It is seen that the main deformation mechanism are crystal fracture, delamination and binder deformation. In addition, the crystal seen to be rotating during deformation.

2. It is shown that the wide shear bands are formed in the polymer-bonded explosives and the wide is due to the mechanical softening occurred in the sample during dynamic loading.
3. It is shown that the shear band formed in polymer bonded explosives are of a dilative type, therefore, the crystal fracture in the shear bands are less compared to the compaction type shear bands seen in granular materials.
4. Effect volume fraction in the dynamic deformation behavior of polymer bonded explosives shows that low mass fraction specimens show elastic-perfectly plastic behavior whereas, at a higher mass fraction, the stress-strain curve shows relatively a brittle type failure. The mesoscale experiments reveal that at a solid mass fraction of 80 %, the deformation is mainly constrained in a binder with very small deformation of the binder. Whereas, at a higher solid mass fraction (87.5 and 95 %), crystal fracture and delamination started to observe at the very early stage of loading.
5. The damage evolution was quantified using volumetric strain evolution in PBS under dynamic loading. Effect of solid mass fraction and strain on the damage evolution was also discussed in detail.

The second study was focused on understanding the weak shock propagation in PBX under impact loading conditions. We have performed experiments at an impact velocity varying from 50- 100 m/s.

1. From this study, a complete characterization of the weak shock wave propagation in PBX was performed. Particle velocity, shock velocity, and shock thickness were calculated using full-field displacement measurement.

2. It is observed that weak shock waves are propagating at a velocity close to 506 m/s for an impact velocity of 56 m/s and it is seen to be increasing linearly with increase in impact velocity.
3. Spatial stress profile of during shock propagation was calculated from the experiments using equilibrium equations for the first time.
4. Using the stress and strain rate calculated, the energy dissipated during weak shock propagation was calculated for the first time.
5. It was observed that shock thickness initially stays approximately constant which started to gradually increase after t=12 μs. The mesoscale experiments show that, the wide shock structure due to the formation of force chain within the material during the shock propagation. In addition, the energy dissipation mechanisms were identified to be crystal fracture, relative sliding of the fractured crystals, binder deformation and friction dissipation due to binder crystal sliding and crystal to crystal sliding.

8.2 RECOMMENDATIONS

In this study, we acquired a comprehensive understanding of the material behavior under weak impact regime (high rate or weak shock) simulating accidental loading scenarios. However, an explosive may undergo high intense loading during its service. Therefore, there is a great deal of understanding is required in a high-speed impact regime where a strong shock wave propagation is possible. In such a loading case, the local failure and dissipation mechanisms may be very different from the weak shock/high rate loading regime. It was qualitatively showed that the pore collapse may be a mechanism for hot spot formation in high-velocity impact regime, however, a quantitative measurement of

deformation around the pore collapse regions is not performed previously. With the developed experimental setup developed in this study, it is possible to understand the dynamics of void collapses in polymer binders.

The current study was mainly focused on the PBX with no experiments performed on granular explosives. The stress calculation technique developed in this study has huge potential for estimating the spatial energy dissipation in granular explosives where only the numerical simulation data

Another aspect of the research is the temperature measurement at high temporal and spatial resolution under real loading conditions. Such experiments are very rare due to the available technology. However, such experiments are extremely necessary to isolate the local dissipation mechanisms that lead to the formation of hotspots and the following detonation.

APPENDIX A

PUBLISHER PERMISSION

Permission to reuse the paper titled "Dynamic meso-scale full-field surface deformation measurement of heterogenous materials".

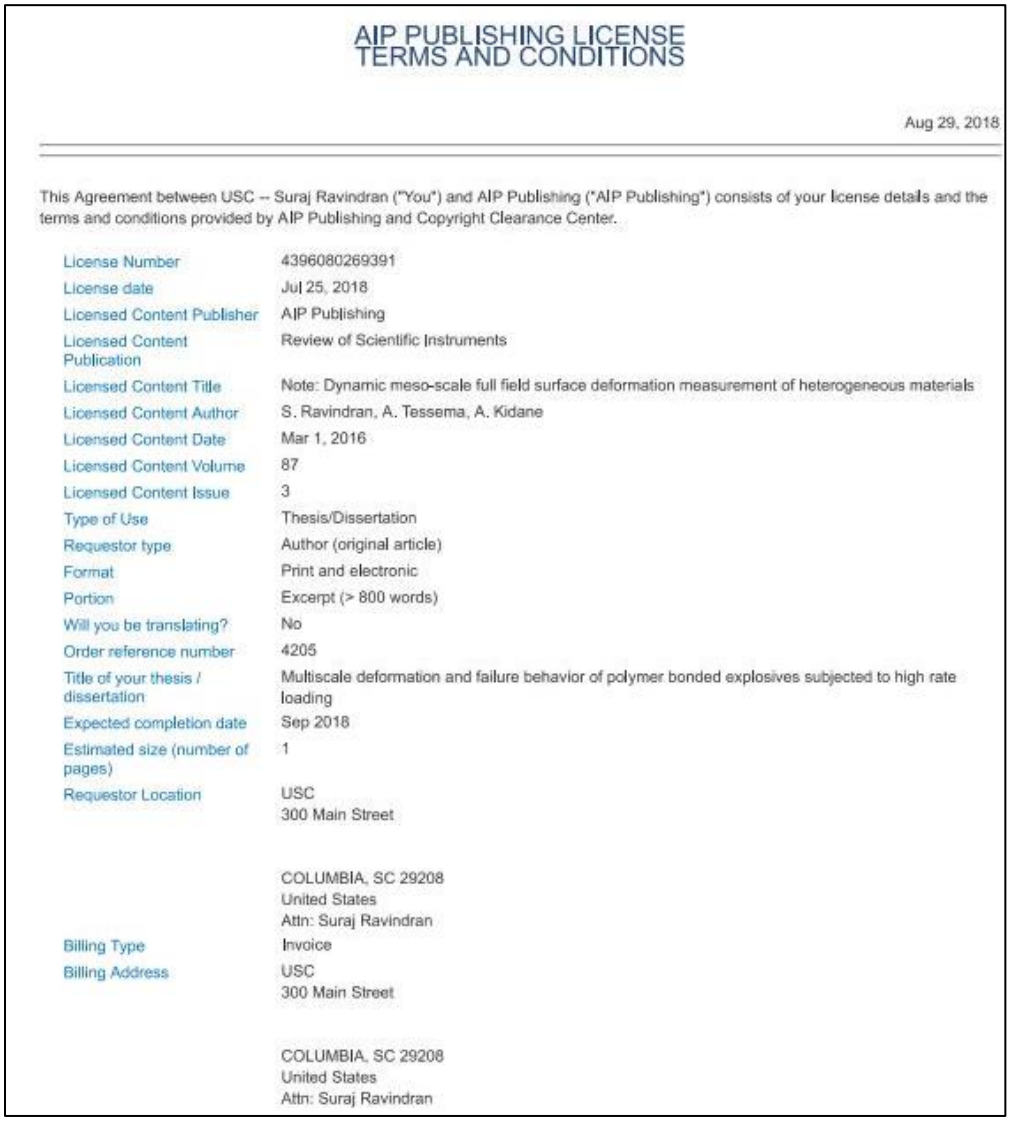

AIP PUBLISHING LICENSE
TERMS AND CONDITIONS

Aug 29, 2018

This Agreement between USC -- Suraj Ravindran ("You") and AIP Publishing ("AIP Publishing") consists of your license details and the terms and conditions provided by AIP Publishing and Copyright Clearance Center.

License Number	4396080269391
License date	Jul 25, 2018
Licensed Content Publisher	AIP Publishing
Licensed Content Publication	Review of Scientific Instruments
Licensed Content Title	Note: Dynamic meso-scale full field surface deformation measurement of heterogeneous materials
Licensed Content Author	S. Ravindran, A. Tessema, A. Kidane
Licensed Content Date	Mar 1, 2016
Licensed Content Volume	87
Licensed Content Issue	3
Type of Use	Thesis/Dissertation
Requestor type	Author (original article)
Format	Print and electronic
Portion	Excerpt (> 800 words)
Will you be translating?	No
Order reference number	4205
Title of your thesis / dissertation	Multiscale deformation and failure behavior of polymer bonded explosives subjected to high rate loading
Expected completion date	Sep 2018
Estimated size (number of pages)	1
Requestor Location	USC 300 Main Street COLUMBIA, SC 29208 United States Attn: Suraj Ravindran
Billing Type	Invoice
Billing Address	USC 300 Main Street COLUMBIA, SC 29208 United States Attn: Suraj Ravindran

Permission to reuse the paper titled “Local Deformation and Failure mechanisms of Polymer Bonded Energetic Materials Subjected to High Strain Rate Loading”.

SPRINGER NATURE LICENSE TERMS AND CONDITIONS

Aug 29, 2018

This Agreement between USC -- Suraj Ravindran ("You") and Springer Nature ("Springer Nature") consists of your license details and the terms and conditions provided by Springer Nature and Copyright Clearance Center.

License Number	4418360038264
License date	Aug 29, 2018
Licensed Content Publisher	Springer Nature
Licensed Content Publication	Journal of Dynamic Behavior of Materials
Licensed Content Title	Local Deformation and Failure Mechanisms of Polymer Bonded Energetic Materials Subjected to High Strain Rate Loading
Licensed Content Author	Suraj Ravindran, Addis Tessema, Addis Kidane
Licensed Content Date	Jan 1, 2016
Licensed Content Volume	2
Licensed Content Issue	1
Type of Use	Thesis/Dissertation
Requestor type	academic/university or research institute
Format	electronic
Portion	full article/chapter
Will you be translating?	no
Circulation/distribution	501 to 1000
Author of this Springer Nature content	yes
Title	Multiscale deformation and failure behavior of polymer bonded explosives subjected to high rate loading
Instructor name	Addis Kidane
Institution name	University of South Carolina
Expected presentation date	Sep 2018
Order reference number	4204
Requestor Location	USC 300 Main Street COLUMBIA, SC 29208 United States Attn: Suraj Ravindran
Billing Type	Invoice
Billing Address	USC 300 Main Street COLUMBIA, SC 29208 United States Attn: Suraj Ravindran

Permission to reuse the paper titled “Multiscale damage evolution in polymer bonded sugar under dynamic loading”.

Title: Multiscale damage evolution in polymer bonded sugar under dynamic loading

Author: Suraj Ravindran,Addis Tessema,Addis Kidane

Publication: Mechanics of Materials

Publisher: Elsevier

Date: November 2017

Logged in as:
Suraj Ravindran
USC